

Calculation of Tilt Rotor Aeroacoustic Model (TRAM DNW)

Performance, Airloads, and Structural Loads

Wayne Johnson

Army/NASA Rotorcraft Division

NASA Ames Research Center

Moffett Field, California

Comparisons of measured and calculated aeromechanics behavior of a tiltrotor model are presented, with an emphasis on performance and structural loads. The recent test of the Tilt Rotor Aeroacoustic Model (TRAM) with a single, 1/4-scale V-22 rotor in the German-Dutch Wind Tunnel (DNW) provides an extensive set of aeroacoustic, performance, and structural loads data. The calculations were performed using the rotorcraft comprehensive analysis CAMRAD II. The comparison of measurements and calculations includes helicopter mode operation (performance, airloads, and blade structural loads), hover performance, and airplane mode performance. The correlation establishes the level of predictive capability achievable with current technology; identifies the limitations of the current aerodynamic, wake, and structural models of tiltrotors; and leads to recommendations for research to extend tiltrotor aeromechanics analysis capability.

Nomenclature

a	speed of sound	P	rotor power, $P = \Omega Q$
c_n	blade section normal force coefficient, $N/(1/2\rho U^2 c)$	q	dynamic pressure, $1/2\rho V^2$
c_{ref}	blade reference chord	Q	rotor torque
C_P	rotor power coefficient, $P/\rho(\Omega R)^3 A = Q/\rho(\Omega R)^2 R A$	T	rotor thrust (shaft axes)
C_T	rotor thrust coefficient, $T/\rho(\Omega R)^2 A$ (shaft axes)	U	blade section resultant velocity (used for c_n), $U^2 = (\Omega r + V \cos \alpha \sin \psi)^2 + (V \sin \alpha)^2$
C_X	rotor propulsive force coefficient, $X/\rho(\Omega R)^2 A$ (wind axes, positive forward)	X	rotor propulsive force (wind axes, positive forward)
$M^2 c_n$	blade section normal force coefficient times Mach number squared, $N/(1/2\rho a^2 c)$	V	wind tunnel speed
M_{tip}	blade tip Mach number, $\Omega R/a$	α, α_s	rotor shaft angle (positive aft, zero for helicopter mode)
N	number of blades	μ	advance ratio, $V/\Omega R$
N	blade section normal force	ρ	air density
r	blade radial station (0 to R)	σ	rotor solidity, $N c_{ref}/\pi R$ ($\sigma = 0.105$ for TRAM)
R	blade radius	ψ	blade azimuth angle (zero azimuth is downstream)
		Ω	rotor rotational speed

Introduction

The tiltrotor aircraft configuration has the potential to revolutionize air transportation by providing an economical combination of vertical take-off and landing capability with efficient, high-speed cruise flight. To achieve this potential it is necessary to have validated analytical tools that will support future tiltrotor aircraft development. These

Presented at the American Helicopter Society Aeromechanics Specialists' Meeting, Atlanta, Georgia, November 13–15, 2000. This paper is declared a work of the U.S. Government and is not subject to copyright protection in the United States.

analytical tools must calculate tiltrotor aeromechanical behavior, including performance, structural loads, vibration, and aeroelastic stability, with an accuracy established by correlation with measured tiltrotor data. For many years such correlation has been performed for helicopter rotors (rotors designed for edgewise flight), but correlation activities for tiltrotors have been limited, in part by the absence of appropriate measured data. The recent test of the Tilt Rotor Aeroacoustic Model (TRAM) with a single, 1/4-scale V-22 rotor in the German-Dutch Wind Tunnel (DNW) now provides an extensive set of aeroacoustic, performance, and structural loads data.

This report documents correlation between the TRAM DNW measured performance and structural loads data and CAMRAD II calculations. CAMRAD II is a modern rotorcraft comprehensive analysis, with advanced models intended for application to tiltrotor aircraft as well as helicopters. Comprehensive analyses have undergone extensive correlation with performance and loads measurements on helicopter rotors. The present paper is an initial effort to perform an equally extensive correlation with tiltrotor data. The comparison of measurements and calculations includes helicopter mode operation (performance, airloads, and blade structural loads), hover performance, and airplane mode operation performance. The correlation establishes the level of predictive capability achievable with current technology; identifies the limitations of the current aerodynamic, wake, and structural models of tiltrotors; and leads to recommendations for research to extend tiltrotor aeromechanics analysis capability.

TRAM DNW Test

The purpose of the Tilt Rotor Aeroacoustic Model (TRAM) experimental project is to provide data necessary to validate tiltrotor performance and aeroacoustic prediction methodologies and to investigate and demonstrate advanced civil tiltrotor technologies. The TRAM activity is a key part of the NASA Short Haul Civil Tiltrotor (SHCT) project. The SHCT project is an element of the Aviation Systems Capacity Initiative within NASA.

In April-May 1998 the TRAM was tested in the isolated rotor configuration at the Large Low-speed Facility of the German-Dutch Wind Tunnels (DNW). A preparatory test was conducted in December 1997. These tests were the first comprehensive aeroacoustic tests for a tiltrotor, including not only noise, performance, and structural loads data, but airload and wake measurements as well. The TRAM can also be tested in a full-span configuration, incorporating both rotors and a fuselage model. The TRAM and the DNW test are described in references 1 to 3.

Figure 1 shows the wind tunnel installation of the TRAM isolated rotor. The DNW is a closed return, atmospheric pressure wind tunnel, with three interchangeable test sections. The TRAM test utilized the 6- by 8-meter open-jet test section, which is in a large anechoic testing hall. In this configuration the tunnel has a maximum airspeed of 85 m/sec.

The rotor tested in the DNW was a 1/4-scale (9.5 ft diameter) model of the right-hand V-22 proprotor. The rotor was tested at a tip Mach number of 0.63 in helicopter mode (because of operational limitations, this was lower than the V-22 nominal tip Mach number of 0.71); and 0.59 in airplane mode (matching the V-22). The rotor and nacelle assembly was attached to an acoustically-treated, isolated rotor test stand through a mechanical pivot (the nacelle conversion axis), as shown in figure 1. The nacelle (but not the spinner) contours model the V-22. The test stand contained the electric motor assembly, and was attached to the DNW sting mount. The conversion angle was manually adjusted, set to 90 deg nacelle angle for helicopter mode and 0 deg nacelle angle for airplane mode testing. As shown in figure 1, the sting was at a nominal angle of 15 deg, so a nacelle angle of 75 deg or -15 deg relative to the sting produced the nacelle angle of 90 deg or 0 deg relative to the horizontal. In helicopter mode or airplane mode (fixed nacelle angle), the rotor shaft angle of attack was set by changing the angle of the sting mount. The DNW sting mount automatically adjusted the vertical position to maintain the hub on the tunnel centerline as shaft angle of attack changed.

TRAM Physical Description

The Tilt Rotor Aeroacoustic Model (TRAM) is a general-purpose test bed for moderate-scale tiltrotor models. TRAM consists of two hardware-interchangeable test rigs: an isolated rotor test stand, and a full-span, dual-rotor model. The contractor team of Micro Craft and McDonnell Douglas Helicopter (now Boeing) had overall responsibility for the TRAM development, under the direction of the Aeromechanics Branch, Army/NASA Rotorcraft Division, NASA Ames Research Center.

The TRAM was designed as a 0.25-scale V-22 tiltrotor aircraft model. The rotor has a diameter of 9.5 ft. Nominal 100% rotor speed is 1588 rpm in helicopter mode (790 ft/sec tip speed, tip Mach number 0.708 at standard conditions) and 1331 rpm in airplane mode (662 ft/sec and 0.593 Mach number). The rotor blades and hub are designed as geometrically and dynamically scaled models of the V-22 blades. The hub is gimbaled with a constant velocity joint consisting of a spherical bearing and elastomeric torque links. The blade set has both strain-gauged and pressure-instrumented blades. The pressure instrumentation consists of 150 transducers (three different

types of Kulite transducers) distributed over two rotor blades.

The TRAM blade assembly consists of the rotor blade, the pitch case, and the yoke or flexbeam. All forces and moments at the root of the rotor blade are transferred through its rigid attachment to the pitch case. The outboard centering bearing (between the pitch case and the outboard end of the yoke) allows only the centrifugal force and flapwise and chordwise shears to be transferred to the yoke. Therefore, the yoke and pitch case serve as dual load paths for the shears, while the torsion, flapwise, and chordwise moments are carried exclusively by the pitch case. Near the inboard end of the yoke, the inboard centering bearing carrier transfers the pitch case shears back into the yoke through the inboard centering bearing, which does not allow the transfer of any moments to the yoke. The resultant loads in the yoke are transferred to the rotor hub through a rigid connection. Both centering bearings are designed so that no moments are transmitted. The inboard bearing is also free to move axially. Blade pitch control moments are applied to the pitch case through a conventional pitch arm, control rod, and swashplate assembly.

The rotor hub assembly transfers the loads from the yoke into the rotor shaft. The rotor hub consists of a gimbal that is free to tilt 12 degrees about the hemispherical retainers, without restoring springs (after 12 degrees of travel, the hub contacts a rubber bumper). A series of three elastomeric torque links transfer the torque from the gimbal hub to the non-tilting torque link hub. The nacelle (but not the spinner) contours model the V-22. The nacelle contains a six-component rotor balance and an instrumented (torque and residual thrust) flex-coupling to measure rotor performance (forces and torque). The test stand contains the electric motor assembly. The nacelle angle is manually adjusted between helicopter mode (90 deg) and airplane mode (0 deg).

Reference 4 provides complete details of the TRAM physical description. The sources of the data in reference 4 include the design analysis reports, various subsystem qualification and test reports, CAD data, and NASA measurements. Table 1 presents the principal characteristics of the TRAM. The solidity $\sigma = 0.105$ is the official value (thrust-weighted), used to normalize measured and calculated data in this report. The inboard centering bearing at $r/R = 0.0631$ is the location of the effective flap and lag hinge, with hinge stiffness provided by the yoke and spindle. Figure 2 shows the blade chord and twist distributions.

The TRAM blade airfoils are the V-22 airfoils designated XN28, XN18, XN12, XN09, at radial stations $r/R = 0.2544, 0.50, 0.75, 1.00$ respectively. The root

fairing has a special airfoil section. The airfoil tables used in the present investigation are those generated during the JVX program in the mid 1980's. The airfoil tables contain data for lift, drag, and moment coefficient as a function of angle-of-attack and Mach number. Reference 5 is the source of this airfoil data. The data are from pressure wind tunnel tests of 6.5 inch chord airfoils, at Reynolds number of approximately $Re/M = 15$ to 20 million (M is the Mach number). For the root fairing the V-22 cuff airfoil data were used, although the contours of the TRAM root fairing do not match the V-22 because of constraints imposed by the blade pitch case geometry and construction. Also used in the present investigation are the current V-22 airfoil tables (identified as the EMD tables). The differences between the JVX and EMD tables are primarily the lift and drag coefficients at negative angle of attack for the XN09 section, and a new table for the cuff airfoil.

The TRAM blade set consists of both strain-gauged and pressure-instrumented blades. There are 150 pressure transducers distributed over two right-hand rotor blades. Table 2 gives the radial positions of the pressure measurements. At the start of the test, 135 of the pressure gages were operational. Chordwise rows of pressure transducers are distributed between two blades in a manner that minimizes the difference in span moment caused by mass distribution effects of the instrumentation wiring and spanwise transducer location. A third blade carries all of the required safety of flight strain gauge instrumentation. The structural design of the TRAM blade is based on a prepreg glass/graphite epoxy hybrid composite. The blade consists of precured spar and skin/core assemblies joined during a bonded assembly stage. Instrumentation wiring packages for measuring pressure or strain are surface mounted into recessed cavities on the blade skin. The strain-gauged and pressure-instrumented blades have nominally identical mass distributions and center-of-gravity locations.

The balance and flex-coupling measure forces and torque. Rotor control positions and gimbal motion are measured. There are redundant measurements for most non-rotating quantities, including balance loads. Table 2 summarizes the blade instrumentation. Five radial stations are instrumented for flap and chord bending moment, and four radial stations for torsion moment. Pitch link force is measured on all three blades. Pitch link loads A, B, and C correspond to blades at 240 deg, 120 deg, and 0 deg relative to the reference azimuth. The blade pressure is measured in chordwise arrays (upper and lower surface) at eight radial stations. Leading edge pressures are measured at additional stations. These pressure measurements can be integrated chordwise to obtain blade section normal force at seven radial stations (there are too few chordwise points at 98% radius to get section normal force). Reference 3 describes

the data reduction process for the blade pressures and section normal force.

Rotorcraft Analysis

The TRAM was analyzed using the rotorcraft comprehensive analysis CAMRAD II. CAMRAD II is an aeromechanical analysis of helicopters and rotorcraft that incorporates a combination of advanced technologies, including multibody dynamics, nonlinear finite elements, and rotorcraft aerodynamics. The trim task finds the equilibrium solution (constant or periodic) for a steady state operating condition, in this case a rotor operating in a wind tunnel. For wind tunnel operation, the thrust and flapping (longitudinal and lateral gimbal tilt) are trimmed to target values. The aerodynamic model includes a wake analysis to calculate the rotor nonuniform induced-velocities, using rigid, prescribed or free wake geometry. The results presented here were all obtained using a free wake. CAMRAD II is described in references 6 to 10. CAMRAD II and similar analyses have undergone extensive correlation with performance and loads measurements on helicopter rotors (see, for example, reference 8). The present paper is an initial effort to perform an equally extensive correlation with tiltrotor data.

Structural Dynamic Model

Figure 3 illustrates the CAMRAD II model of the TRAM. The analytical model has a fixed shaft (no test stand dynamics) and constant rotor rotational speed (no drive train dynamics). The hub has a gimbal joint at the center of rotation, with nominal pitch/gimbal coupling of $\delta_3 = -15$ deg. The true kinematics of the gimbal can be analyzed (either Hook's joint or constant speed), but generally for efficiency a simulated gimbal is used, consisting of a flap hinge at the center of rotation, with harmonics of the gimbal motion at multiples of 3 per-rev suppressed in the trim solution. The pitch link flexibility represents all flexibility of the control system.

The TRAM blade root has a dual load-path, consisting of the pitch case and the yoke/spindle, between the inboard and outboard centering bearings (at $r/R = 0.06314$ and 0.18024 respectively). A CAMRAD II model of this configuration was developed, with a three degree of freedom angular joint at the outboard centering bearing, and a six degree of freedom (angular then linear) joint at the inboard centering bearing. The inboard linear joint has a large spring in the normal (blade thrust) direction, and a zero axial spring stiffness. However, the pitch case is much stiffer than the yoke and flexbeam, so this dual load-path model is unnecessarily complex. An equivalent model of the kinematics consists of flap, lag, and pitch rotations at the inboard centering bearing, plus elastic bending and torsion of the blade outboard of the pitch case. The yoke

and spindle provide spring stiffness for these flap and lag rotations. The CAMRAD II model of the TRAM for the results presented here has a single load-path root. At the inboard centering bearing ($r/R = 0.06314$) there are flap and lag hinges, followed by the blade pitch rotation. The blade is modelled as rigid inboard of these hinges, and from the hinges to $r/R = 0.18024$ (the pitch case). The equivalent spring stiffnesses about the flap and lag hinges were determined by matching the calculations to the measured nonrotating blade frequencies and deflections.

Table 3 identifies the source of the TRAM blade geometric, inertial, and structural properties for the CAMRAD II model. These properties are obtained from reference 4. The pitch axis is the axis of twist of the blade. The elastic axis is assumed to be coincident with the pitch axis. Figure 4 shows the blade planform, including the chordwise offsets of the center of gravity and tension center, and the nodes on the elastic axis. The tension center information in reference 4 coincides with the measured center of gravity offsets, except for the offsets associated with the blade instrumentation. For improved correlation with measured mean bending loads, the tension center has been set to zero for $r/R < 0.5$ (see figure 4). The blade is represented structurally by four elastic beam elements, with nodes at $r/R = 0.195, 0.375, 0.595, 0.795$, in addition to nodes at the inboard centering bearing ($r/R = 0.06314$, location of the flap, lag, and pitch rotations) and the outboard centering bearing ($r/R = 0.18024$). Blade bending and torsion moments are calculated by a force balance method. For best accuracy in these load calculations, the structural nodes have been aligned with the edges of the aerodynamic panels.

Table 4 presents the measured nonrotating frequencies and root stiffness of the cantilever TRAM blade. The flap, lag, or pitch link stiffness was obtained by measuring the rotation of the pitch case about the inboard feathering bearing, caused by flap, lag, or torsion load applied at the blade tip. Table 4 gives two stiffness values, the first obtained with the aluminum pitch cases and the second with titanium pitch cases. The DNW test was conducted using the aluminum pitch cases, which were subsequently replaced by the titanium pitch cases. The pitch case material is not expected to change the root stiffness significantly, so the results for the both pitch cases are considered here. The frequencies were measured by a rap test (with aluminum pitch cases). The flap hinge stiffness and the pitch link stiffness of the CAMRAD II model are determined by matching the measured nonrotating fundamental flap and pitch/torsion frequencies (the frequencies shown in bold in table 4). The resulting stiffnesses are close to the measured stiffnesses, although the pitch link stiffness is somewhat higher. However, the fundamental lag frequency proved difficult to measure.

Matching the measured nonrotating lag frequency results in a low root lag stiffness compared to the measured value, and an unreasonably low rotating lag frequency (just slightly above one per-rev at 1588 rpm). Therefore the lag hinge stiffness of the CAMRAD II model is determined by matching the measured nonrotating lag stiffness (the stiffness shown in bold in table 4). Figure 5 shows the blade frequencies as a function of rotor speed for cantilever and cyclic modes, at zero and 60 deg collective pitch. For cantilever modes, the blade root boundary condition is cantilevered in both flap and lag directions. For cyclic modes, the flap boundary condition is pinned at the center of rotation. In addition, the CAMRAD II model has the damping at the pitch bearing set to 1.5 ft-lb/rad/sec, based on correlation with the oscillatory pitch link loads. This damping coefficient corresponds to 7% critical damping of the pitch/torsion mode at about 8.75 per-rev.

The CAMRAD II solution for the periodic rotor motion in trim used 10 harmonics of 12 cantilever elastic blade modes plus the gimbal degree of freedom. The blade structural damping was assumed to be 3% for each mode. Performance and airloads calculations were also performed neglecting the elastic blade motion (but retaining the gimbal motion, and usually the motion at the flap and lag hinges).

Aerodynamic Model

The aerodynamic model uses lifting-line theory with a vortex wake calculation of the induced velocity. The blade aerodynamic surfaces are represented by 16 panels, from the root cutout of $r/R = 0.10558$ to the tip, with panel widths varying from 0.09R inboard to 0.025R at the tip. Midpoints of seven of the aerodynamic panels are aligned with the pressure instrumentation on the TRAM blades, to avoid additional interpolation in the comparison of calculated and measured airloads. The drag coefficients in the airfoil tables are corrected to the lower Reynolds number of the 1/4-scale model, using a factor equal to the Reynolds number ratio to the 1/5-power.

There is evidence that rotational effects on the boundary layer produce a delay of separation on rotor blades, particularly for the inboard sections of tiltrotors and wind turbines (references 11 and 12). This stall delay is modelled using input factors K_{sd} to modify the lift and drag coefficients obtained from the airfoil tables:

$$c_l = c_{l \text{ table}} + K_{sdL} (c_{l\alpha}(\alpha - \alpha_z) - c_{l \text{ table}})$$

$$c_d = c_{d \text{ table}} + K_{sdD} (c_{dz} - c_{d \text{ table}})$$

where $c_{l\alpha}$ is the lift-curve slope, and α_z and c_{dz} are the angle of attack and drag coefficient at zero lift. The equations given by Selig (reference 12) are used to evaluate the stall delay factors, which depend on the blade chord

distribution. The values of K_{sd} used in the TRAM analysis are shown in figure 6.

The CAMRAD II rotor wake analysis uses second-order lifting line theory, and the general free wake geometry described in references 9 and 10. For helicopter mode operation (edgewise flight at moderate speed, $\mu = 0.125$ to 0.200), the high twist of the tiltrotor blades results in negative tip loading over most of the advancing side. Hence the dual-peak model must be used, in which the tip vortex is defined by the negative tip loading (not by the maximum positive bound circulation on the inboard part of the blade). A core radius of 20% mean chord is used for the tip vortex. The positive trailed vorticity inboard of the negative tip loading also rolls up in the analysis, with a core radius of 30% mean chord. To avoid having the rollup model respond to small regions of negative loading, the dual-peak model is only used at azimuths where the negative loading extends inboard at least to 0.945R. Two revolutions of wake are used, with calculated free distortion. There is partial entrainment of the trailed vorticity into the tip vortex, such that the final tip vortex strength (achieved after 1/4 revolution of wake age) is 70% of the peak bound circulation on the blade. The distorted wake geometry is calculated for the inboard vorticity as well as for the tip vortices, since inboard rollup is used in the negative tip loading areas. However, distortion of the inboard vorticity is not too important, except when drawing the wake geometry. These wake model features and parameters were determined based on the correlation with measured TRAM performance and airloads, as presented below. The resulting wake model is not the same as the model that has been established for helicopter rotors (references 9 and 10).

Work with helicopter rotors has established the importance of rolled-up tip vortices in the calculation of the blade airloading. The resulting blade-vortex interactions are dominant contributors to noise, vibration, and oscillatory structural loads in low speed flight. The tiltrotor wake model used in this report also has a rolled-up tip vortex, although with partial entrainment as described above. In addition, airloads calculated using a wake model with multiple trailed vortex elements are presented here. Bruce Charles of The Boeing Company (Mesa) determined that such a wake model gives good correlation with the measured airloads. The multiple-trailer wake model has a discrete trailed vortex line emanating from each of the aerodynamic panel edges. The calculation of the free wake geometry in CAMRAD II includes the distortion of all of these trailed lines.

For performance calculations in airplane mode (propeller operation), a single-peak model is used, with full entrainment, and two revolutions of wake. A wake model is needed to calculate the induced power adequately. The

distortion calculated using the free wake geometry model has some influence, but generally the details of the wake rollup are less important than for helicopter mode operation, because the wake is quickly convected axially downstream. At higher speeds than tested in the DNW, the blade loading will be negative inboard (because the twist is less than the optimum for a propeller at high speed). Hence a dual-peak model may be appropriate at higher speeds.

For hover performance calculations, the single-peak wake model is used. The wake model described in reference 10 is used, with four revolutions of wake. The extent of the initial convection is $\tau_K = 0.23$, and the initial span station of the tip vortex is $r_{TV} = 0.97$ (see reference 10 for a full description of these parameters).

Data Reduction and Corrections

The following procedures were used during the DNW test of the TRAM. The nacelle angle was fixed for a particular run. For each data point during a run, the wind tunnel speed, rotor rotational speed, and the rotor shaft angle of attack were set to specified values, and the rotor thrust coefficient C_T set using collective pitch control. Cyclic pitch control was used to achieve zero gimbal tilt (really zero maximum rotating-frame gimbal motion) as indicated on the rotor control console. The rotating-frame gimbal motion was measured and recorded by the data system, so the actual one per-rev gimbal motion (and higher harmonics) is available. Typically the lateral and longitudinal gimbal tilt is less than a few tenths of a degree.

The calculations were performed for specified advance ratio ($V/\Omega R$), tip Mach number, and shaft angle of attack. The analysis trim loop adjusts collective and cyclic to achieve target values of the rotor thrust (C_T/σ) and mean gimbal tilt. The shaft angle of attack values in the analysis correspond to the measured values with wind tunnel wall corrections applied. For comparison of trends with operating condition, involving many measured points, the target thrust is a nominal value and the target gimbal tilt is zero. For comparison with specific data points, the measured thrust and measured one per-rev gimbal tilt are the target trim values for the analysis. Similarly, for trends the operating condition is defined by nominal values of advance ratio, tip Mach number, shaft angle of attack, air density, and temperature; while for specific data points the measured values are used.

All measured quantities were sampled at 64 per-rev, except for the pressure and acoustic measurements, which were sampled at 2048 per-rev. Data were collected for 64 revolutions. The first data sample corresponds to zero azimuth. The results in this report are from a single revolution of data obtained by averaging over the 64

revolutions collected. For performance (loads and power) data, the mean values over this averaged revolution are considered. For structural loads data, the mean and oscillatory (1/2-peak-to-peak) values over the averaged revolution are considered. The time histories of the structural load and airload measurements are corrected for the azimuth shift caused by torque link deflection: $\Delta\psi = Q/11620$, radians, where Q is the measured shaft torque (ft-lb). Thus for a quantity x measured at azimuth ψ the blade is actually at $\psi - \Delta\psi$: $x_{\text{corrected}}(\psi) = x_{\text{measured}}(\psi + \Delta\psi)$. This correction is implemented by using direct and inverse harmonic analysis. For the pitch link loads, link C is on the blade corresponding to the reference azimuth. To bring the loads on the other links into phase with link C, $\Delta\psi + 120$ deg is used in place of $\Delta\psi$ for link A; $\Delta\psi - 120$ deg is used for link B. To eliminate high frequency noise, the airloads data are harmonically analyzed, and 64 harmonics are used to reconstruct the time history (with the $\Delta\psi$ shift) at 256 points in a revolution (reduced from 1024 harmonics representing 2048 samples). All the blade-vortex interaction events in the section normal force data are captured using 64 harmonics.

Table 5 summarizes the sign conventions of the TRAM data. To follow these conventions, the signs are changed for the calculated propulsive force, flap bending moment, and lag bending moment.

The balance and flex-coupling measure the rotor forces and torque. The axes of the balance measurements are the shaft axes. The data reduction process converts these loads to engineering units, subtracts weight tares, and subtracts aerodynamic tares. The results include the rotor thrust T (in shaft axes) and torque Q . Then the shaft angle of attack (measured, without wind tunnel wall correction) is used to transform the forces to rotor lift L and propulsive force X , in wind axes. These quantities are used here in rotor coefficient form:

$$C_T/\sigma = T/\rho(\Omega R)^2 A \sigma$$

$$C_X/\sigma = X/\rho(\Omega R)^2 A \sigma$$

$$C_P/\sigma = P/\rho(\Omega R)^3 A \sigma = Q/\rho(\Omega R)^2 R A \sigma$$

where ρ is the air density, ΩR is the tip speed, A is the rotor disk area, and $\sigma = 0.105$ is the official solidity value (thrust-weighted). The power P equals ΩQ . By definition, VX is the rotor parasite power, so

$$C_P - \mu C_X = C_{P0} = C_{P0} + C_{Pi}$$

is the sum of the induced and profile power ($\mu = V/\Omega R$). The shaft axis forces T and H (positive aft) are transformed to the wind axis forces L and X (positive forward) using the shaft angle of attack α . Thus

$$C_{X0} = C_X + C_T \sin \alpha = -C_H \cos \alpha$$

is the shaft axis rotor propulsive force (times $\cos\alpha$), and nominally the shaft axes are also the tip-path plane axes. Note that wind tunnel wall corrections are applied before $C_{P_{i0}}$ and C_{X0} are calculated. It is useful to compare calculations and measurements for $C_{P_{i0}}/\sigma$ and C_{X0}/σ as well as C_P/σ and C_X/σ , since the former exhibit less variation with shaft angle. In the discussions below, $C_{P_{i0}} = C_P - \mu C_X$ may be referred to as the rotor equivalent drag, although the equivalent drag is actually defined as $C_P/\mu - C_X$.

In the calculations it is possible to separately evaluate the induced power and the profile power. The induced power can be presented as the ratio $\kappa = C_{P_i}/C_{P_{ideal}}$, where $C_{P_{ideal}}$ is the ideal power obtained from momentum theory. The profile power can be presented as an equivalent blade drag coefficient, $c_{d0} = 8C_{P_o}/\sigma$, although in airplane mode this expression does not account for the effect of high axial velocity on the profile power. For hover and airplane mode, both measured and calculated performance can be examined in terms of efficiency parameters. For hover, the figure of merit is defined as $FM = C_{P_{ideal}}/C_P$, where $C_{P_{ideal}} = C_T^{3/2}/\sqrt{2}$. For airplane mode (propeller) operation, the propulsive efficiency is defined as $\eta = P/TV$.

Wind Tunnel Wall Correction

The measured balance loads of the TRAM in the DNW are corrected for the influence of the wind tunnel walls, by using the corrected shaft angle of attack and wind axis propulsive force:

$$\Delta\alpha = \delta \cdot 0.02881 \frac{C_L/\sigma}{\mu^2}$$

$$\alpha_{corrected} = \alpha_{uncorrected} + \Delta\alpha$$

$$C_{X/\sigma} \text{ corrected} = \cos(\Delta\alpha) C_{X/\sigma} - \sin(\Delta\alpha) C_L/\sigma$$

where C_L/σ and C_X/σ are the rotor lift and propulsive force coefficients (rotor coefficient definition, in wind axes), μ is the ratio of wind tunnel speed to rotor tip speed, and $\Delta\alpha$ is the angle of attack correction (positive shaft rearward) in radians. The value of the wall correction constant is $\delta = -0.147$ for the TRAM in the DNW. The correction is thus a decrease in the shaft angle of attack (shaft more forward) relative to the wind, and an increase in the rotor propulsive force. The corresponding correction of the rotor lift is neglected for this test. Also note that if the propulsive force data follow $C_X = C_{X0} - \alpha C_T$, with C_{X0} a constant, then the corrected data fall on the same curve, $C_{Xcorrected} = C_{X0} - \alpha_{corrected} C_T$ (for small $\Delta\alpha$).

The classical wind tunnel wall correction has the form

$$\Delta\alpha = \delta \frac{S}{C} C_L = \delta \frac{L/q}{C}$$

$$= \delta \frac{2A\sigma}{C} \frac{C_L/\sigma}{\mu^2} = \delta \cdot 0.02881 \frac{C_L/\sigma}{\mu^2}$$

with $C_L = L/qS$ (airplane lift coefficient) in the first expression, and $C_L = L/\rho(\Omega R)^2 A$ (helicopter rotor lift coefficient) in the last expression. $A\sigma$ is the rotor blade area, and C is the wind tunnel cross-section area, so $2A\sigma/C = 2\pi R^2\sigma/WH = 0.02881$; using $R = 4.75$ ft, $\sigma = 0.105$; and $W = 8$ m, $H = 6$ m for the DNW open section. The correction constant δ depends on the wind tunnel cross-section shape and the rotor position in the wind tunnel; δ is positive for closed sections and negative for open sections.

Calculations performed by C.L. Burley at Langley Research Center give a value of $\delta = -0.147$, for advance ratios from $\mu = 0.125$ to 0.200 and thrust coefficients from $C_T = 0.009$ to 0.013 . For comparison, the wall correction figures of Pope (figures 6.31 and 6.34 of reference 13) give $\delta = -0.168$ for

$$k = \text{wing span} / \text{tunnel width} = 9.5 \text{ ft} / 8 \text{ m} = 0.362$$

$$\lambda = \text{tunnel height} / \text{tunnel width} = 6 \text{ m} / 8 \text{ m} = 0.75$$

$$d/B = \text{distance above center} / \text{tunnel width} \\ = 0.5 \text{ m} / 8 \text{ m} = 0.0625$$

$$\text{rotor shaft } 0.5 \text{ m to starboard of center}$$

As another example, for a 4 m diameter Bo105 model rotor in the DNW, the Langley Research Center calculations give $\delta = -0.1775$; while Pope's figures give $\delta = -0.158$. Reference 14 shows good results using the Langley Research Center value for the correction factor.

Tare Corrections

Aerodynamic tares are subtracted from the measured rotor forces and torque. Figures 7 and 8 show the tare configurations. For helicopter mode, the blades were removed but the root fairings around the pitch cases were retained (figure 7, shown at airplane mode nacelle angle); the ends of the root fairings were sealed with foam inserts. For airplane mode, both blades and root fairings were removed and a clean spinner was used, without cutouts for the blades (figure 8). The equations for the tare correction of the forces and torque is:

$$\text{measurement} = \text{data} - \text{weight tare} \\ - (\text{aero tare} - \text{aero weight tare})$$

Table 6 defines the tare configurations. The "blades off" configuration is different for the helicopter mode and airplane mode tares (figures 7 and 8). For the tares with the root fairings installed, the pitch setting corresponded to 5 deg collective pitch at 75% radius (about 32 deg pitch of the root fairings). From the measured tare data, analytical functions of shaft angle of attack and airspeed (α and dynamic pressure q ; only α for the weight tare) are

generated by least-squares methods. Then the tares are applied by evaluating these functions at the α and q of the measured data point. The weight tare eliminates the influence of gravity on the balance measurements. Note that the aerodynamic weight tare is obtained with the rotor turning (because it was found that the nonrotating aerodynamic weight tare depended on the hub azimuth). So the aerodynamic tare less the aerodynamic weight tare is zero at zero airspeed (hover).

These tare corrections remove the effects of gravity, the spinner, and (for helicopter mode) the blade root fairings from the measured performance data. The calculated performance (forces and power) does not include the blade weight, and the analysis does not model the spinner. The analysis does include the root fairing, so for helicopter mode it is necessary to apply a tare correction to the calculated performance:

$$\text{calculation} = \text{data} - (\text{aero tare} - \text{aero tare at } q=0)$$

With these tare corrections, the measured and calculated performance data can be directly compared. The calculations must include the root fairing, since the root fairing does influence the wake and the loading on the rest of the blade. The calculated aerodynamic tare is obtained by considering only the root fairing ($r/R = 0.1045$ to 0.2684). The drag data from the cuff airfoil table are used, with zero lift and moment. Stall delay, Reynolds number correction, and unsteady loads are not used; the lift and hence the inflow are negligible. Strip theory applied to the root fairings must be calibrated by matching a measured tare data point. The calibration is accomplished by dividing the airfoil table drag data by the factor K_D . The measured torque for the aerodynamic tare (blades off) at zero airspeed, zero shaft angle, and 1411 rpm is $Q = 11.78$ to 11.89 ft-lb. With $K_D = 2.52$, the calculated torque is $Q = 11.82$ ft-lb. The calculated torque tare (power) is used, but the difference between the aerodynamic tare ($\mu > 0$) and the aerodynamic weight tare ($\mu = 0$) is not large. The calculated propulsive force tare (drag = $-C_X$) has a noticeable effect on the correlation with measured data.

In airplane mode, the tare corrections remove the effects of gravity and a clean spinner from the measured performance data. The measured data therefore include the effects of the blade shanks and the holes in the spinner. The calculated data include none of these effects. So for airplane mode it is appropriate to subtract from the calculated thrust and torque the effects of the blade shanks and the spinner holes. A method to analyze these effects is not available, so the correction is estimated based on correlation with the measured performance. Since the rotational speed at the spinner radius is so much smaller than the flight speed, the correction should involve a thrust decrease proportional to the flight speed squared, and a

small torque increase that is ignored. Based on correlation between measured and calculated performance at $V/\Omega R = 0.350$ and $C_T/\sigma = 0.030$ to 0.035 , a correction of $\Delta C_T/\sigma = -0.011(V/\Omega R)^2$ for the calculated thrust is established. This corresponds to an additional drag of $D/q = 0.164 \text{ ft}^2$. However, the DNW performance measurements in airplane mode only cover a range of $V/\Omega R = 0.325$ to 0.375 , which is probably not sufficient to verify the functional form of this correction.

Zero point data are subtracted from the structural load measurements, in order to remove constant offsets present in the instrumentation: measurement = data – zero data. Actually the subtraction occurs before the conversion to engineering units. The zero point data are measured at the beginning of each run, hence in the same configuration as the data point; with zero airspeed and the rotor not turning, at 5 deg collective and zero shaft angle of attack (for helicopter mode). The zero data are constants for each channel. The load value corresponding to the zero point (caused by the blade weight) could be added to the measurement, but that is not done for this test. So instead the same correction is applied to the calculated structural loads. The constant loads are calculated for the operating condition of the zero point, and then the results are corrected: calculation = data – zero data. This correction is not large.

Airloads Data

The data reduction process for the pressure and airloads measurements is described in reference 3. The pressure coefficient is obtained from the pressure by dividing by the local section dynamic pressure: $c_p = p/(1/2\rho U^2)$. The section velocity U is

$$U^2 = (\Omega r + V \cos \alpha \sin \psi)^2 + (V \sin \alpha)^2$$

where V is the tunnel speed, α the shaft angle of attack (without wall correction), and ψ the blade azimuth angle (without correction for torque link deflection). It follows that the section normal force coefficient, obtained by integrating the pressure coefficients, is $c_n = N/(1/2\rho U^2 c)$; where c is the local chord. Since the operating conditions of interest in this report do not involve significant stall at the measurement locations, it is more interesting to look at the quantity $M^2 c_n = N/(1/2\rho a^2 c)$. Here $M = U/a$ is the section Mach number:

$$\begin{aligned} M^2 &= ((\Omega r + V \cos \alpha \sin \psi)^2 + (V \sin \alpha)^2) / a^2 \\ &= (M_{\text{tip}}^2 r + M_{\text{tun}}^2 \cos \alpha \sin \psi)^2 + (M_{\text{tun}}^2 \sin \alpha)^2 \end{aligned}$$

with $M_{\text{tip}} = \Omega R/a$ the tip Mach number, and $M_{\text{tun}} = V/a$ the tunnel Mach number. The time histories of $M^2 c_n$ presented here include the correction of the azimuth angle for the torque link deflection (applied after using the

nominal azimuth ψ to calculate M^2). The section airloads can be integrated to obtain the rotor thrust:

$$T = \int \frac{1}{2} \rho a^2 c_n (M^2 c_n) dr$$

(dimensional) or

$$C_T = \int \frac{1}{2} M_{tip}^2 (Nc/\pi R) (M^2 c_n) dr$$

(dimensionless), averaged over the rotor azimuth as well. Trapezoidal integration is used over the seven radial stations where c_n is measured, assuming the load is zero at the root cutout and at the tip. In general the difference between the section normal force N and the shaft axis vertical force that gives the thrust is considered, by including the cosine of the section pitch angle in the integrand. For helicopter mode this difference is not large. A comparison of the rotor thrust measured by the balance with the rotor thrust obtained by integrating the blade pressure measurements shows that the thrust from the airloads is consistently lower than the thrust from the balance, by 15 to 19%. The balance measurement of rotor thrust is considered accurate. Based on comparison of the radial distribution of mean airloads from measurements and from calculations, it is concluded that the mean section normal force measurements at 0.82R and inboard are too small. The cause of this difference is not known. Examination of the chordwise pressure distributions at the seven radial stations does not suggest any problem.

DNW Test Results

The operating conditions of the TRAM in the DNW covered helicopter mode, airplane mode, and hover. The rotor shaft angle of attack is positive aft, around zero for helicopter mode and around -90 deg for airplane mode. The tip Mach number M_{tip} is the ratio of the rotor tip speed to the speed of sound. The advance ratio μ is the ratio of the tunnel speed to the rotor tip speed, regardless of the shaft angle. The helicopter mode test points are for nominal advance ratios of $\mu = 0.125, 0.150, 0.175, 0.200$; nominal thrust coefficients of $C_T = 0.009, 0.011, 0.013$; at shaft angles from -14 deg to 12 deg. Figure 9 shows the actual advance ratio and thrust values tested; and the shaft angle of attack (with wall corrections) for $C_T = 0.009$ and 0.013 . The airplane mode test points are for nominal advance ratios of $\mu = 0.325, 0.350, 0.375$; at shaft angles from -95 deg to -85 deg. Figure 10 shows the actual advance ratio and thrust values tested in airplane mode. Hover tests were conducted in both helicopter mode and airplane mode (shaft angle of 0 and -76 deg respectively, with the tunnel circuit 90% blocked for airplane mode), at thrusts up to approximately $C_T/\sigma = 0.17$. Figure 11 shows the actual tip Mach numbers and rotor thrusts for the hover tests.

The TRAM test results from the DNW consist of a total of 1617 points. Data points with rotor speed less than 1300 rpm, thrust or power less than zero, or hover figure

of merit greater than 1.0 are discarded. There remain 1489 good data points. The points are sorted based on advance ratio, tip Mach number, and shaft angle. After discarding isolated points, there are 1456 sorted, good points. For structural loads, only sorted good points from the performance filter are considered. For each bending, torsion, or pitch link gage, specific runs and points are discarded based on mean or oscillatory load value being outside trends with operating condition. Because of instrumentation difficulties, particularly damage to wiring, the structural loads data were lost for 15 to 31% (depending on the channel) of the 1072 points in helicopter mode at $C_T/\sigma = 0.089$ and 0.128 . However, the remaining data are sufficient to establish the behavior of the structural loads.

Pressure data were acquired for 463 points. There are 434 data points after discarding static points: 330 helicopter mode, 37 airplane mode, and 67 hover. Because of instrumentation difficulties, including damage to wiring and data acquisition problems, an increasing number of pressure channels were lost as the test progressed (although the gages are still good). Helicopter mode airloads data from runs 603–607 (early in the test) are examined in this report. Runs 603–607 contain 98 of the 330 helicopter mode pressure points. Of the 135 pressure gages operational at the start of the test, 3 to 19 (average 12) were bad during these runs; 91% of the channels were good. So during 40% of the points in these runs, the section normal force is not available at one of the seven radial stations; 94% of the c_n measurements were good. During airplane mode runs (at the end of the test), only 49% of the c_n measurements were good. In this context, a good measurement means simply that at least four upper surface and four lower surface pressure gages are operational at a radial station. For hover and for airplane mode cruise conditions, the airloads data were edited by discarding c_n values that are clearly outside trends with thrust or with radial station. In airplane mode, there remain 23 points (all at -90 deg shaft angle of attack), with 49% of the c_n values good. In hover, the edited points include 16 points (from early in the test) with c_n values at all seven radial stations.

For detailed examination of the airloads and structural loads in helicopter mode forward flight, twelve points were selected. The nominal operation condition is advance ratio $V/\Omega R = 0.15$, rotor thrust $C_T/\sigma = 0.089$ and 0.128 , shaft angle of attack from -10 deg (forward) to $+10$ deg (aft). Table 7 gives the details of the measured operating condition for these twelve points. The corrected shaft angle of attack includes the effect of the wind tunnel walls; the rotor propulsive force C_X/σ is the corrected value. The azimuth correction $\Delta\psi$ accounts for the torque link deflection. The gimbal tilt is obtained from the first harmonics of the measured gimbal deflection. The

longitudinal gimbal tilt β_{1c} is positive forward; the lateral gimbal tilt β_{1s} is positive towards the advancing side. For each of the twelve operating conditions examined, airloads data are available for several points (at least three points, as many as eight points). The airloads data from different points at the same operating condition exhibit little difference.

Correlation Results

The following sections present the results of CAMRAD II calculations compared to the TRAM DNW measurements for hover performance; airplane mode performance; helicopter mode performance; helicopter mode airloads; and helicopter mode blade structural loads. More extensive results of this investigation, including helicopter and airplane mode airloads, are given in reference 15.

Hover Performance

The TRAM hover performance measured in the DNW is shown in figure 12, in terms of rotor power and figure of merit as a function of rotor thrust. The hover tests were conducted in helicopter mode (zero shaft angle of attack) at $M_{tip} = 0.62$ to 0.63 , and in airplane mode (-76 deg shaft angle of attack, tunnel circuit 90% blocked) at $M_{tip} = 0.62$ and 0.58 (see figure 11). The results for these three operating conditions are different, which is not unexpected considering the difficulties involved in performing hover measurements in a wind tunnel, even with an open test section. The airplane mode configuration was anticipated to be better for hover, since blockage from the model support is minimized in this configuration.

Because of these differences in the TRAM measurements, hover correlation begins instead with data from the test of a 0.658-scale model of the JVX rotor (an early version of the design that became the V-22). The JVX hover test results are given in reference 16. The rotor radius was 12.5 ft (XV-15 radius). The JVX blades had the same twist, taper, and thickness-to-chord ratio as the V-22 blades, but with 8.4% larger chord (solidity of $\sigma = 0.1138$ instead of 0.105). The hub was gimbaled, but was an XV-15 hub with 2.5 deg of precone, not a scaled V-22 hub (hence without the effective flap and lag hinge at the inboard centering bearing as on the TRAM model). The JVX blades used the XN28, XN18, XN12, XN09 airfoils at radial stations $r/R = 0.09, 0.50, 0.75, 1.00$ respectively. The JVX blades had a root cutout of about $0.1R$, without the cuff of the V-22 and TRAM blades. Hence the JVX chord and twist are similar to the TRAM values shown in figure 2, but with the chord increased by a factor 1.084 and the linear taper extending to the root cutout; and the twist linear from $0.3R$ inboard to the root cutout. Figure 12 compares the measured JVX and TRAM hover performance. The JVX data are for $M_{tip} = 0.68$ and wind

speeds below 0.5 m/sec (1 knot); see figure 18a of reference 16.

The TRAM blades have a smaller chord and smaller Reynolds number compared to the JVX blades. The solidity σ is reduced by the factor $f_\sigma = 1/1.084$. The drag is increased by approximately the Reynolds number ratio to the 1/5-th power, a factor of about $f_d = 1.21$ in this case. Blade element theory gives $C_P = \kappa C_T^{3/2} \sqrt{2} + \sigma c_d/8$. At constant C_T it is expected that the TRAM rotor has higher C_P than the JVX rotor. The profile power is reduced by the smaller chord and increased by the smaller Reynolds number. The net factor on profile power is $f_\sigma f_d = 1.12$, an increase since the drag effect dominates. At constant C_T/σ the TRAM rotor has about the same C_P/σ as the JVX rotor. The reduction of the induced power by the factor $\sqrt{f_\sigma} = 1/1.04$ is offset by the increase in the profile power by the factor $f_d = 1.21$. At constant C_T/σ the figure of merit of the TRAM rotor is reduced by both effects, since the ratio of profile power to ideal induced power is increased by the factor $f_d/\sqrt{f_\sigma} = 1.26$. Based on these estimates, it is clear that the TRAM helicopter mode hover performance measurements are not accurate. In particular, the TRAM figure of merit is about the same as the JVX figure of merit in helicopter mode (figure 12), but in airplane mode it is reduced as expected.

The measured and calculated JVX hover performance are compared in figure 13. The calculated peak figure of merit matches the measured data well, but the calculated power is too large at the lowest thrust shown, and too small at the highest thrust. Figure 13 also shows the influence of the aerodynamic and wake parameters of the analysis on the calculated JVX hover performance. The stall delay has a major influence on the calculated performance. Without the stall delay, the induced power is larger at high thrust and the profile power is much larger, with the result that the figure of merit is much too low at moderate and high thrust. The drag stall delay has some influence, but most of the effect is from the lift stall delay. The lift stall delay allows the inboard sections of the blade to produce more lift and thus the outboard sections less lift at a given thrust. This lift redistribution is small, but sufficient to significantly reduce the induced and profile losses at the tip. Two wake parameters are also observed to influence the calculated performance: using five wake revolutions instead of four, or using an initial span station of the tip vortex of $r_{TV} = 0.99$ instead of 0.97. Both of these changes increase the induced power. Model features that did not influence the results include changing the extent of the initial convection τ_K ; tip vortex core radius or radius growth; or using the JVX instead of the EMD airfoil tables.

The measured and calculated TRAM hover performance are compared in figure 14. Compared to the JVX rotor, the

reduction in chord reduces the power, and the lower Reynolds number significantly increases the power and reduces the figure of merit. As for the JVX rotor (figure 13), the calculated peak figure of merit matches the data well, but the calculated power is too large at the lowest thrust shown, and too small at the highest thrust. The stall delay has a significant influence on the shape of the power and figure of merit as a function of thrust. The method used to calculate the stall delay factors (from reference 12) apparently produces too much stall delay. Figure 14 shows calculations for both rigid and elastic blades. Blade flexibility has little effect on the calculated performance.

Airplane Mode Performance

The TRAM airplane mode performance measured in the DNW is shown in figure 15, in terms of rotor power and propulsive efficiency as a function of rotor thrust. The performance data are for advance ratios of $V/\Omega R = 0.325, 0.350, 0.375$; only measurements for axial flow (shaft angle of attack of -90 deg) are considered here. Figure 15 also shows the calculated performance, for a rigid blade and with the spinner tare correction. The calculated power and propulsive efficiency match the measured data well. At low speed or low thrust, the induced power is much higher than the momentum theory value, because the blade twist distribution is far from ideal for these operating conditions. Figure 16 shows the influence of blade elasticity and the spinner tare correction on the calculated airplane mode performance. Blade flexibility has little effect on the calculated performance. Without the spinner tare correction (applied to the calculated thrust, as described above), the calculated propulsive efficiency is too high. At these low advance ratios, the influence of advance ratio on the calculated propulsive efficiency observed in figure 15 is produced by the spinner tare correction. Using the JVX instead of the EMD airfoil tables produces a change in profile power that is too small to significantly influence the total power or the propulsive efficiency.

Helicopter Mode Performance

The TRAM helicopter mode performance measured in the DNW is shown in figures 17 and 18, in terms of rotor power, equivalent drag, propulsive force, and inplane force, as a function shaft angle of attack for two rotor thrust values and four advance ratios. Most of the reduction of power as angle of attack increases is accounted for by the parasite power (μC_X), but the equivalent drag still shows a decrease with angle of attack, indicating that the tiltrotor (like the helicopter rotor) becomes more efficient as the propulsive force is reduced. The power increases with thrust, and decreases with advance ratio, as expected at low speed. Most of the variation of the propulsive force with shaft angle of attack and thrust is accounted for by the tilt of the thrust vector with the shaft (α_{CT}), so the shaft-axis

inplane force is a relatively constant drag value. Figures 19 and 20 compare the measured helicopter mode performance with calculations using a rigid blade model and the aerodynamic model described above. The calculated power generally matches the measurements well, although the calculated power is too low at low thrust and the middle of the angle of attack range; and the slope with angle of attack is somewhat too small for $\mu = 0.15$ and high thrust. In addition, the calculated power is somewhat erratic, reflecting the complexity of the wake at these operating conditions. The calculated propulsive force matches the data well, which is the reason that differences between measurement and calculation are similar for power and equivalent drag.

Figure 21 compares the measured performance with and without the wind tunnel wall correction (plotted as a function of the corrected and uncorrected shaft angle of attack respectively). The wind tunnel wall correction results in a reduction in the power and equivalent drag. The correction implies a larger propulsive force at a given uncorrected angle of attack, hence more of the total power is attributed to parasite losses, and the equivalent drag (induced plus profile power) decreases. The propulsive force as a function of angle of attack is not significantly affected by the correction. Figure 22 compares the calculated helicopter mode performance and measurements without the wind tunnel wall correction. Because the uncorrected measured power is higher, the correlation with calculations is not good. Figure 23 compares the calculated performance with and without the analysis tare correction. The analysis tare for the total power (rotor torque) is small. The analysis tare significantly increases the calculated propulsive force, particularly at the higher speeds (the tare is a drag value), hence decreases the calculated rotor equivalent drag. Figure 24 compares the measured helicopter mode performance and calculations without the analysis tare correction. The correlation is nearly the same for the total power, but without the analysis tare the calculated equivalent drag is too high, and does not decrease as much with angle of attack; and the slope of the propulsive force as a function of angle of attack is too large. So both the wind tunnel wall correction and the analysis tare correction are required for best correlation between measured and calculated performance.

The influence of the aerodynamic model on the calculated TRAM helicopter mode performance for $\mu = 0.15$ is examined in figure 25. Without the Reynolds number correction of the drag from the airfoil tables, the calculated power is too low. Without the stall delay model, particularly for the lift, the calculated power is much too high, especially at the higher thrust. Without the stall delay model, the equivalent drag actually increases with angle of attack, because of an increase in the stall at the

blade root. As for hover, the stall delay model is required for accurate calculation of the tiltrotor performance in helicopter mode forward flight. Note however that at low thrust and the middle of the angle of attack range, the induced power is higher, perhaps more realistic, without the stall delay (reflecting the influence on the wake of the lift distribution changes produced by the stall delay model). This implies that a better stall model is needed.

The influence of the wake model on the calculated TRAM helicopter mode performance for $\mu = 0.15$ is examined in figure 26. The wake model for the baseline uses the dual-peak wake model, to accommodate the negative loading on the advancing tip of the blade in helicopter mode; partial entrainment of the trailed vorticity into the tip vortex, such that the final tip vortex strength (achieved after 1/4 revolution of wake age) is 70% of the peak bound circulation on the blade; two revolutions of wake; and a search for the circulation peak only inboard of 0.945R, to avoid having the rollup model respond to small regions of negative loading. Using three revolutions of wake, or unrestricted search for the circulation peak, does not change the calculated performance significantly. However, unrestricted search for the circulation peak results in a calculated induced power that is unreasonably low. Using the single-peak wake model increases the calculated power for low thrust, where there is significant negative loading of the blade tip. Using complete entrainment of the tip vortex increases the calculated power for high thrust. For both of these effects, the source of the power increase is a substantial increase of the induced power. The ratio of the tip vortex strength to the peak bound circulation (70% here) is a fixed parameter in this model. It is likely that this ratio actually varies with azimuth.

Through extensive correlation of CAMRAD II calculations with performance and airloads measurements, an aerodynamic and wake model appropriate for most helicopters has been developed (refs. 8 to 10). Figure 27 compares the measured TRAM helicopter mode performance with calculations using this helicopter aerodynamic and wake model, and with calculations using the tiltrotor aerodynamic and wake model documented in this report. The primary differences are that the helicopter model does not include the stall delay, and uses complete entrainment of the tip vortex, three revolutions of wake, and unrestricted search for the circulation peak. For both the tiltrotor and helicopter models, the dual-peak wake model is used, since there is significant negative loading on the rotor blade. At high thrust, the calculated power is much too large with the helicopter model. This power increase is caused by increases both in profile power (without the stall delay) and in the induced power (with complete rollup). At low thrust the induced power is unreasonably low with the helicopter model (less than the

ideal momentum theory value), while the profile power is increased. So at low thrust, the power calculated using the helicopter model shows good correlation with the measured power only because of canceling errors in the calculated induced and profile power. The span loading and wake formation are very different on tiltrotors and helicopters, so it is essential to use model features specific to tiltrotors in order to adequately predict the behavior. The high twist of the tiltrotor blade generally means that the peak bound circulation is not near the tip, implying a partial rollup of the trailed vorticity into the tip vortex. The delay of stall by rotational effects on the inboard blade sections is an aerodynamic phenomenon that should exist on helicopters as well as on tiltrotors. With the low twist of helicopter blades, the angle of attack is not high enough on the inboard part of the blade for the stall delay to have a significant role in redistributing the lift load over the rotor disk.

Helicopter Mode Airloads

The blade section airloads ($M^2 c_n$) measured in helicopter mode are presented in figures 28 and 29, for the twelve points at advance ratio $\mu = 0.15$ selected for detailed examination. Each figure shows the airloading as a function of azimuth angle, for all twelve points (six shaft angles and two thrusts), for one of the seven radial stations where the blade pressures are measured. Figures 28 and 29 also show the calculated airloads, obtained using the multiple-trailer wake model and the rolled-up wake model respectively (with elastic blade). The measured airloads show significant blade-vortex interaction at the tip for all twelve conditions, at both high and low thrust, and at both positive and negative shaft angles. There is a substantial region of negative loading on the advancing blade tip, particularly at low thrust. The calculated and measured airloads compare very well using the multiple-trailer wake model (figure 28). The measured airloads integrate to a smaller rotor thrust, so the calculated airloads tend to have a larger mean value. Bruce Charles of The Boeing Company (Mesa) determined that the multiple-trailer wake model of CAMRAD II gives good correlation with the measured airloads.

The calculations using the rolled-up wake model (figure 29) capture the overall character of the airloads, but there are significant differences in the details. The calculated and measured blade-vortex interaction are similar on the retreating side, but different on the advancing side. At low thrust, for the calculated and measured advancing side blade-vortex interaction the amplitudes match, but not the azimuth at which the interaction occurs. At high thrust, the azimuths of the advancing side interaction are similar, but the calculated amplitude of the interaction is somewhat larger than the measured interaction for negative shaft

angles (forward), and much larger for positive shaft angles (aft). The region of negative loading on the advancing tip is well calculated at low thrust, except that the loading occurs in the calculations at 20 or 30 deg earlier azimuth angle than in the measurements. At high thrust, the calculated loading in the second quadrant of the disk is higher than the measured loading. The calculated airloads at low thrust and -10 deg shaft angle do not follow the trend of the other shaft angles, particularly for azimuth angles from 45 to 135 deg, reflecting a change in character of the calculated wake geometry. The tip vortex core size in the analysis has little influence on the major discrepancies between calculated and measured airloads.

Compared to the airloads calculated using the tiltrotor aerodynamic and wake model, the helicopter model (not shown in the figures) produces larger blade-vortex interaction amplitude on the retreating side, smaller blade-vortex interaction amplitude on the advancing side for positive shaft angles, and larger peak airloads on the rotor disk.

There is little influence of the blade elastic motion on the calculated performance or on the calculated airloads. Figure 30 shows the calculated elastic pitch and elastic twist motion of the blade. The quantity presented as elastic twist is the difference between the blade pitch at the tip and at the pitch bearing. The root pitch value is the rotation of the pitch bearing, with the mean and one per-rev removed since these harmonics correspond to the trim of the rotor. The calculated elastic twist has a one per-rev amplitude of about 0.2 deg, plus a small amplitude at 7 to 9 per-rev, evidently associated with the calculated torsion mode frequency. The root pitch motion has a 3 per-rev amplitude of up to 0.2 deg, probably associated with the second flap mode. The calculated elastic flap motion for these conditions (not shown) is primarily one per-rev, with amplitudes from 0.01 to 0.02 deg.

The measured airloads and the airloads calculated using the multiple-trailer wake compare very well. The airloads calculated using the other wake models differ significantly from the measurements. The wake geometry calculated for the multiple-trailer wake exhibits rollup of the outboard lines into a tip vortex, but because of the spanwise resolution and the absence of viscous effects, a highly concentrated tip vortex is not produced. In contrast, measurements of the TRAM flow field show distinct rolled-up vortex structures, including both positive and negative vortices at low thrust (ref. 17). These measured vortices have core radii from 25 to 50% chord and corresponding strength from 60 to 20% of the peak bound circulation, after at least one revolution of wake age. The vortices produce high-frequency oscillations in the measured airloads (figure 28), that this multiple-trailer wake model can never produce. In addition, the induced

power is larger with the multiple-trailer model, so the performance correlation is not as good as with the rolled-up wake model. It is concluded from these results that while the tiltrotor wake does roll up into concentrated vortices, the rollup process is occurring over a wake age of several revolutions.

Helicopter Mode Structural Loads

The TRAM helicopter mode blade structural loads measured in the DNW are compared with the loads calculated using the baseline elastic blade model in figures 31 to 35. Each figure presents the mean and oscillatory (one-half peak-to-peak) loads as a function shaft angle of attack for two rotor thrust values and four advance ratios. The mean and oscillatory flap bending moments (figure 31) and lag bending moments (figure 32) increase with thrust (except for mean lag moment) and exhibit some variation with shaft angle; no clear variation with speed is seen over the range tested. The oscillatory torsion moments (figure 33) and pitch link forces (figure 34) increase with thrust, and at high thrust exhibit a peak around a shaft angle of $\alpha = -2$ deg; no clear variation with speed is seen over the range tested. The oscillatory pitch link loads are similar for the three blades (figure 35). The mean torsion moments inboard (figure 33) and the mean pitch link forces (figures 34 and 35) exhibit much scatter and differences between blades, probably associated with adjustments made during the test to maintain track and balance. The calculated mean and oscillatory loads show variations with thrust and shaft angle that are comparable to the variations in the measured data. The calculations show variations of the loads with speed that are somewhat larger than measured.

The influence of the blade structural model on the calculated loads for $\mu = 0.15$ is shown in figures 36 to 41. The structural model variations considered are a stiffer blade root (stiffer flap and lag hinge springs at the inboard centering bearing, and stiffer pitch link; see table 4); nonzero tension center offset inboard of $r = 0.5R$; and zero pitch bearing damping. The calculated oscillatory and mean flap loads (figures 36 and 37) match the measured data well, although the oscillatory flap loads are low at the root for high thrust and negative shaft angle. For high thrust, the mean loads increase with the stiffer root, which improves the correlation with measured loads; but the oscillatory loads decrease with the stiffer root, resulting in worse correlation. The calculated oscillatory lag loads (figures 38 and 39) are too small. The calculated mean lag loads match the data well, except for $r = 0.365R$ (not shown). The calculated oscillatory lag loads are increased with the stiffer blade root, resulting in much improved correlation. The spring constant of the effective lag hinge at the inboard centering bearing is not well established by the available nonrotating frequency and deflection

measurements. Evidently a larger value than the baseline lag spring constant gives a better model of the TRAM. The calculated oscillatory torsion loads (figure 40) and pitch link loads (figure 41) generally match the measured data well, except that the calculations do not show the measured peak around a shaft angle of $\alpha = -2$ deg. The calculated mean torsion and pitch link loads do not compare well with the measured loads, but the measured mean loads exhibit substantial scatter and differences between blades. With a nonzero inboard tension center, the calculated mean flap loads (figure 36) and calculated mean lag loads (figure 39) are substantially changed, resulting in poor correlation with measured loads. The only influence observed for the pitch bearing damping is on the oscillatory pitch link loads. Without the pitch bearing damping, the calculated oscillatory pitch link loads are much too small.

The measured and calculated blade structural loads are presented in figures 42 to 47, for the twelve points at advance ratio $\mu = 0.15$ selected for detailed examination. Each figure shows one of the loads as a function of azimuth angle, for all twelve points (six shaft angles and two thrusts). Generally the measured and calculated loads exhibit similar behavior. The calculated flap bending moment (figure 42) and lag bending moment (figure 44) inboard at high thrust do not show the increase around 140 deg azimuth that is observed in the measurements. This difference undoubtedly is associated with the differences between measured and calculated spanwise airloading. The abscissa scales for measured and calculated loads are shifted in figures 46 and 47, because of the difference in mean values. The measured and calculated torsion loads both show significant high harmonic content. The measured torsion loads however show more 3 per-rev variation than calculated (figure 46). The amplitude and phase of the calculated pitch link loads match the data well (figure 47). The value of the pitch bearing damping was determined by matching the amplitude of oscillatory pitch link loads (figure 41). With this damping, the one per-rev motion of the pitch bearing results in a pitch link load. While the value of the pitch bearing damping has not been independently measured, the fact that the measured and calculated pitch link load have the same phase and are both primarily one per-rev (figure 47) confirms that the pitch bearing damping is a reasonable source of the pitch link loads.

Conclusions

Comparisons of measured and calculated aeromechanics behavior of a tiltrotor model have been presented. The measured data are from the test of the Tilt Rotor Aeroacoustic Model (TRAM) with a single, 1/4-scale V-22 rotor in the German-Dutch Wind Tunnel (DNW). This

report has summarized the TRAM model and the DNW test, and presented the measured data. The calculations were performed using the rotorcraft comprehensive analysis CAMRAD II. The comparison of measurements and calculations includes helicopter mode operation (performance, airloads, and blade structural loads), hover performance, and airplane mode performance.

The CAMRAD II aerodynamic model uses second-order lifting-line theory with a vortex wake calculation of the induced velocity, and a free wake geometry calculation. For these tiltrotor calculations, the blade aerodynamic model includes a correction of the airfoil drag for Reynolds number, and a model for the stall delay on inboard blade sections that is caused by rotational effects on the boundary layer. Because of the negative loading encountered on the advancing blade tip in helicopter mode, a dual-peak wake model is used, in which the tip vortex is defined by the negative tip loading (not by the maximum positive bound circulation on the inboard part of the blade). To avoid having the rollup model respond to small regions of negative loading, the dual-peak model is only used at azimuths where the negative loading extends inboard at least to 0.945R. Two revolutions of wake are used, with calculated free distortion. There is partial entrainment of the trailed vorticity into the tip vortex, such that the final tip vortex strength is 70% of the peak bound circulation on the blade. In addition to this rolled-up wake model (with partial entrainment), a wake model with multiple trailed vortex elements is also used for the airloads calculations. The multiple-trailer wake model has a discrete trailed vortex line emanating from each of the aerodynamic panel edges, with the distortion of all of these trailed lines included in the free wake geometry calculation.

This model for tiltrotor calculations was developed based on the present correlation with measured TRAM performance and airloads. The CAMRAD II aerodynamic and wake model that has been found appropriate for helicopter rotors is different. The primary differences are that the helicopter model does not include the stall delay, and uses complete entrainment of the tip vortex, three revolutions of wake, and unrestricted search for the circulation peak.

The comparison of measured and calculated behavior demonstrates that accurate calculation of tiltrotor performance requires a nonuniform inflow and free wake geometry model, in hover, cruise, and helicopter mode operation. With momentum theory or a prescribed wake geometry, the induced power is not calculated accurately, and the detailed airloading changes can not be captured. The effect of blade flexibility on the calculated performance was small. Some influence of blade flexibility on the calculated blade airloads was observed, reflecting more the sensitivity of the wake model rather than large elastic deflection.

In hover, the important model features are the stall delay, the wake extent, the initial span station of the tip vortex formation, and the Reynolds number correction. As observed in other investigations, without the stall delay, the induced power is larger at high thrust and the profile power is much larger, with the result that the figure of merit is much too low at moderate and high thrust. The drag stall delay has some influence, but most of the effect is from the lift stall delay. The lift stall delay allows the inboard sections of the blade to produce more lift and thus the outboard sections less lift at a given thrust. This lift redistribution is small, but sufficient to significantly reduce the induced and profile losses at the tip. The calculated peak hover figure of merit matches the measured data well, but the calculated power is too large at the lowest thrust considered, and too small at the highest thrust. The stall delay has a significant influence on the variation of the power and figure of merit with thrust. It is concluded that an improved method to calculate the stall delay factors is required.

In airplane mode, the calculated power and propulsive efficiency match the measured data well, when the appropriate spinner tare correction is used.

In helicopter mode, important model features are the stall delay, the Reynolds number correction, the dual-peak wake model with restricted search for the circulation peak, the wake extent, and the tip vortex formation. Good correlation of measured and calculated performance is achieved, when the wind tunnel wall correction of the measurements and an analysis tare correction are used. The helicopter aerodynamic and wake model does not give adequate performance calculations. The measured airloads and the airloads calculated using the multiple-trailer wake compare very well. However, the multiple-trailer wake does not produce the rolled-up vortex structures observed in the TRAM flow field measurements and implied by the measured high frequency airload variations. In addition, the induced power is larger with the multiple-trailer model, so the performance correlation is not as good as with the rolled-up wake model. Considering the entire range of operating conditions examined, it is clear that the stall delay and tip vortex formation models are too simple. The stall delay is defined by constants that are just a function of radius. The ratio of the tip vortex strength to the peak bound circulation is a constant that is applied to the wake at all azimuths. For both effects, the same parameter values were used for all operating conditions. A rational means to define the parameters as a function of operating condition would be useful. The good airloads correlation using the multiple-trailer wake model implies that while the tiltrotor wake does roll up into concentrated vortices, the rollup process is occurring over a wake age of several revolutions.

In helicopter mode, the calculated mean and oscillatory blade structural loads generally match the measured data well. The value of the effective lag spring at the inboard centering bearing is important for the oscillatory lag bending loads. The tension center offset has a significant influence on the mean flap and lag bending loads. The pitch bearing damping produces a large contribution to the oscillatory pitch link loads. There are differences between the measured and calculated load time histories that reflect the differences between the measured and calculated airloads.

In summary, an aerodynamic and wake model and calculation procedure that reflects the unique geometry and phenomena of tiltrotors has been developed. There are major differences between this model and the corresponding aerodynamic and wake model that has been established for helicopter rotors. In general good correlation between measured and calculated aeromechanics behavior has been shown, but significant differences remain in the detailed behavior. Two aspects of the analysis that clearly need improvement are the stall delay model and the trailed vortex formation model.

This investigation has covered several facets of rotorcraft analytical model development. The calculation of rotor aeromechanics behavior commonly requires nonuniform inflow and free wake geometry, and the importance of a dual-peak wake model in the presence of negative tip load is understood from helicopter calculations. Wall corrections and tare corrections are standard techniques when dealing with wind tunnel data. The influence of blade flexibility on performance and airloads depends on the particular rotor design. The examination of the effects of root stiffness, tension center offset, and pitch bearing damping on the structural loads reflects not unusual uncertainties in the physical properties of the rotor. A Reynolds number correction is normally required for models at this scale. The wake extent, wake rollup, and inboard stall delay are features of the model that represent specific physical aspects of rotor aerodynamics. These features are represented directly, but quite simply, in the aerodynamic and wake model. One result of the correlation is to establish values of the parameters that define these features in CAMRAD II. The more general results of the correlation are to establish the key importance of these features for tiltrotor aeromechanics behavior, and the need for improved models. A first-principles solution for rotor aerodynamics is the long term goal. Until that is available, more accurate and more general models of the stall delay and the trailed vortex formation are needed. Acquisition of additional detailed aerodynamic measurements will be needed to support such model development.

Although the tiltrotor model developed in this investigation is considered generic, these calculations must be repeated for other tiltrotor configurations in order to establish the generality of the models. Two candidates for additional comparison between measured and calculated tiltrotor aeromechanics behavior are the test of the full-span TRAM in the Ames Research Center 40- by 80-Foot Wind Tunnel, which will offer an extended range of operating conditions as well as the full-span configuration; and the helicopter mode test of an isolated, full-scale XV-15 rotor in the Ames Research Center 80- by 120-Foot Wind Tunnel.

Acknowledgments

The experimental results in this paper were derived from research performed under the auspices of the Tilt Rotor Aeroacoustic Model (TRAM) project and the NASA Short Haul Civil Tiltrotor (SHCT) project. The TRAM and SHCT projects are led at NASA Ames Research Center by the Army/NASA Rotorcraft Division and the Advanced Tiltrotor Technology Project Office, respectively. Other major funding partners and research participants in the experimental research effort were the U.S. Army Aeroflightdynamics Directorate (AFDD) located at Ames, the Acoustics Division of NASA Langley Research Center, and The Boeing Company (Mesa). In addition, the outstanding support provided by the German-Dutch Wind Tunnel (DNW) staff during the execution of the wind tunnel test was crucial to the success of the test.

References

- 1) Young, L.A. "Tilt Rotor Aeroacoustic Model (TRAM): A New Rotorcraft Research Facility." Heli Japan 98: AHS International Meeting on Advanced Rotorcraft Technology and Disaster Relief, April 21–23, 1998, Nagarafukumitsu, Gifu, Japan.
- 2) Young, L.A.; Booth, E.R., Jr.; Yamauchi, G.K.; Botha, G.; and Dawson, S. "Overview of the Testing of a Small-Scale Proprotor." American Helicopter Society Annual Forum, Montreal, Canada, May 1999.
- 3) Swanson, S.M.; McCluer, M.S.; Yamauchi, G.K.; and Swanson, A.A. "Airloads Measurements from a 1/4-Scale Tiltrotor Wind Tunnel Test." European Rotorcraft Forum, Rome, September 1999.
- 4) Ames Research Center. "TRAM Physical Description." NASA Report (to be published).
- 5) Jenks, M.D., and Narramore, J.C. "Final Report for the 2-D Test of the Model 901 Rotor and Wing Airfoils (BSWT 592)," Boeing Report D901–99065–1, June 1984.
- 6) Johnson, W. "CAMRAD II, Comprehensive Analytical Model of Rotorcraft Aerodynamics and Dynamics." Johnson Aeronautics, Palo Alto, California, 1992–1999.
- 7) Johnson, W. "Technology Drivers in the Development of CAMRAD II." American Helicopter Society, Aeromechanics Specialists Meeting, San Francisco, January 1994.
- 8) Johnson, W. "Rotorcraft Aeromechanics Applications of a Comprehensive Analysis." Heli Japan 98: AHS International Meeting on Advanced Rotorcraft Technology and Disaster Relief, April 21–23, 1998.
- 9) Johnson, W. "A General Free Wake Geometry Calculation for Wings and Rotors." American Helicopter Society Forum, May 1995.
- 10) Johnson, W. "Rotorcraft Aerodynamics Models for a Comprehensive Analysis." American Helicopter Society Forum, May 1998.
- 11) Corrigan, J.J., and Schillings, J.J. "Empirical Model for Stall Delay Due to Rotation." American Helicopter Society Aeromechanics Specialists Conference, San Francisco, January 1994.
- 12) Du, Z., and Selig, M.S. "A 3-D Stall-Delay Model for Horizontal Axis Wind Turbine Performance Prediction." AIAA Paper 98–0021, January 1998.
- 13) Pope, A. *Wind Tunnel Testing*, Second Edition, John Wiley and Sons, Inc., New York. 1954.
- 14) Langer, H.-J.; Peterson, R.L.; and Maier, T.H. "An Experimental Evaluation of Wind Tunnel Wall Correction Methods for Helicopter Performance." American Helicopter Society Forum, Washington, D.C., June 1996.
- 15) Johnson, W. "Comparison of Measured and Calculated Aeromechanics Behavior of the Tilt Rotor Aeroacoustic Model (TRAM) in the DNW." NASA Report (to be published).
- 16) Felker, F.F.; Signor, D.B.; Young, L.A.; and Betzina, M.D. "Performance and Loads Data From a Hover Test of a 0.658-Scale V-22 Rotor and Wing." NASA TM 89419, April 1987.
- 17) Yamauchi, G.K.; Burley, C.L.; Mercker, E.; Pengel, K.; and JanakiRam, R. "Flow Measurements of an Isolated Model Tilt Rotor." American Helicopter Society Forum, Montreal, Canada, May 1999.

Table 1. Principal physical characteristics of the TRAM model.

blade	
blade radius R	4.75 ft
solidity σ (thrust weighted)	0.105
number of blades	3
100% rpm, helicopter	$\Omega = 1588$ rpm $\Omega R = 789.90$ $M_{tip} = 0.708$
100% rpm, airplane	$\Omega = 1331$ rpm $\Omega R = 662.06$ $M_{tip} = 0.593$
airfoil sections	XN28, XN18, XN12, XN09
hub	
gimballed, trailing pitch link	
gimbal undersling	0.0273 R
precone	2 deg
nominal pitch flap coupling, δ_3	-15 deg
torque link stiffness (azimuth windup)	11620 ft-lb/rad
gimbal spring	0
radius of pitch horn from pitch axis	0.0708 R
pitch horn radial station	0.0190 R
coll. pitch for horizontal pitch horn	16 deg
pitch link length	0.1439 R
blade stations	
hub/yoke bolts	0.0618 R
inboard centering bearing	0.0631 R
spinner outside radius (at blades)	0.0929 R
inboard end of root fairing	0.1056 R
yoke/spindle bolts	0.1267 R
outboard centering bearing	0.1803 R
blade attachment bolts	0.2018 R
outboard end of root fairing	0.2684 R

Table 2. Blade Instrumentation.

measurement	radial station, r/R
flap and chord bending moment	.23, .365, .50, .67, .85
torsion moment	.432, .585, .76, .90
pressure, blade #1	.50, .62, .82, .96
pressure, blade #2	.33, .72, .90, .98

Table 5. Sign conventions (helicopter mode).

measurement	positive value
propulsive force, X	forward
flap bending moment	blade tip bent upward
lag bending moment	blade tip bent toward trailing edge
torsion moment	blade twisted tip leading edge up
pitch link force	link in tension

Table 3. Source of TRAM blade properties for analytical model.

quantity	source
flap and lag hinge spring	match measured nonrotating frequency and stiffness
control system and pitch link stiffness	match measured nonrotating frequency
blade section mass and moment of inertia	measured
blade chordwise center-of-gravity offset	measured
blade bending and torsion stiffness	measured
pitch case inertia and stiffness	calculated
blade chordwise neutral axis offset	calculated
blade structural principal axes pitch	calculated
blade chord and aerodynamic twist	CAD data
blade chordwise and normal quarter-chord offsets	CAD data
blade airfoil contours	CAD data
root fairing chord, twist, qc offsets, airfoil contours	measured

Table 4. TRAM blade frequencies; nonrotating, zero collective, cantilever modes.

	root stiffness			modal frequencies						
	ft-lb/rad	ft-lb/rad	lb/ft	Hz						
	flap hinge	lag hinge	pitch link	F	L	F	F	L	T	F
measured										
rap test				13.9	24.1	46.25	124.4	195	227.8	358
deflections (aluminum)	5590	38200	45600							
deflections (titanium)	5510	47700	30000							
calculated										
match rap test	5700	15800	69400	13.9	24.1	53.4	140	172	227.8	316
match deflections	5590	38200	45600	13.8	34.1	53.4	145	177	202	317
stiffness variation	10000	90000	137000	17.0	44.1	56.8	152	193	257	320
present model	5700	40000	69000	13.9	34.7	53.5	145	178	227.7	317

Table 6. Definition of aerodynamic and weight tare configurations.

quantity	blades	rotor	airspeed	shaft angle
data	on	rotating	vary	vary
weight tare	on	nonrotating	0	match data
aero tare	off	rotating	match data	match data
aero weight tare	off	rotating	0	match data

Table 7. Measured operating condition of helicopter mode points selected for detailed examination.

V/WR = 0.15, $C_T/s = 0.089$

nominal shaft angle	-10	-6	-2	2	6	10
run	607	605	605	605	603	603
point	13	231	122	10	7	72
advance ratio, $V/\Omega R$.1509	.1506	.1509	.1502	.1495	.1506
rotor thrust, C_T/σ	.08814	.08792	.08831	.08895	.08839	.08949
shaft angle of attack	-9.99	-6.00	-2.03	1.99	5.94	9.95
corrected shaft angle of attack	-10.92	-6.94	-2.97	1.04	4.98	9.02
tip Mach number, M_{tip}	.6278	.6248	.6259	.6281	.6294	.6271
air density, ρ	.002334	.002326	.002336	.002354	.002373	.002356
air temperature (deg F)	59.69	64.37	62.62	59.20	57.98	61.55
azimuth correction, $\Delta\psi$	1.48	1.30	1.11	.94	.75	.53
rotor power, C_P/σ	.007386	.006516	.005567	.004656	.003683	.002603
rotor propulsive force, C_X/σ	.01382	.00809	.00191	-.00480	-.01091	-.01628
longitudinal gimbal tilt, β_{1c}	-.04	.07	.09	.03	-.14	-.30
lateral gimbal tilt, β_{1s}	-.08	-.09	.16	.10	-.13	-.33
missing c_n	.96R				.82 R	.82 R
missing flap moment	.365 R	.365 R	.365 R	.365 R	.365 R	.365 R
missing torsion moment	.76 R	.76 R				

V/ΩR = 0.15, $C_T/\sigma = 0.128$

nominal shaft angle	-10	-6	-2	2	6	10
run	607	605	605	605	603	603
point	68	252	177	68	13	39
advance ratio, $V/\Omega R$.1506	.1503	.1500	.1512	.1504	.1501
rotor thrust, C_T/σ	.12679	.12619	.12371	.12665	.12662	.12625
shaft angle of attack	-9.98	-5.99	-2.10	1.93	5.95	10.03
corrected shaft angle of attack	-11.32	-7.34	-3.43	.59	4.60	8.69
tip Mach number, M_{tip}	.6264	.6247	.6254	.6266	.6290	.6280
air density, ρ	.002325	.002325	.002330	.002342	.002369	.002361
air temperature (deg F)	61.89	64.64	63.72	61.67	58.90	60.57
azimuth correction, $\Delta\psi$	2.47	2.25	1.92	1.69	1.37	1.02
rotor power, C_P/σ	.012392	.011290	.009617	.008402	.006704	.005002
rotor propulsive force, C_X/σ	.02137	.01239	.00455	-.00377	-.01364	-.02190
longitudinal gimbal tilt, β_{1c}	.06	.26	.09	.10	.22	.23
lateral gimbal tilt, β_{1s}	-.03	.01	.00	.09	.31	.26
missing c_n	.96R				.82 R	.82 R
missing flap moment	.365 R	.365 R	.365 R	.365 R	.365 R	.365 R
missing torsion moment	.76 R	.76 R				



Figure 1. Tilt Rotor Aeroacoustic Model in the German-Dutch Wind Tunnel (TRAM DNW).

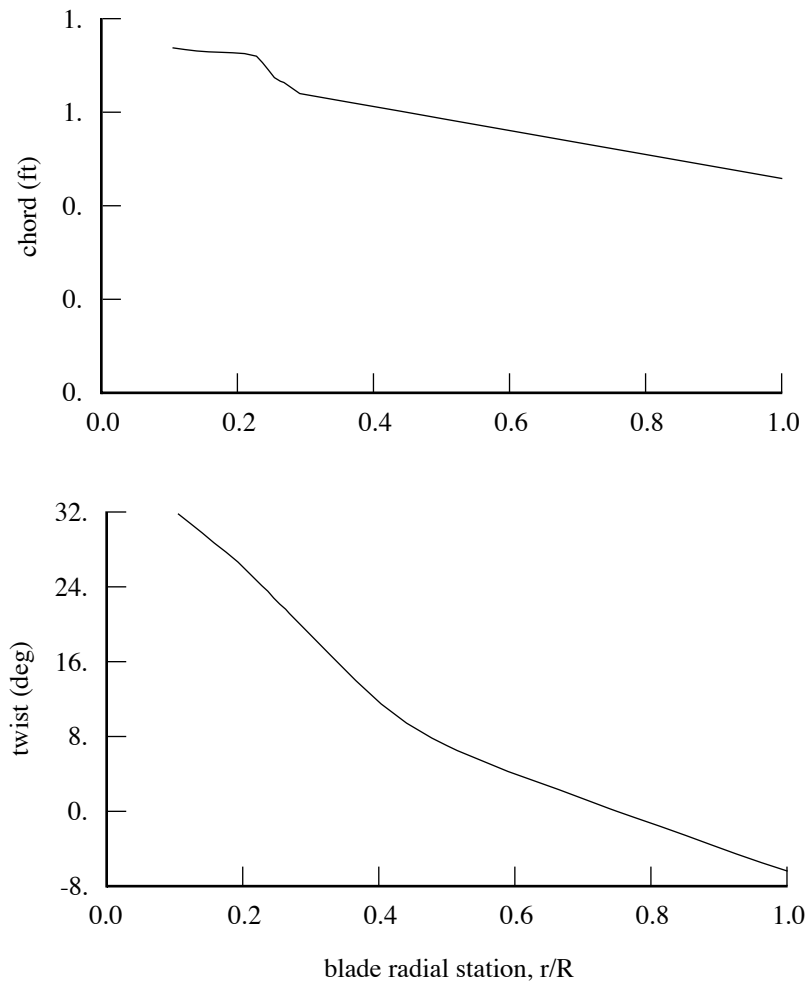


Figure 2. TRAM chord and twist distributions.

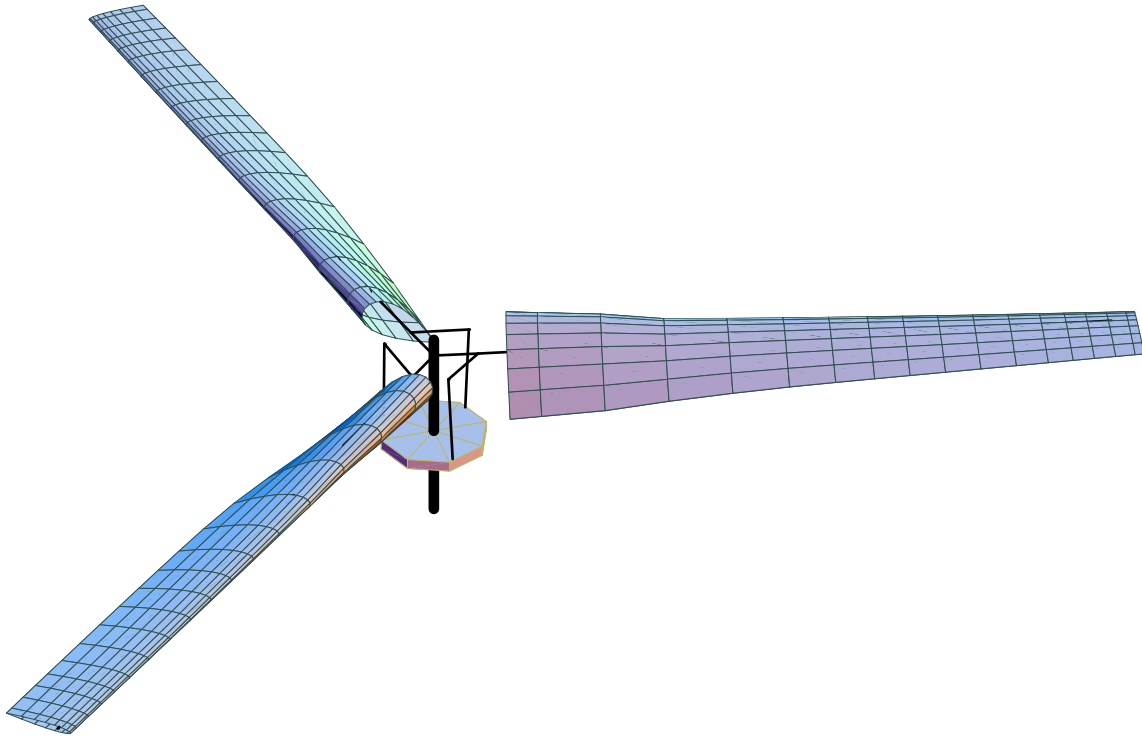


Figure 3. CAMRAD II model of TRAM.

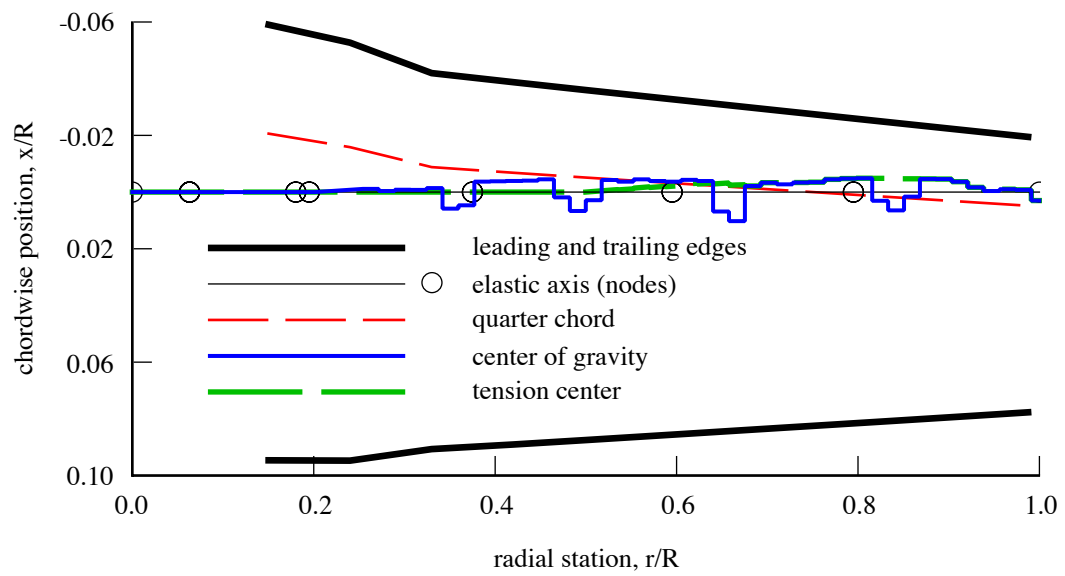


Figure 4. TRAM blade planform (shown untwisted).

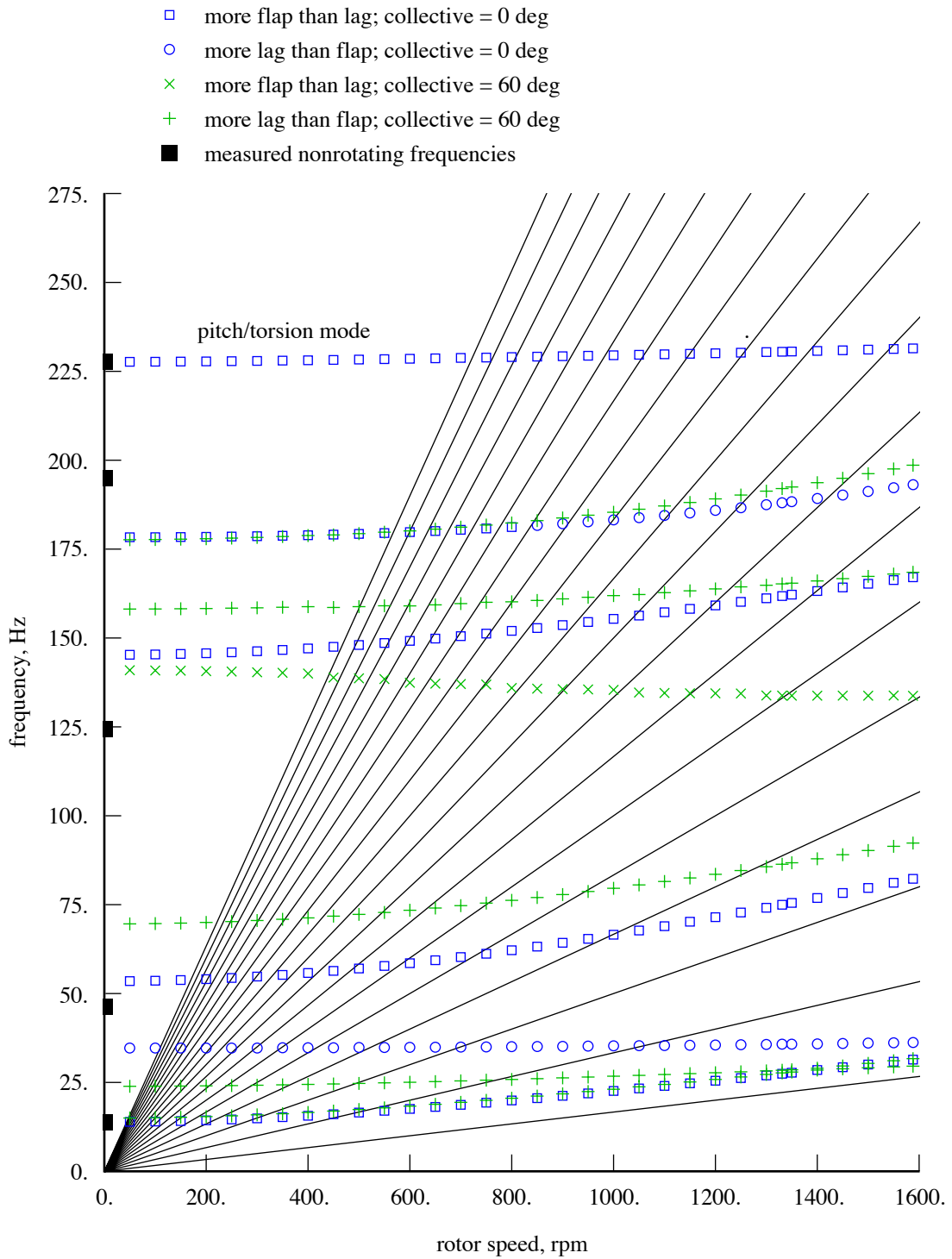


Figure 5a. Calculated natural frequencies of TRAM rotor blade; cantilever modes.

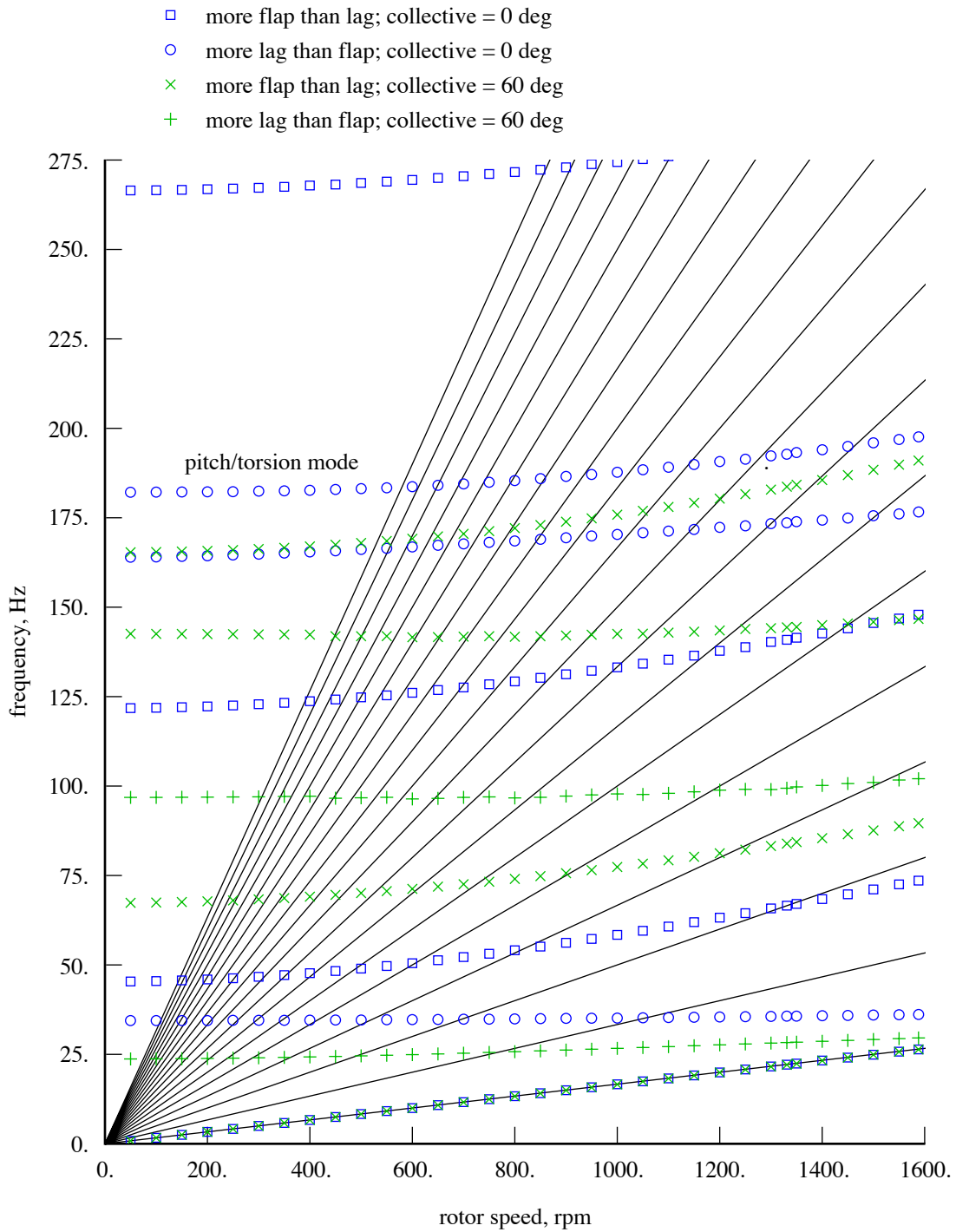


Figure 5b. Calculated natural frequencies of TRAM rotor blade; cyclic modes.

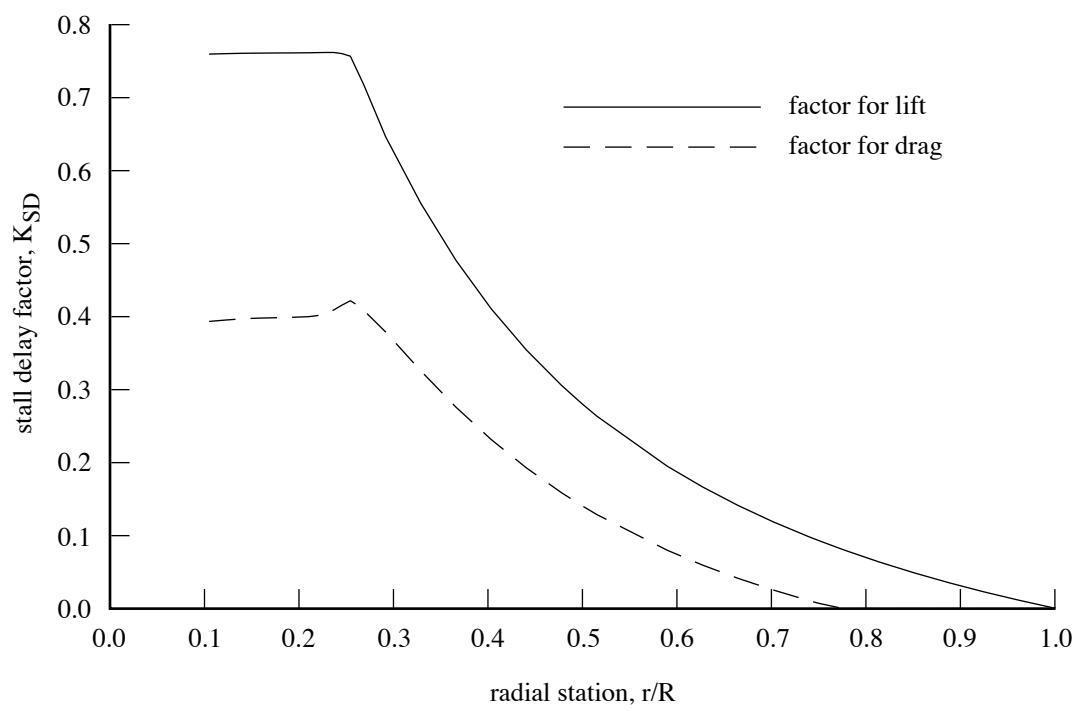


Figure 6. Stall delay factor for TRAM blade.

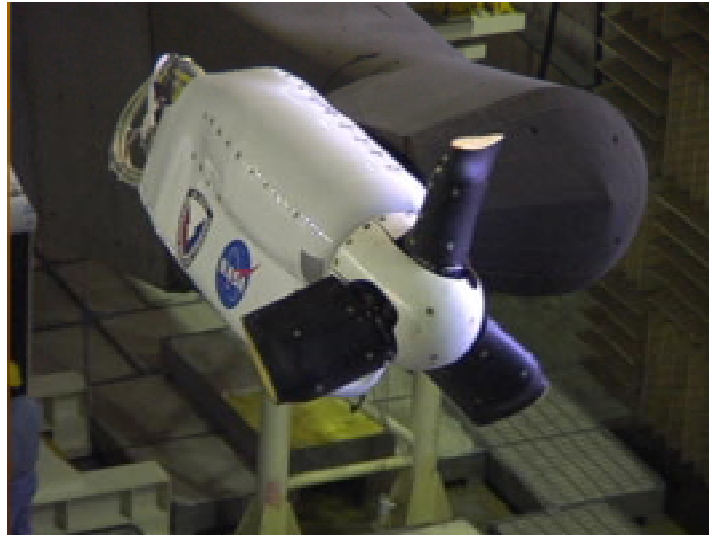


Figure 7. Helicopter mode aerodynamic tare configuration (shown in airplane mode).



Figure 8. Airplane mode aerodynamic tare configuration.

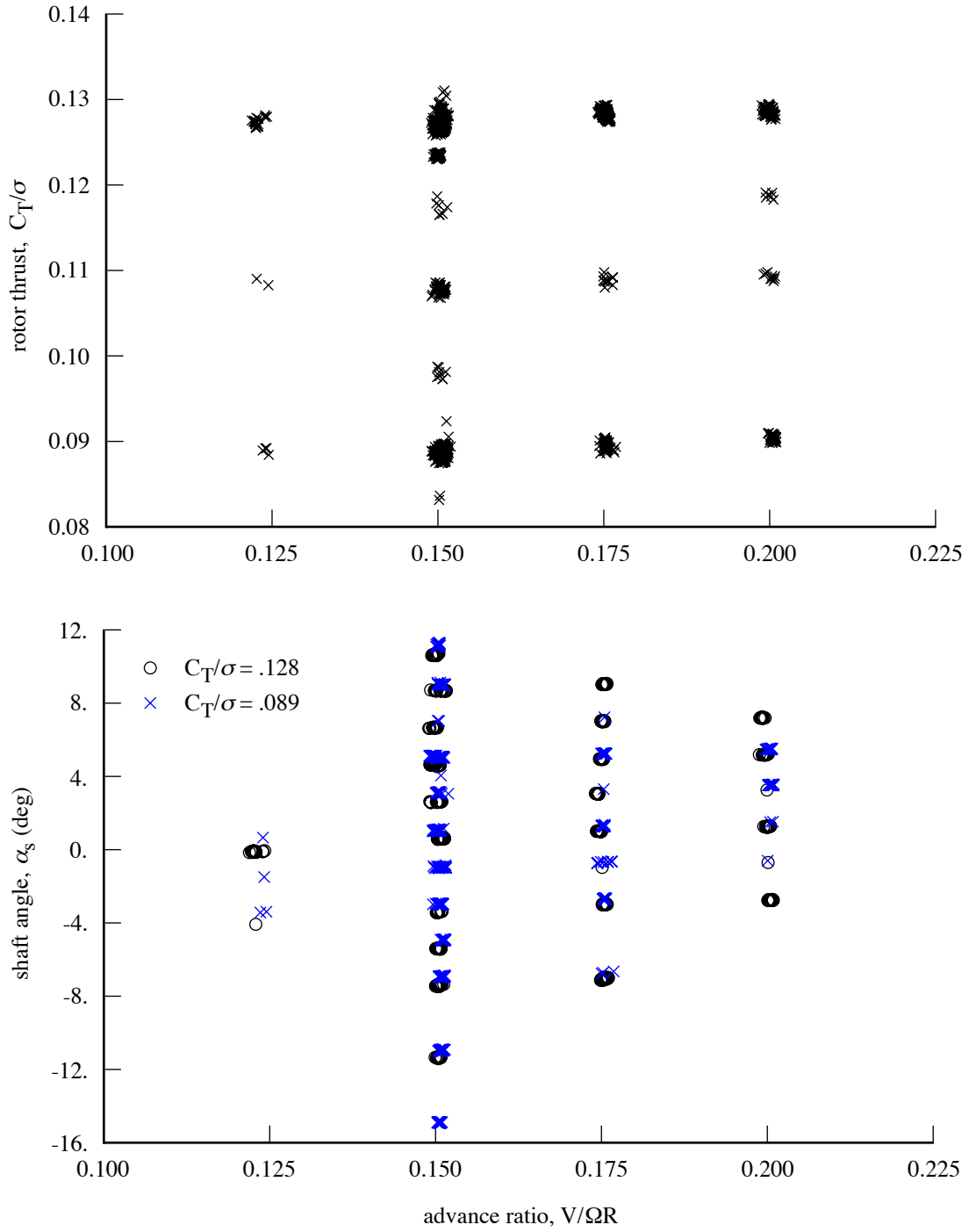


Figure 9. TRAM DNW operating conditions for helicopter mode tests.

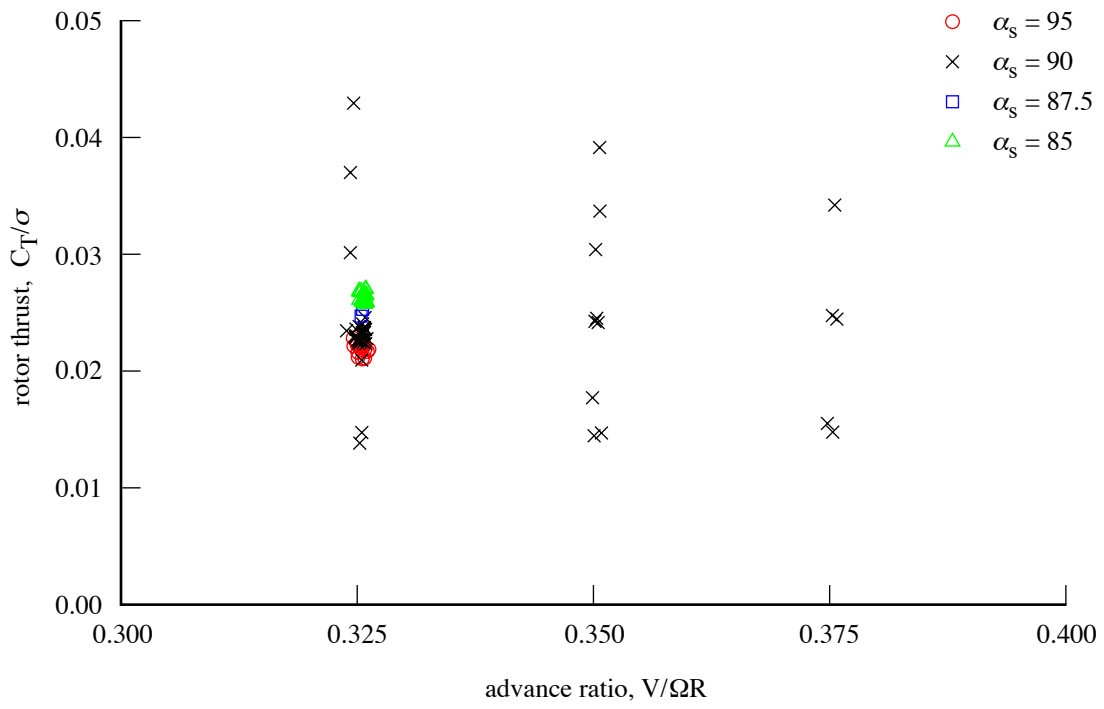


Figure 10. TRAM DNW operating conditions for airplane mode tests.

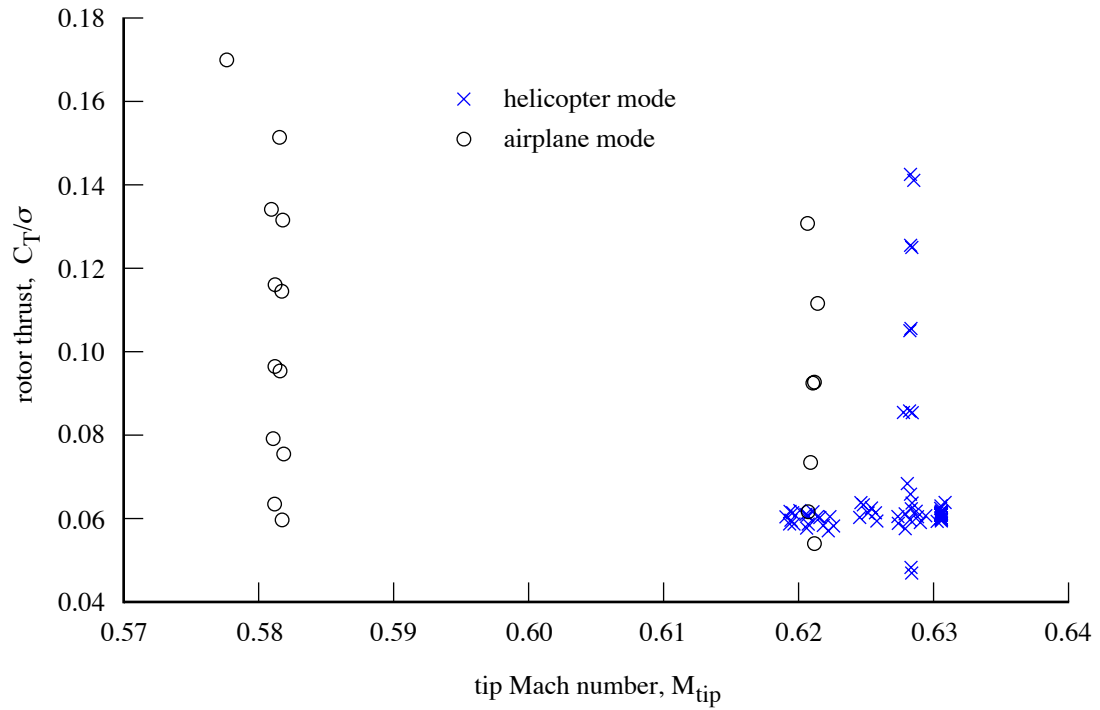


Figure 11. TRAM DNW operating conditions for hover tests.

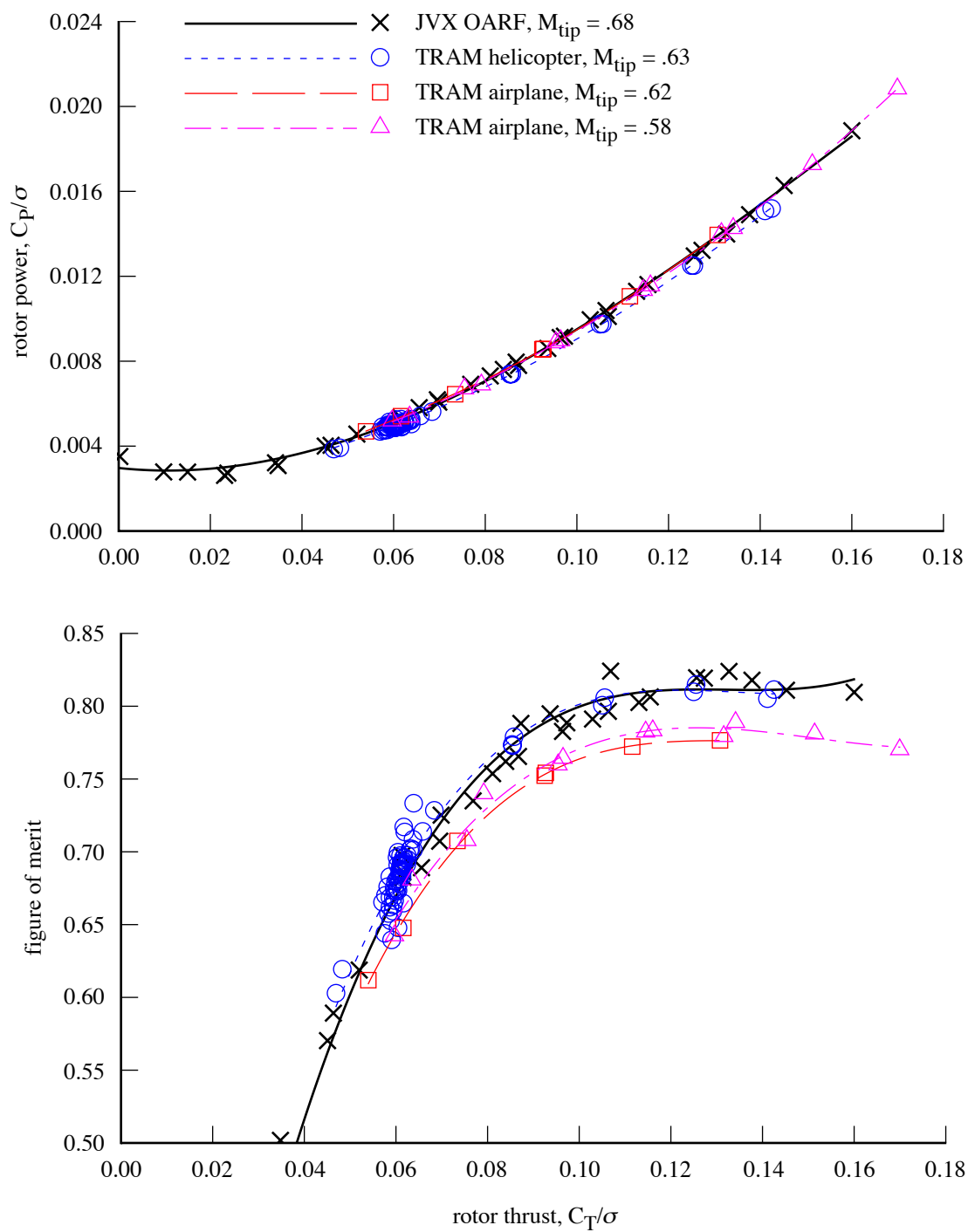


Figure 12. Measured JVX and TRAM hover performance.

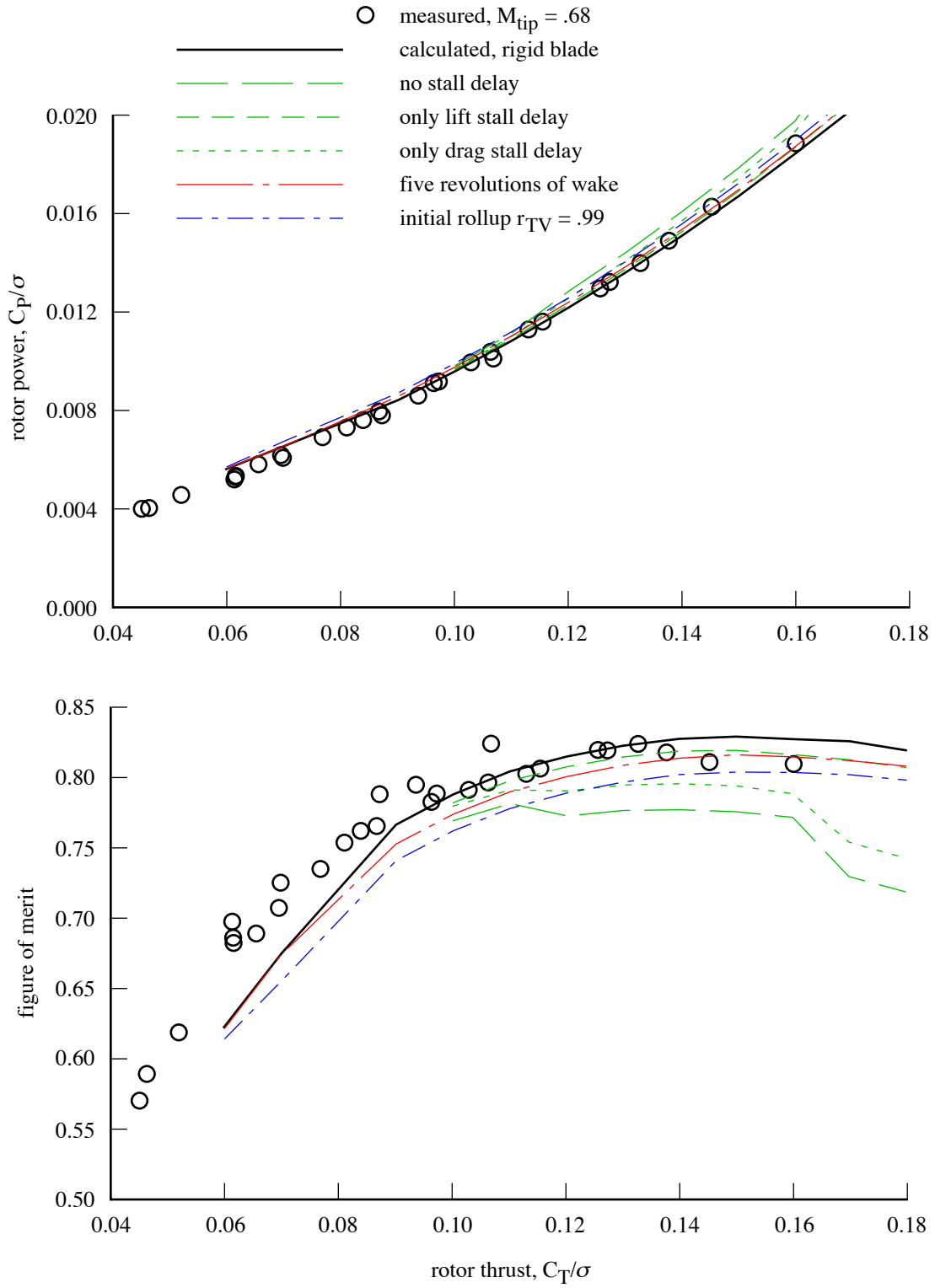


Figure 13. Influence of aerodynamic and wake parameters on calculated JVX hover performance.

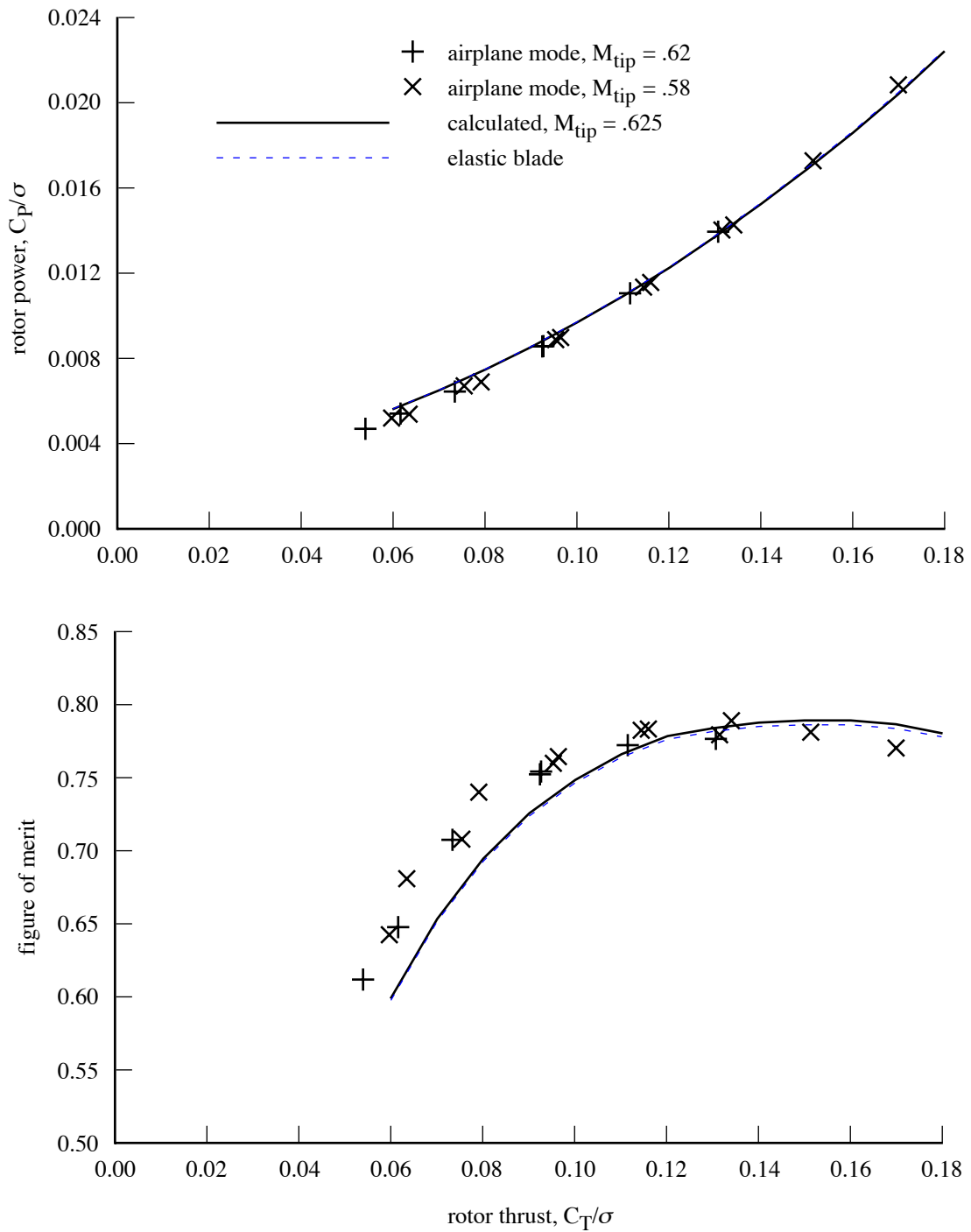


Figure 14. Measured and calculated TRAM hover performance.

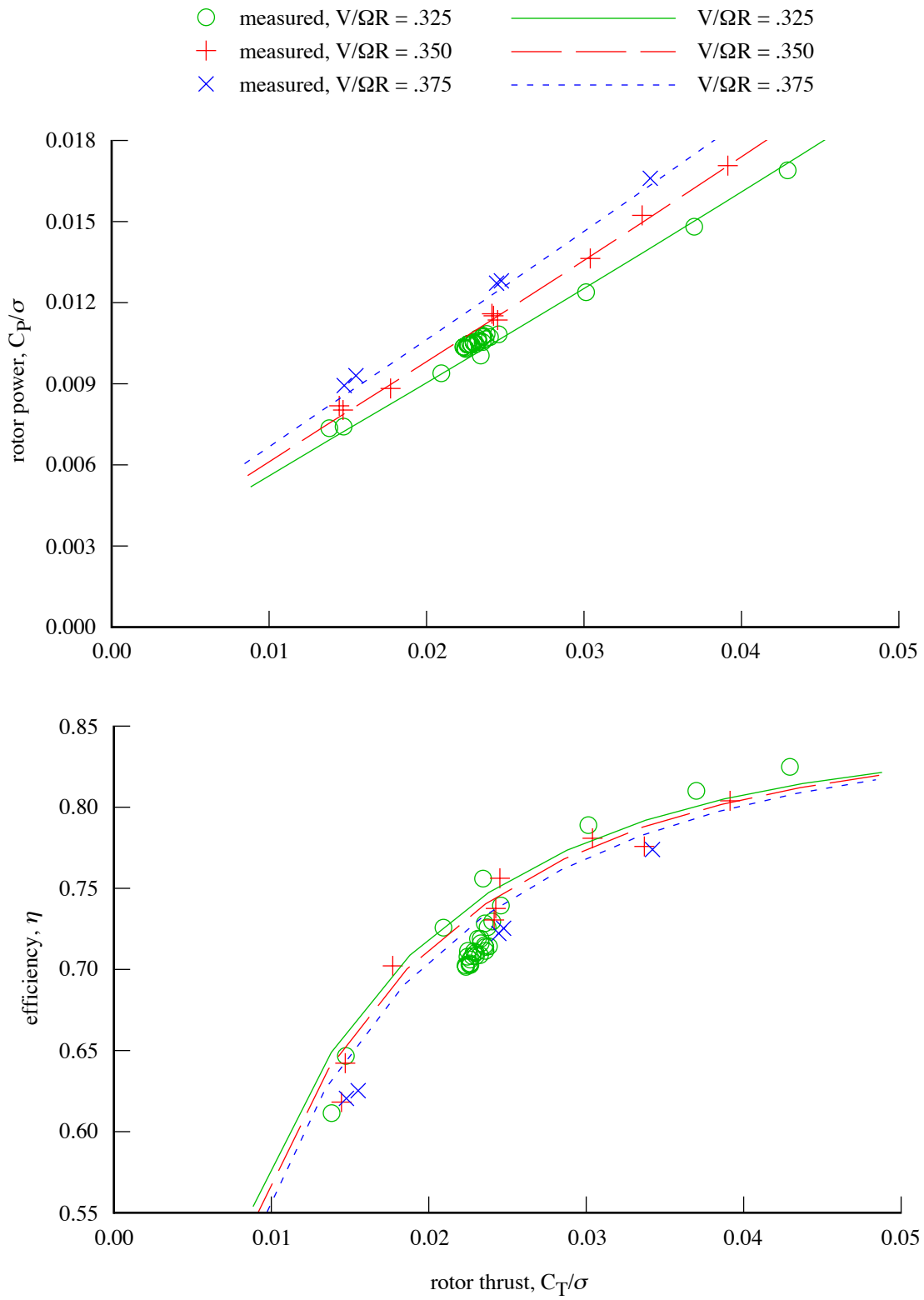


Figure 15. Measured and calculated TRAM airplane mode performance.

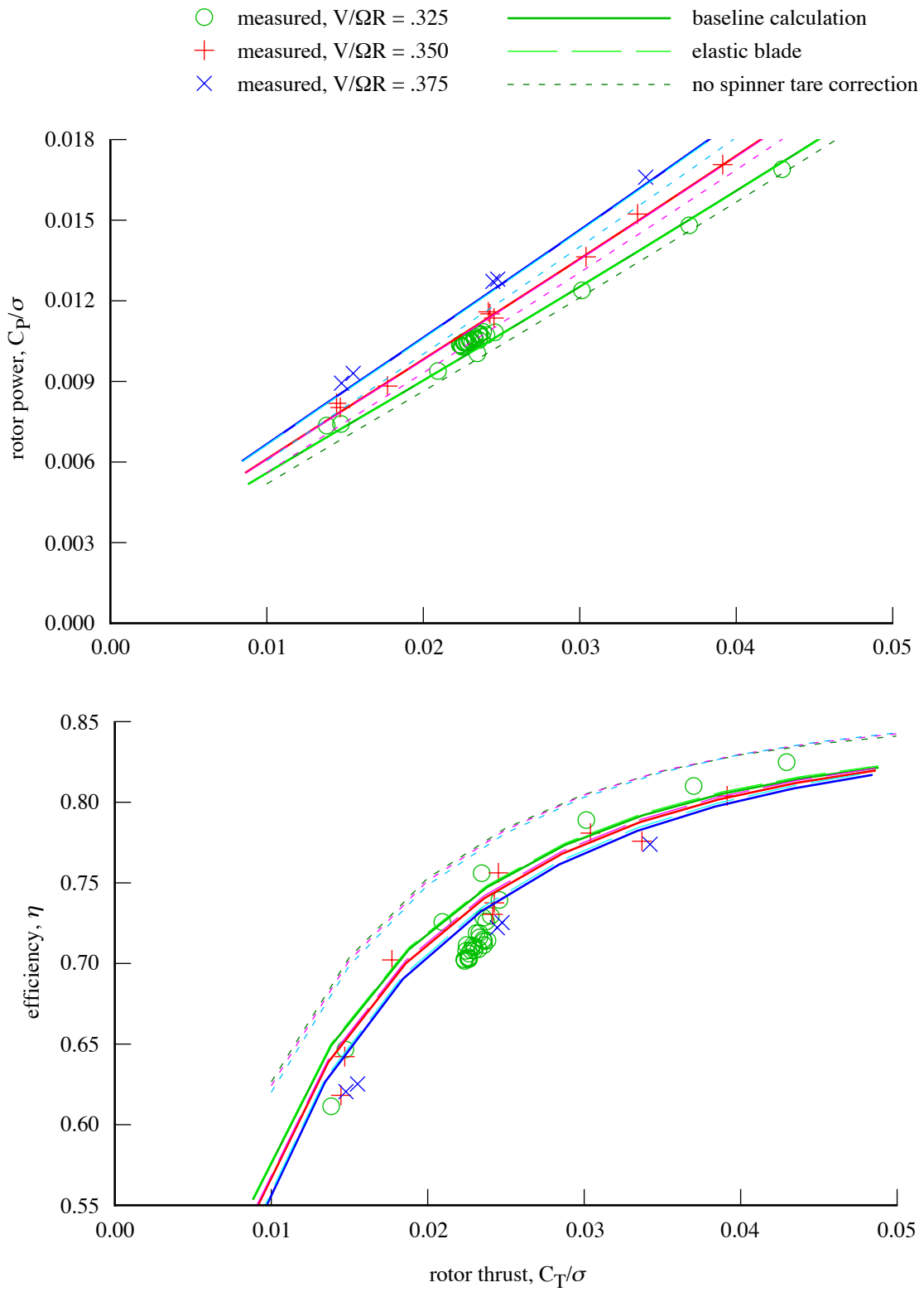


Figure 16. Influence of model on calculated TRAM airplane mode performance.

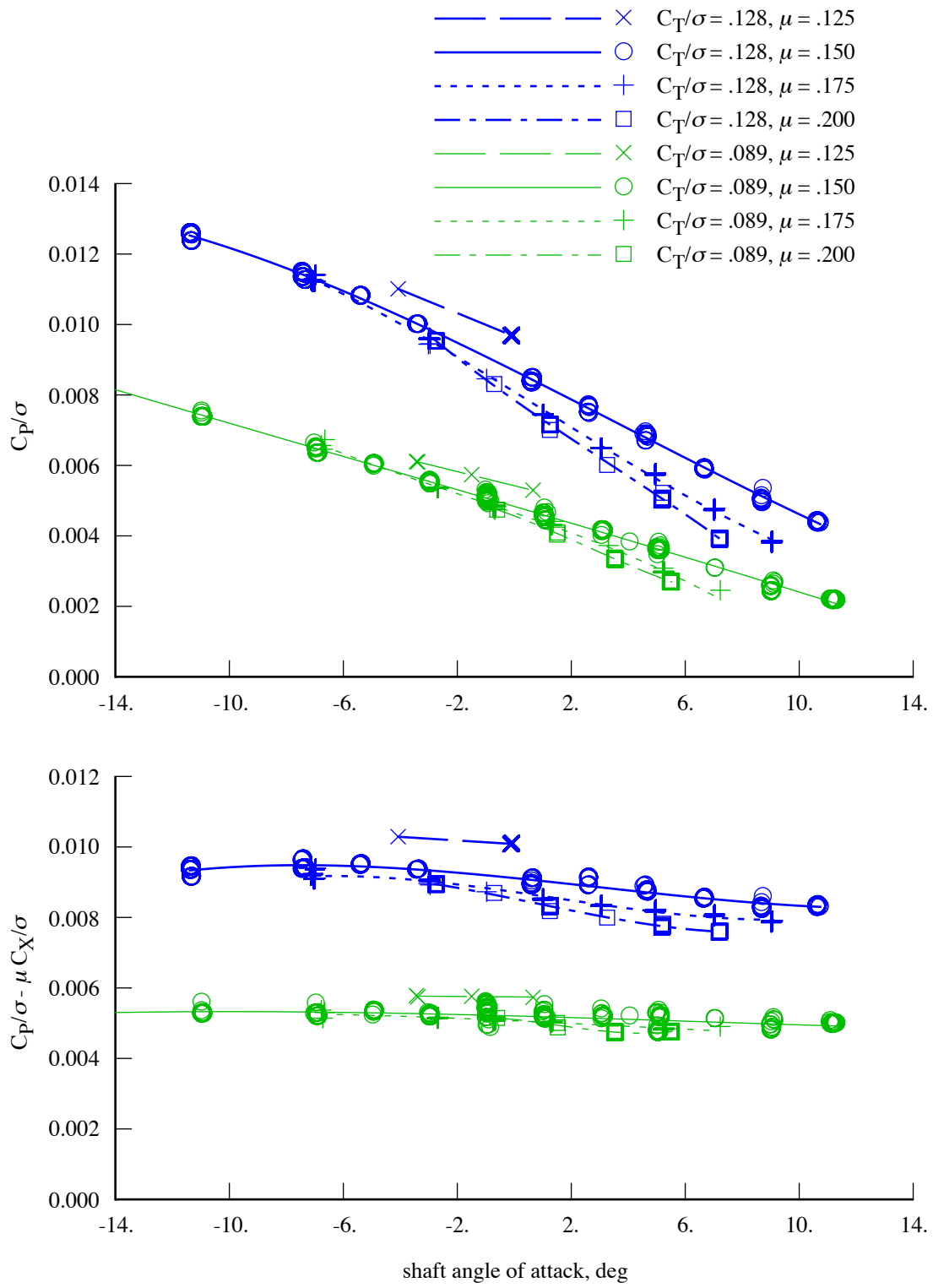


Figure 17. Measured TRAM helicopter mode performance.

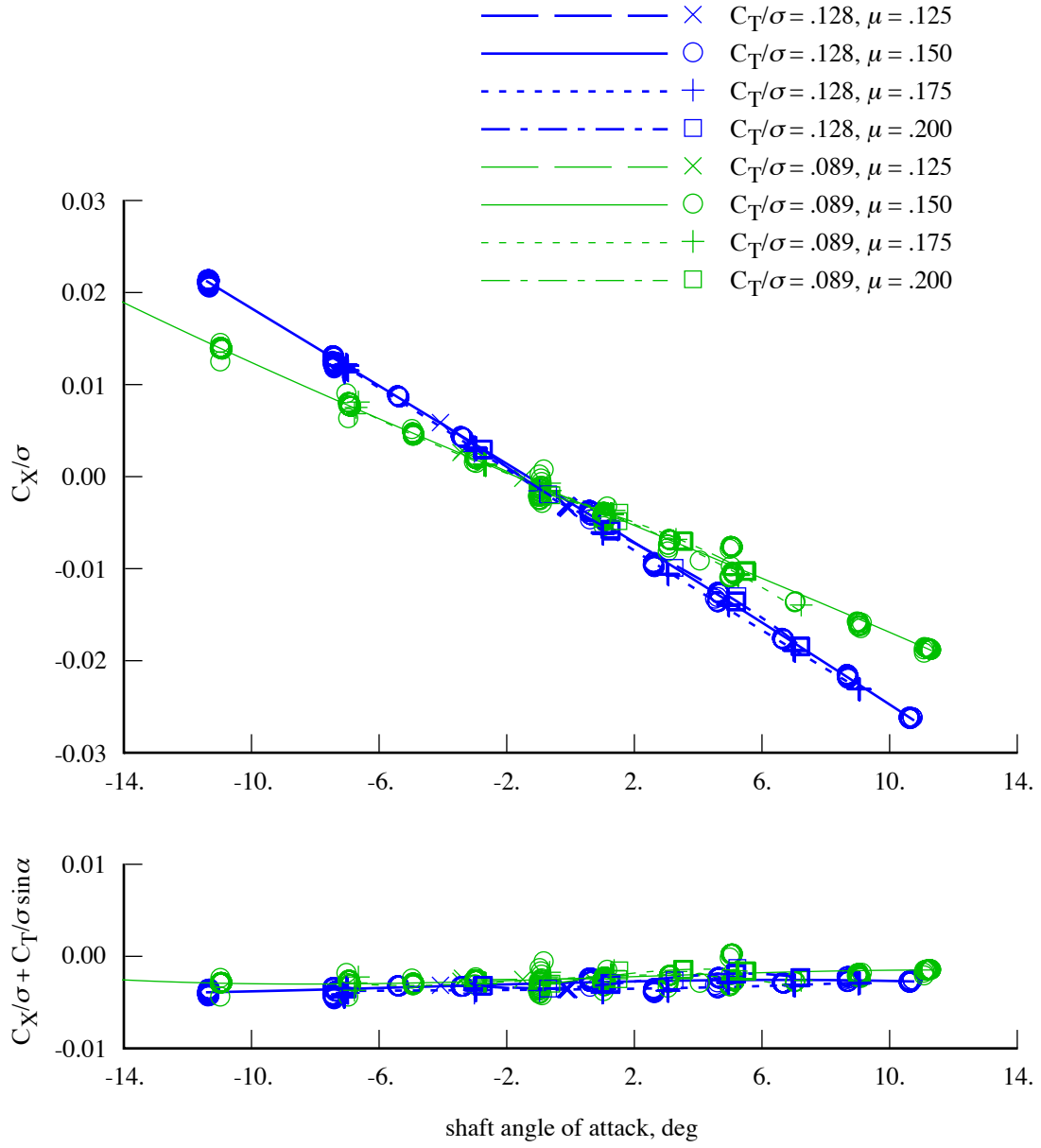


Figure 18. Measured TRAM helicopter mode performance.

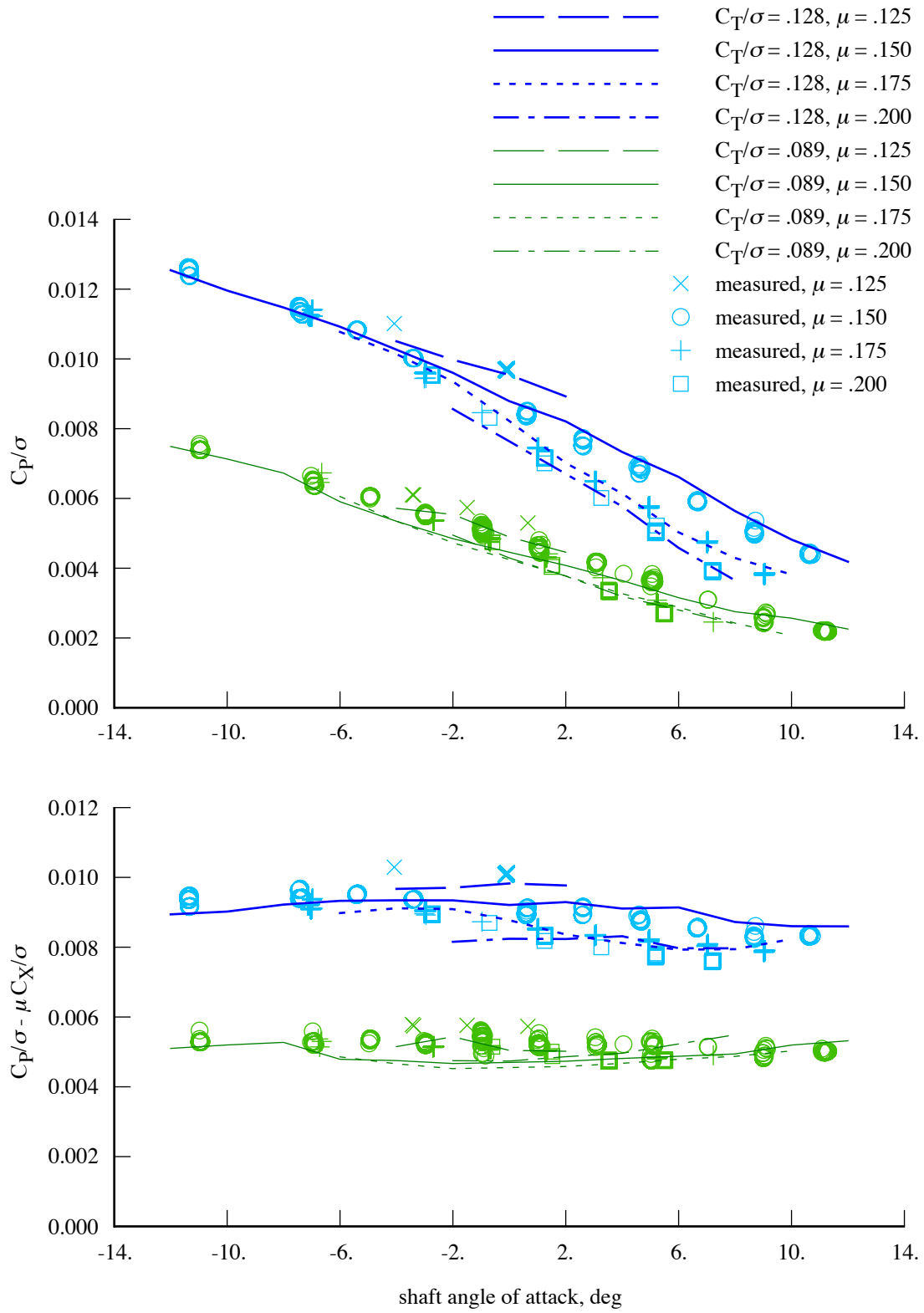


Figure 19. Measured and calculated TRAM helicopter mode performance (rigid blade model).

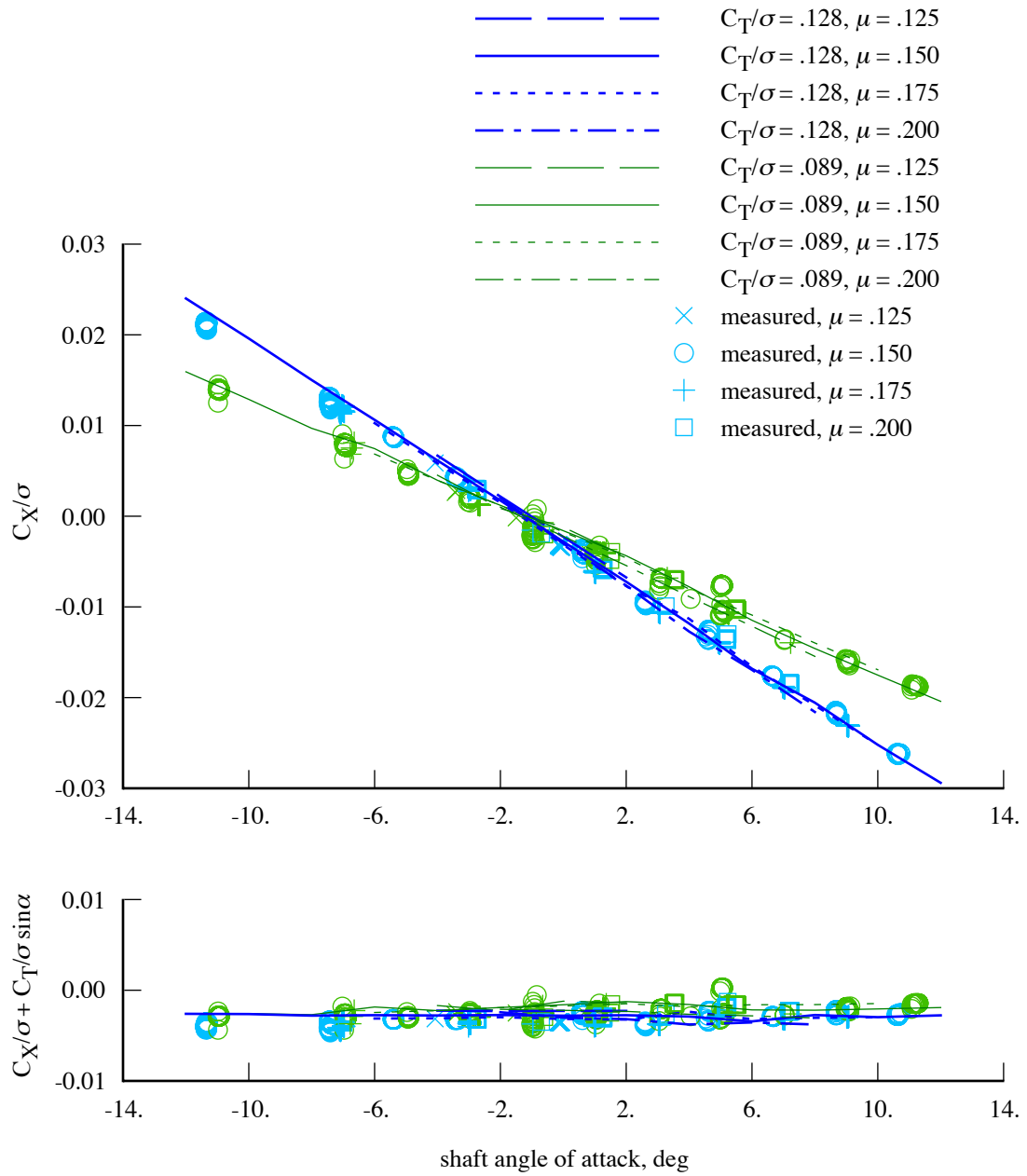


Figure 20. Measured and calculated TRAM helicopter mode performance (rigid blade model).

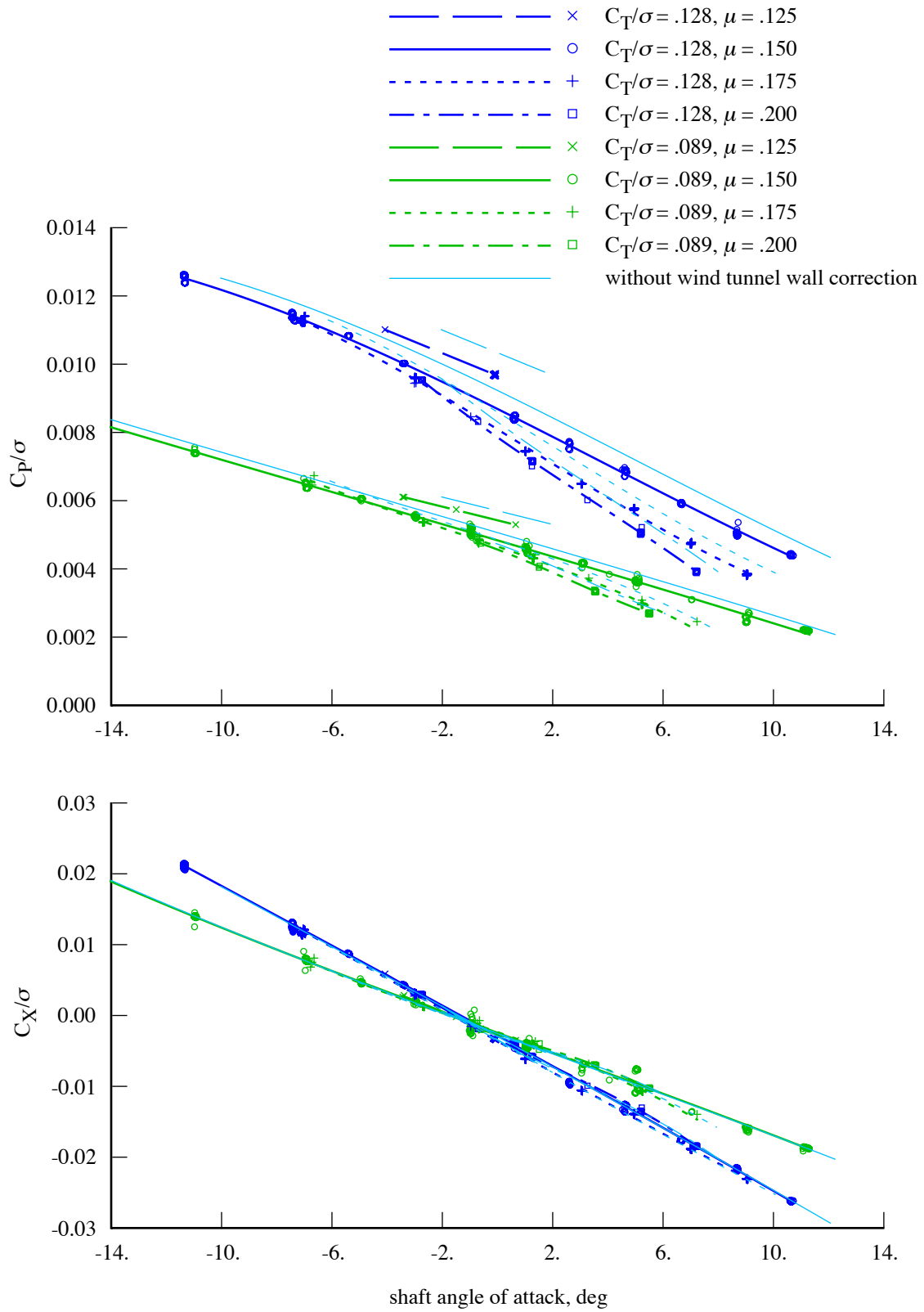


Figure 21. Measured TRAM helicopter mode performance, with and without wind tunnel wall correction.

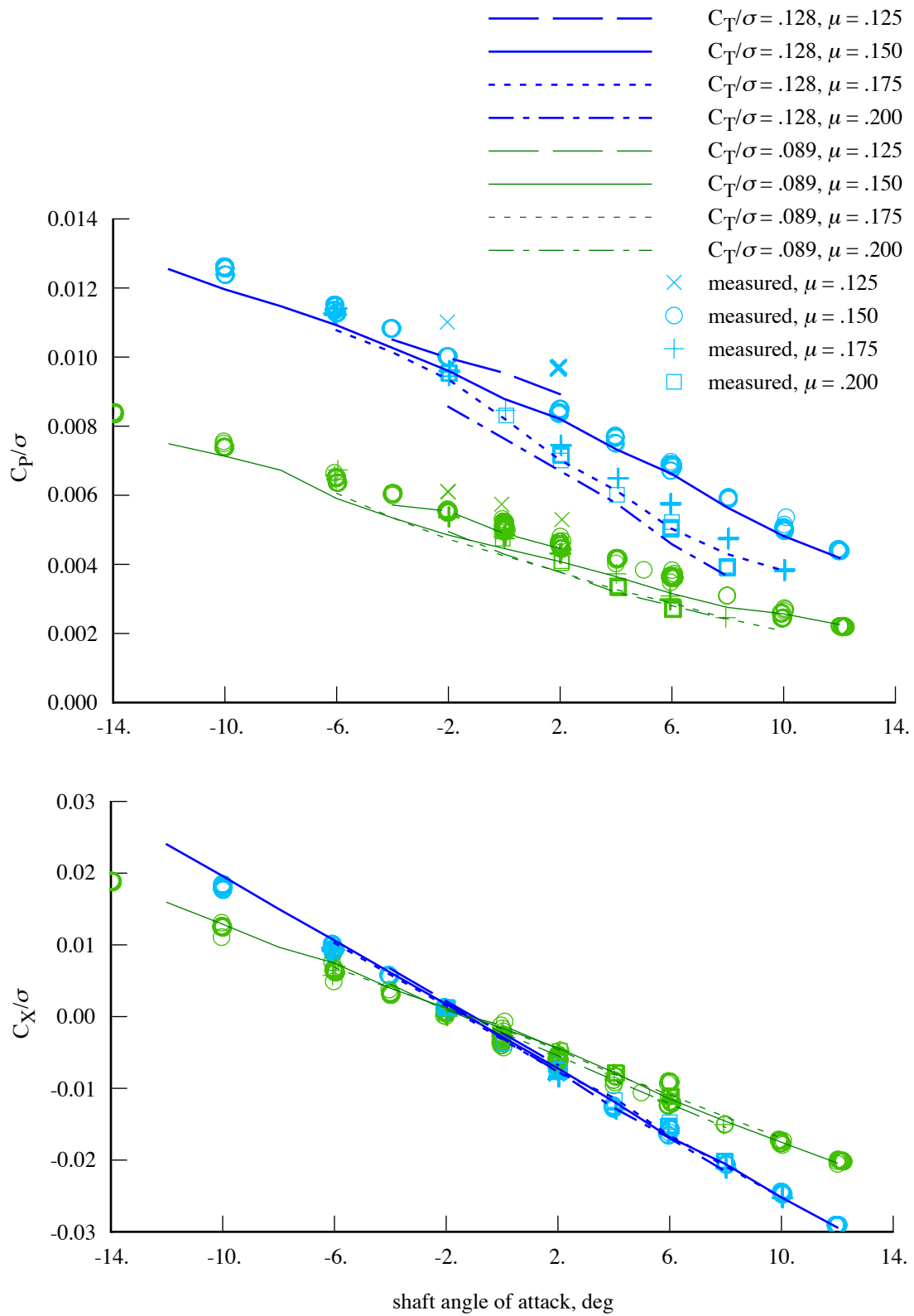


Figure 22. Measured and calculated TRAM helicopter mode performance; rigid blade model, without wind tunnel wall correction in measurements.

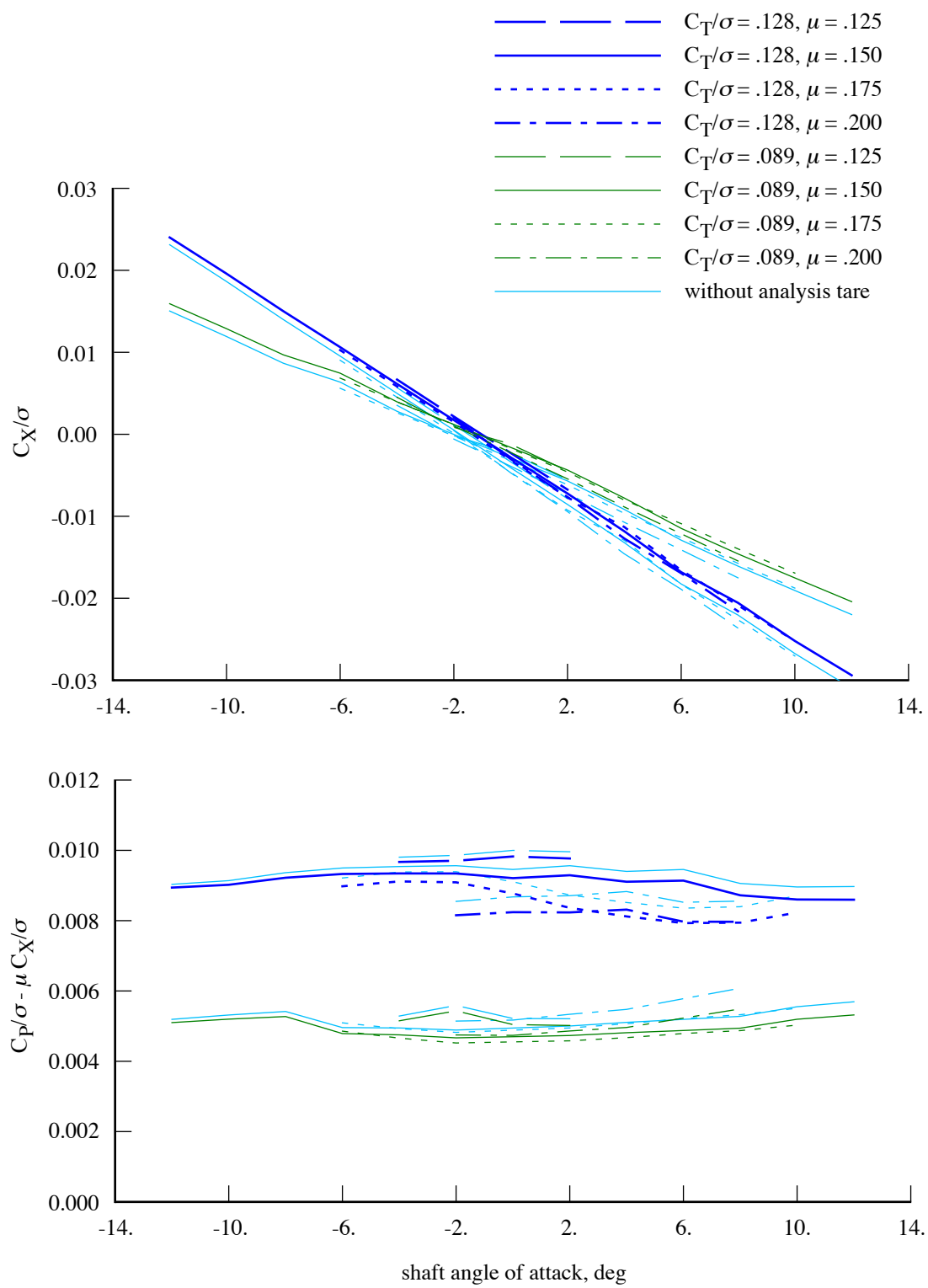


Figure 23. Calculated TRAM helicopter mode performance, with and without tare correction.

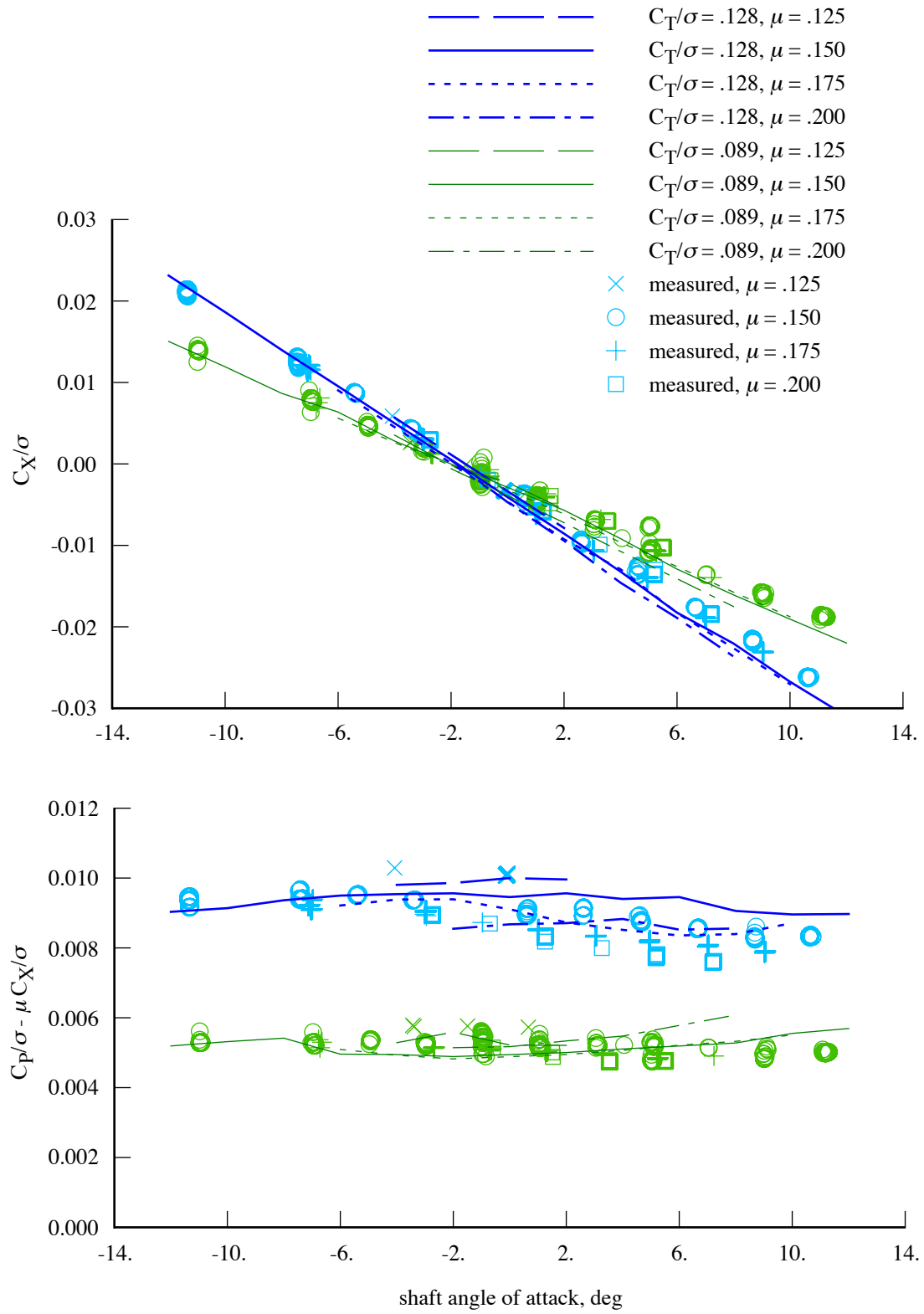


Figure 24. Measured and calculated TRAM helicopter mode performance;
rigid blade model, without tare correction in calculations.

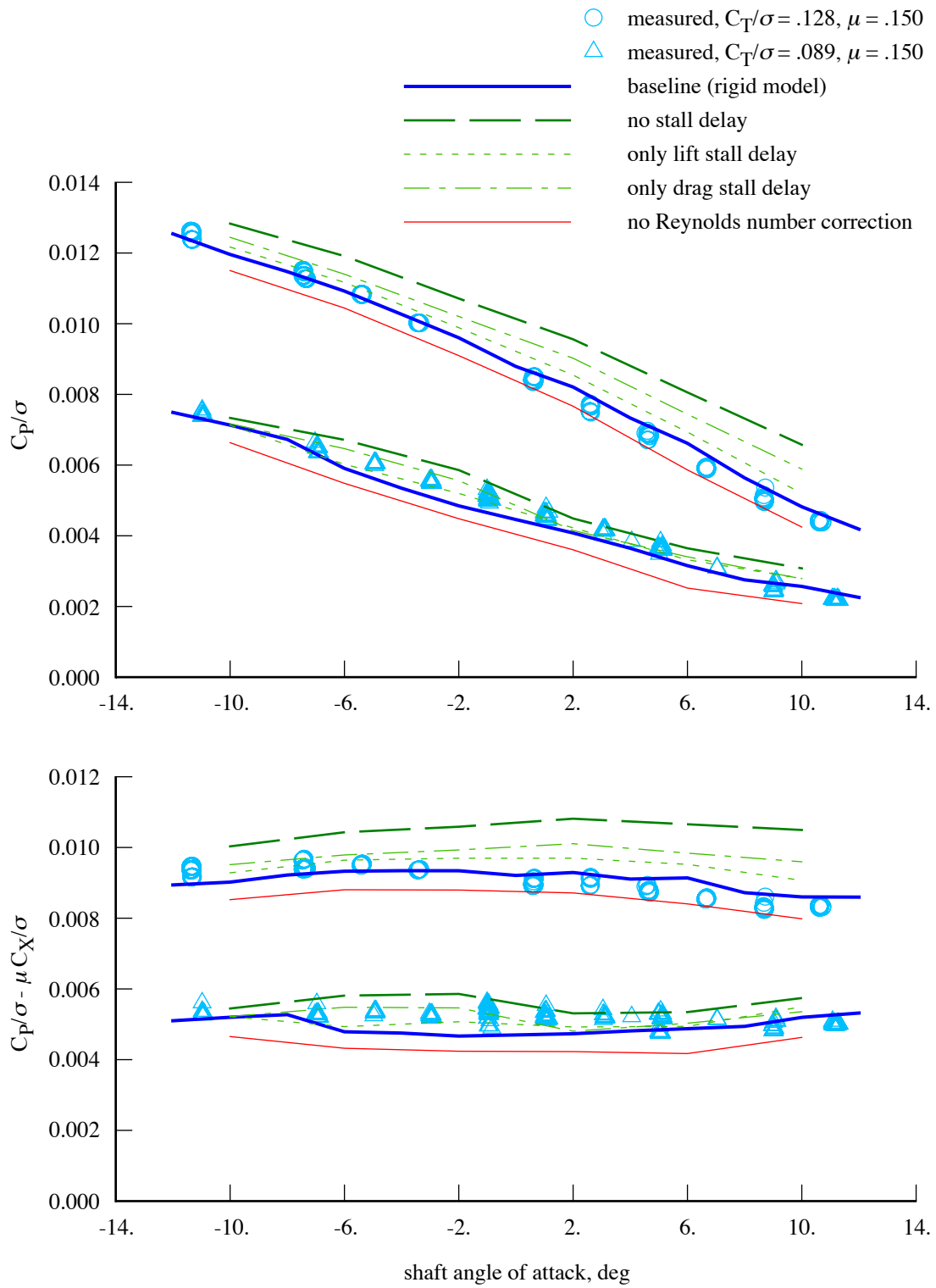


Figure 25. Influence of aerodynamic model on calculated TRAM helicopter mode performance ($\mu = 0.15$).

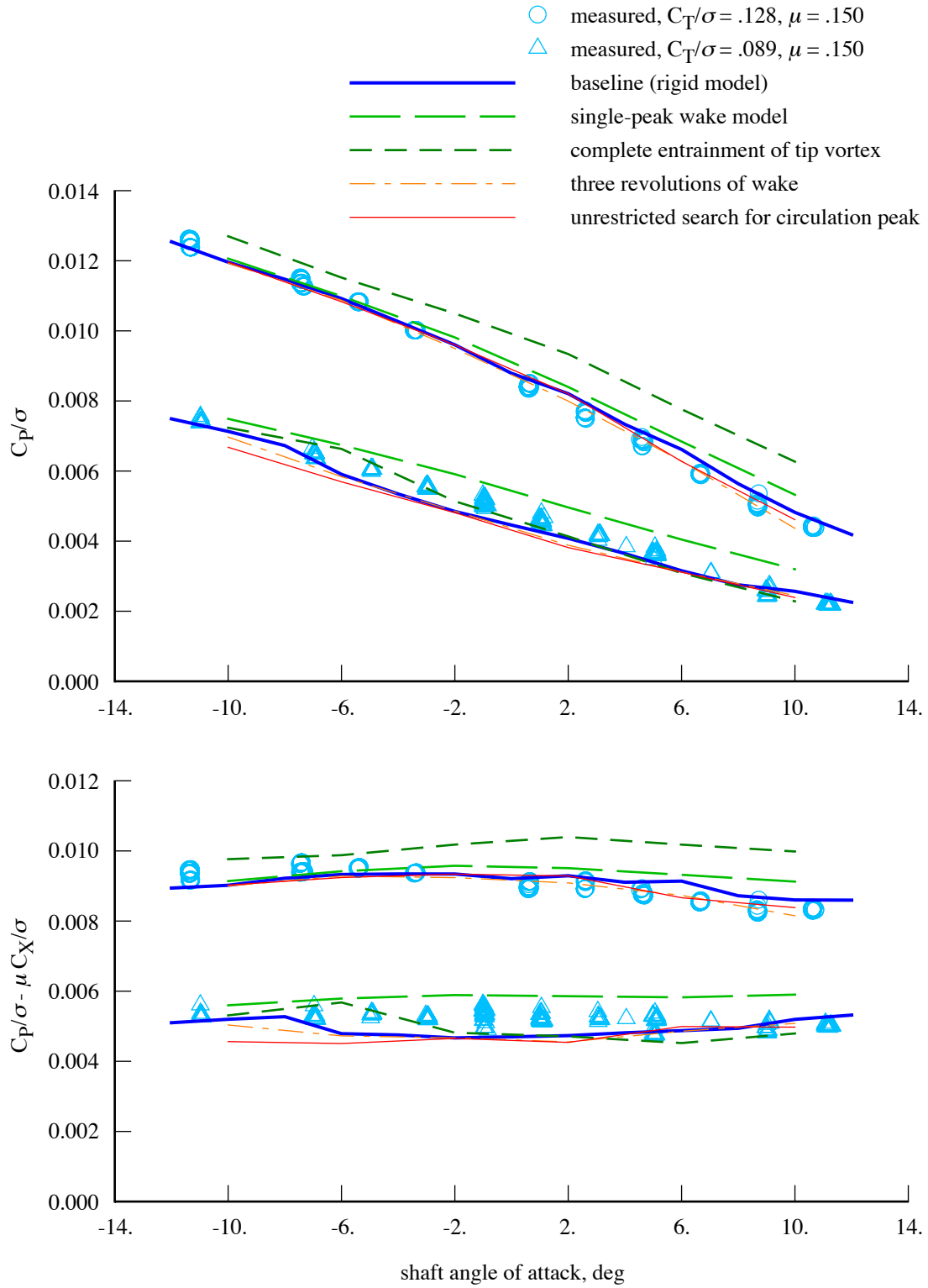


Figure 26. Influence of wake model on calculated TRAM helicopter mode performance ($\mu = 0.15$).

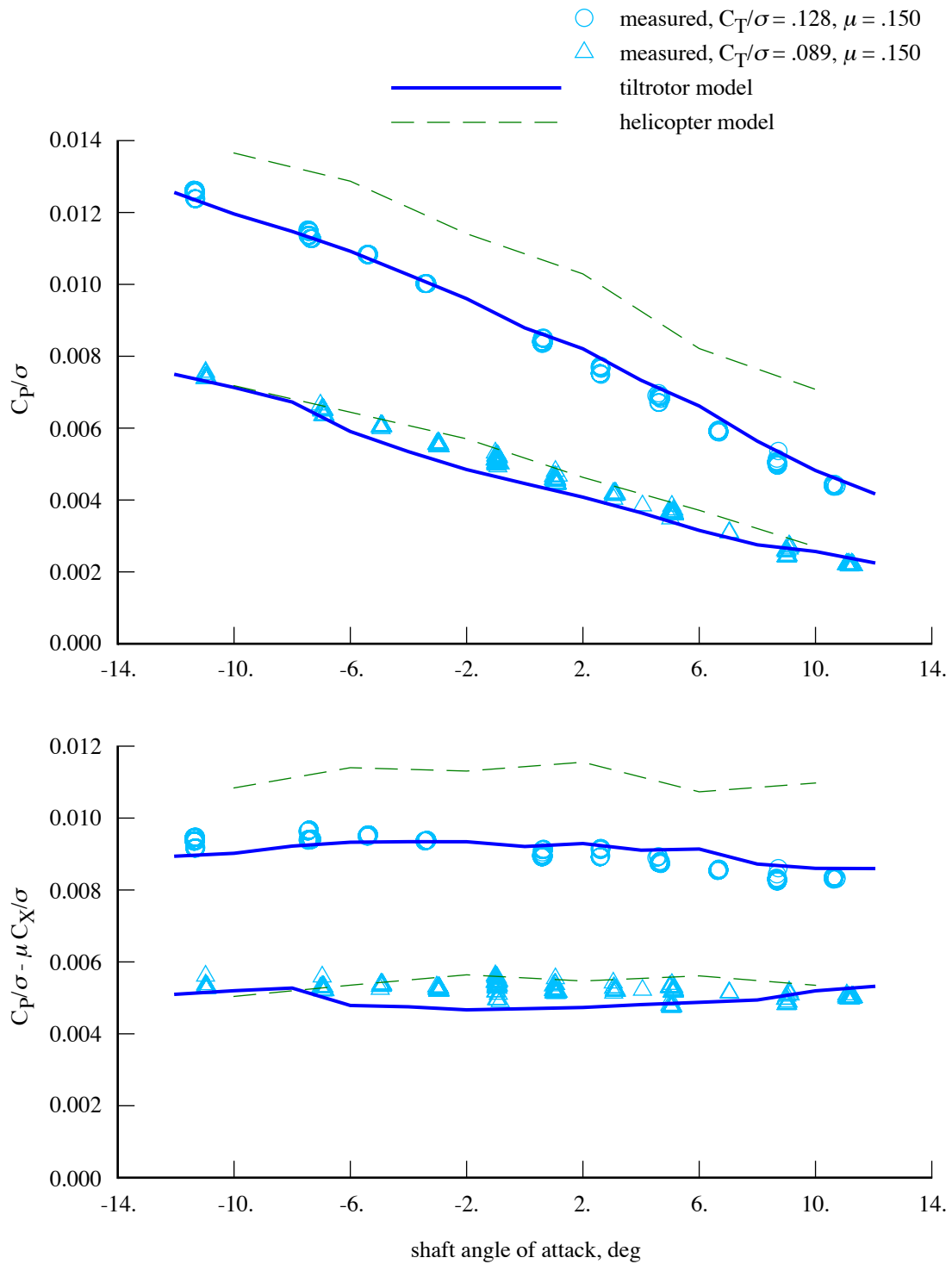


Figure 27. TRAM helicopter mode performance calculated using tiltrotor and helicopter aerodynamic and wake models (rigid blade model, $\mu = 0.15$).

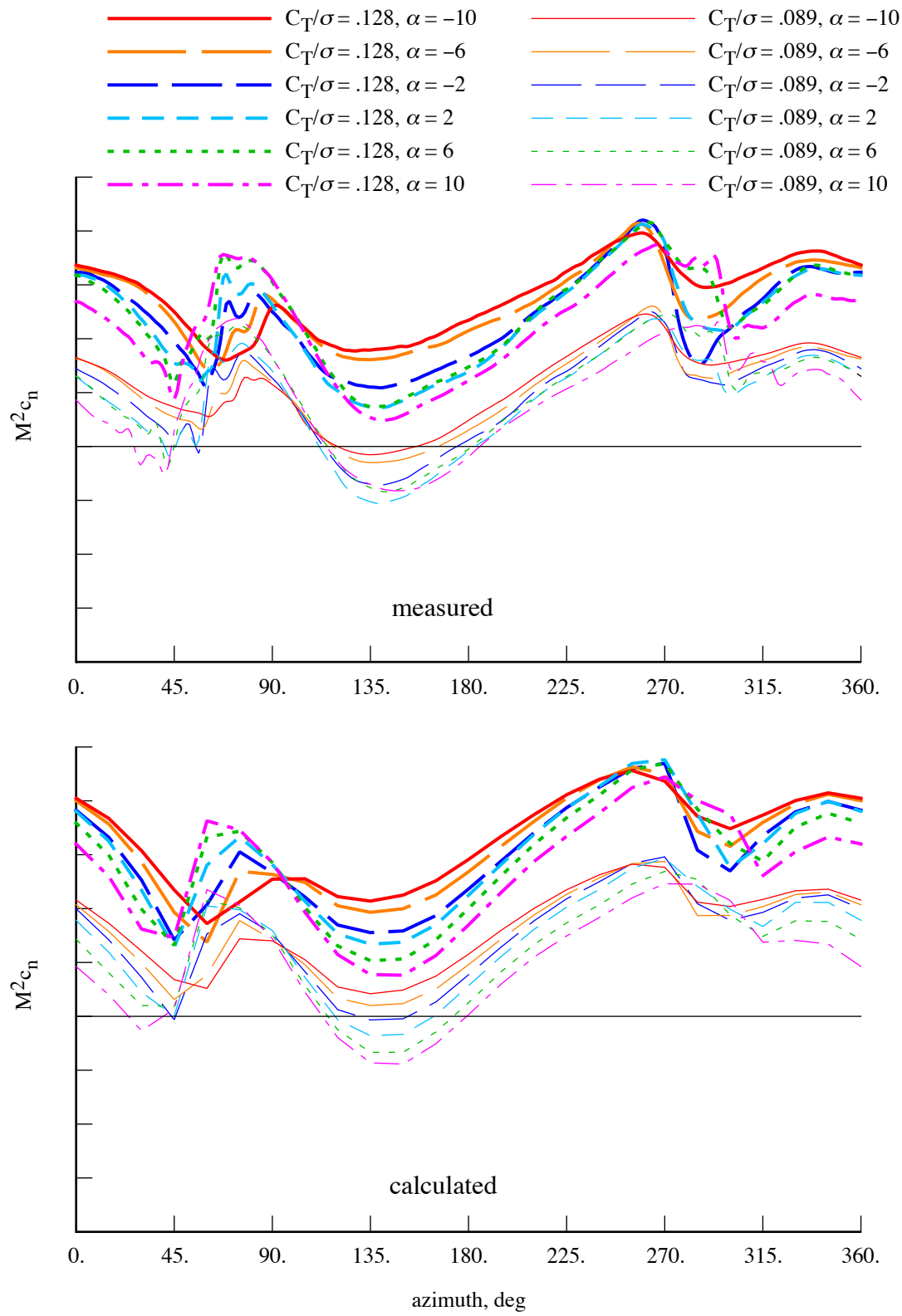


Figure 28a. Measured and calculated TRAM helicopter mode airloads ($\mu = 0.15$). Calculations using tiltrotor model with multiple-trailer wake model. Radial station $r = 0.90R$.

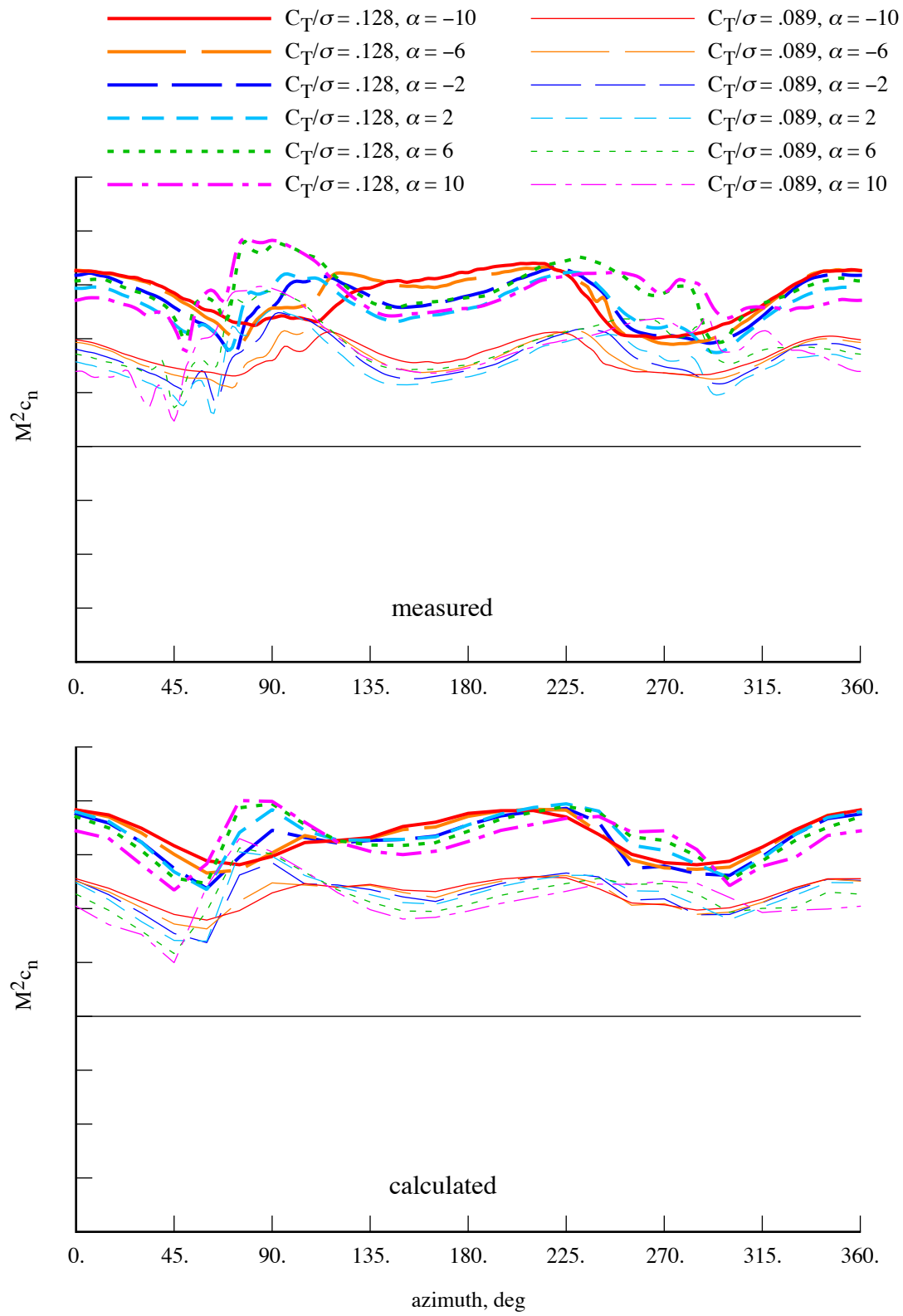


Figure 28b. Measured and calculated TRAM helicopter mode airloads ($\mu = 0.15$). Calculations using tiltrotor model with multiple-trailer wake model. Radial station $r = 0.72R$.

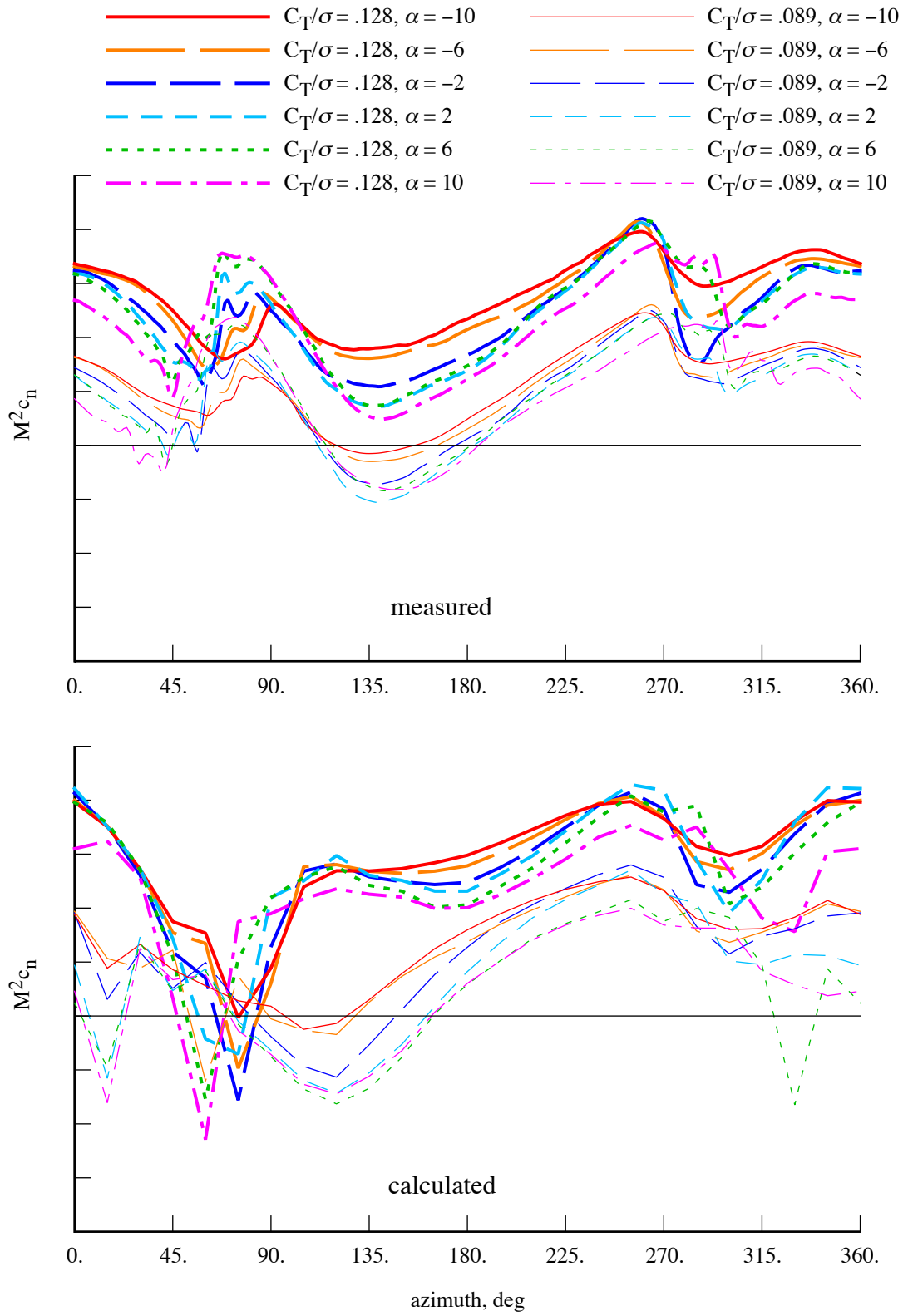


Figure 29a. Measured and calculated TRAM helicopter mode airloads ($\mu = 0.15$). Calculations using tiltrotor model with rolled-up wake model. Radial station $r = 0.90R$.

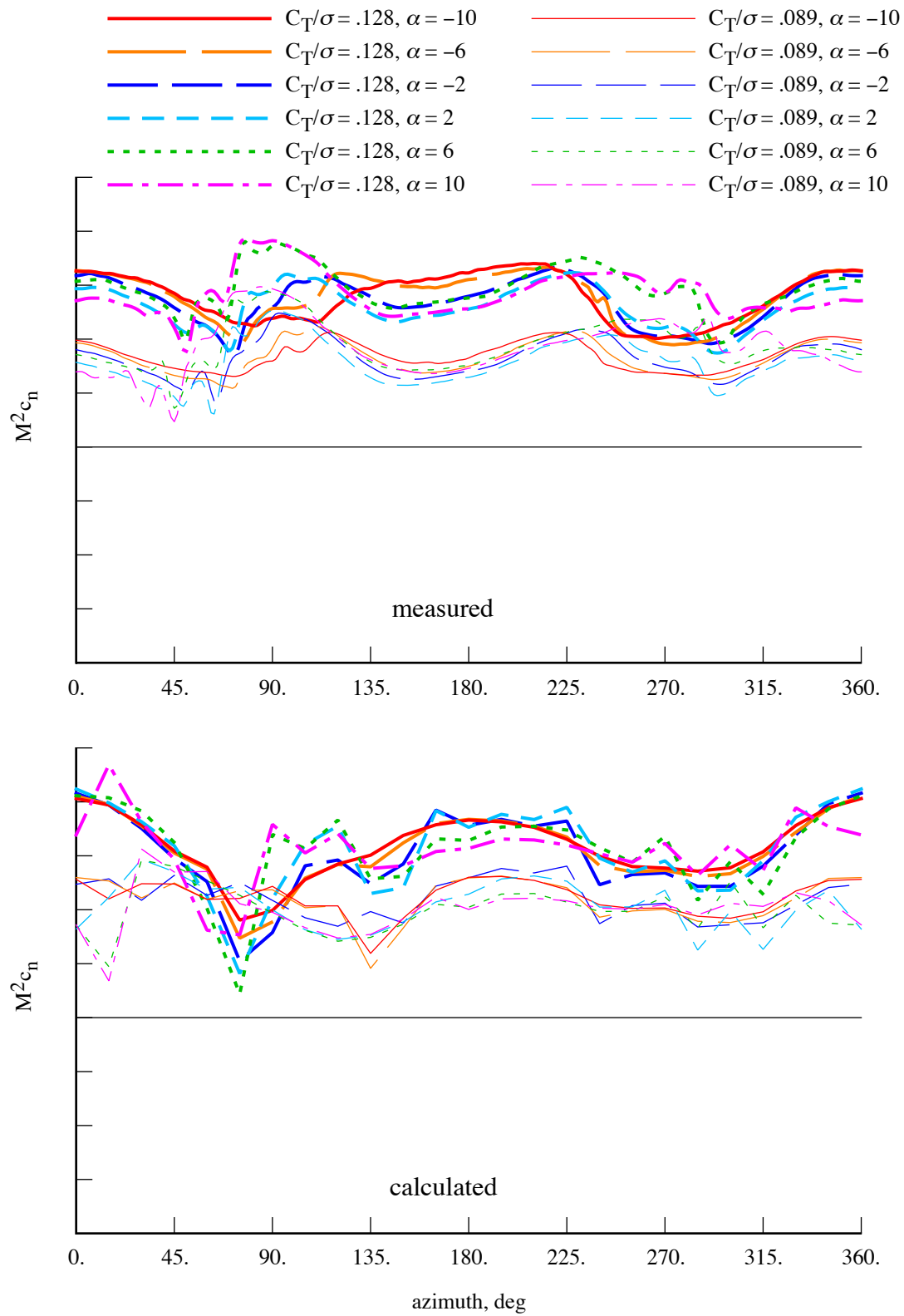


Figure 29b. Measured and calculated TRAM helicopter mode airloads ($\mu = 0.15$). Calculations using tiltrotor model with rolled-up wake model. Radial station $r = 0.72R$.

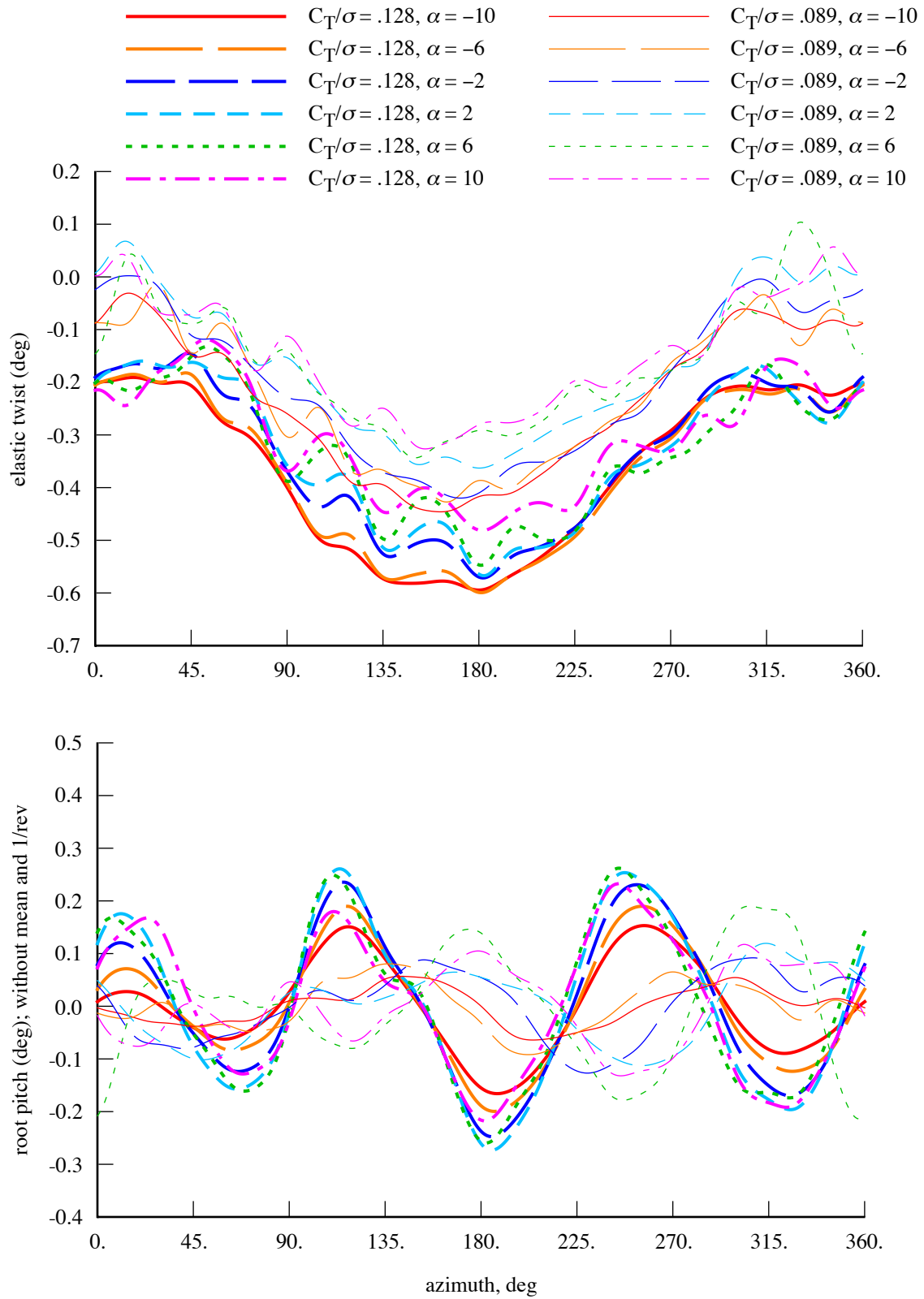


Figure 30. Calculated TRAM helicopter mode blade deflection ($\mu = 0.15$); elastic twist (tip pitch – root pitch) and root pitch (without mean and 1/rev).

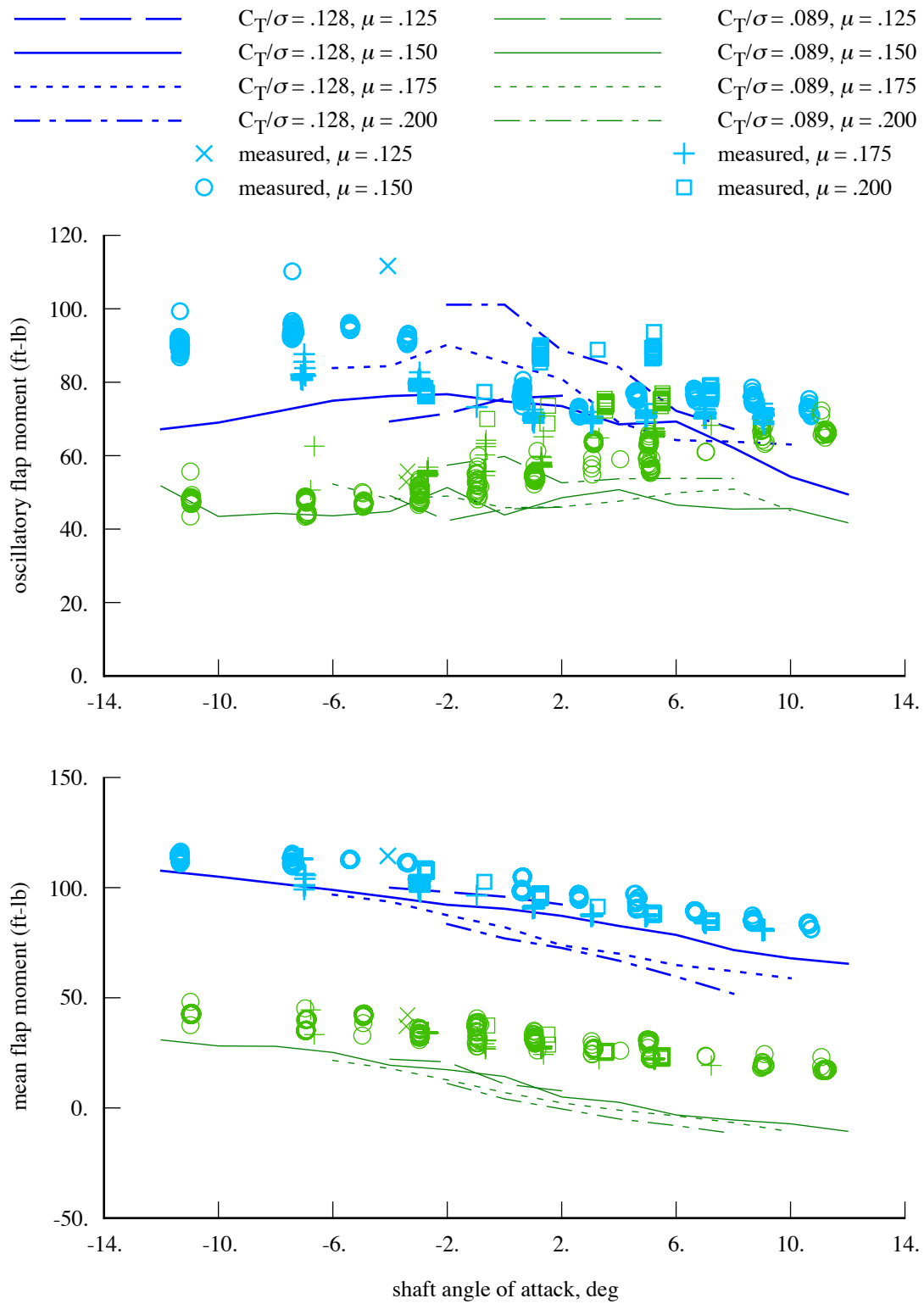


Figure 31. Measured and calculated TRAM helicopter mode blade loads; flap bending moment at $r = 0.23R$.

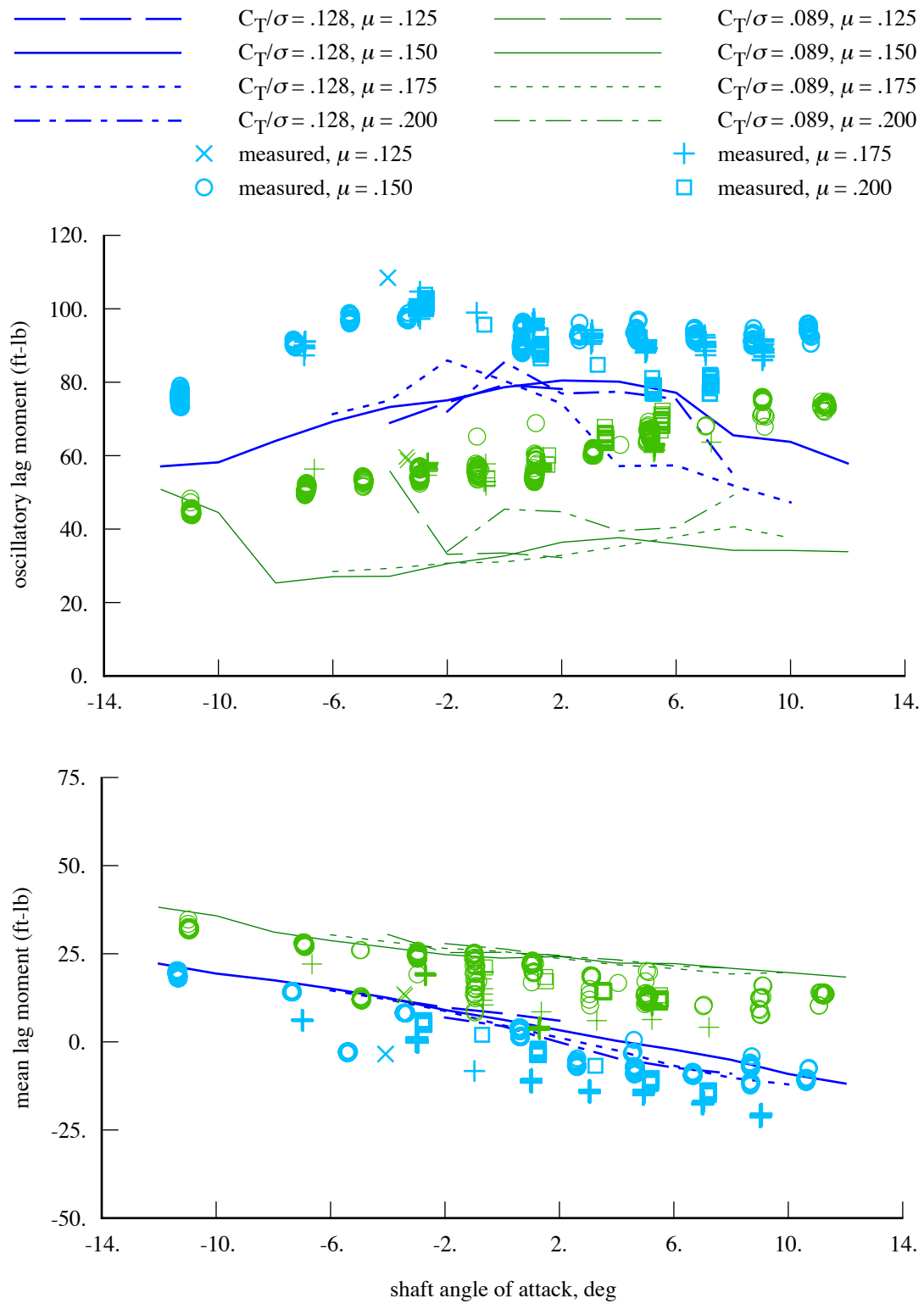


Figure 32. Measured and calculated TRAM helicopter mode blade loads; lag bending moment at $r = 0.23R$.

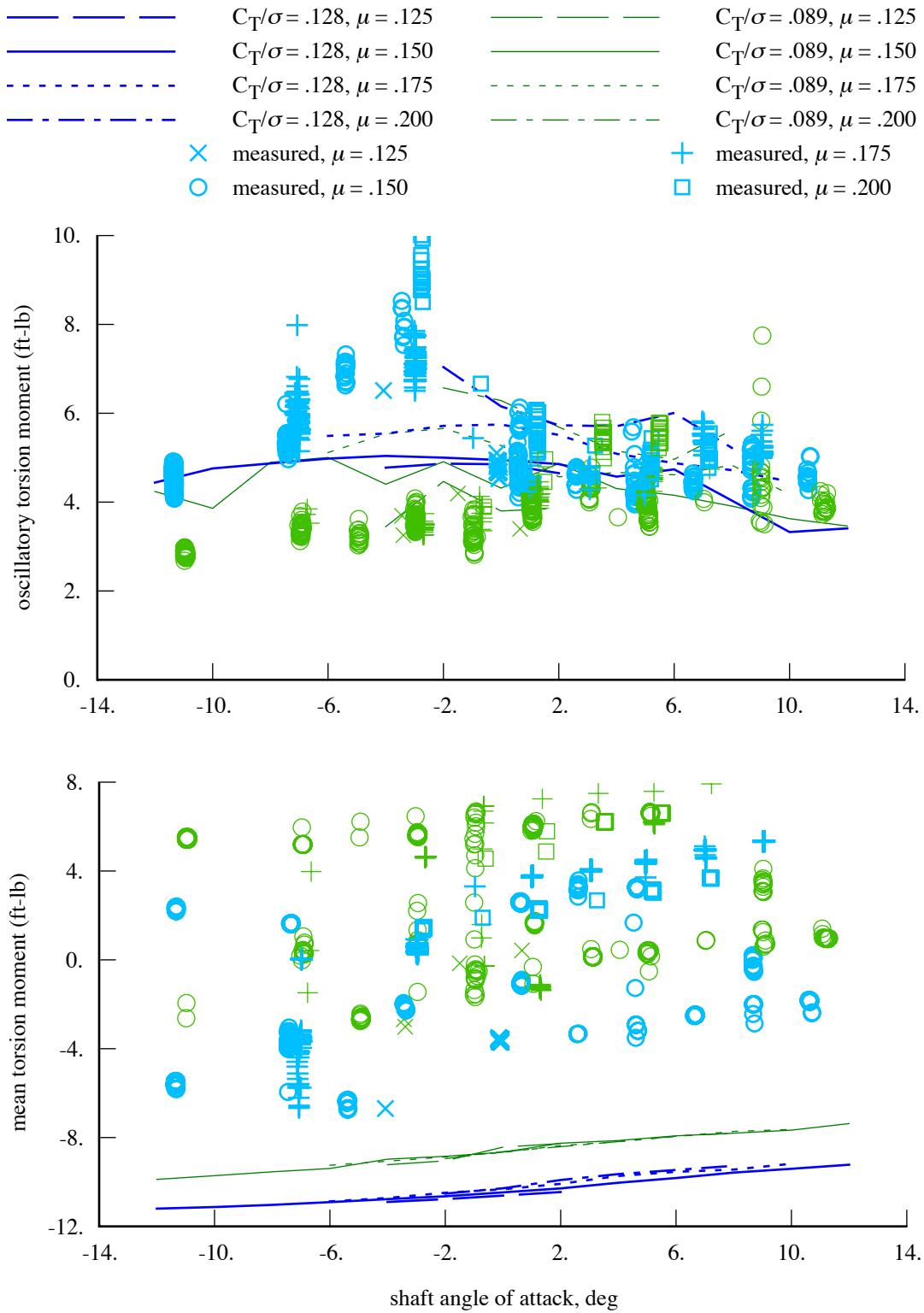


Figure 33. Measured and calculated TRAM helicopter mode blade loads; torsion moment at $r = 0.432R$.

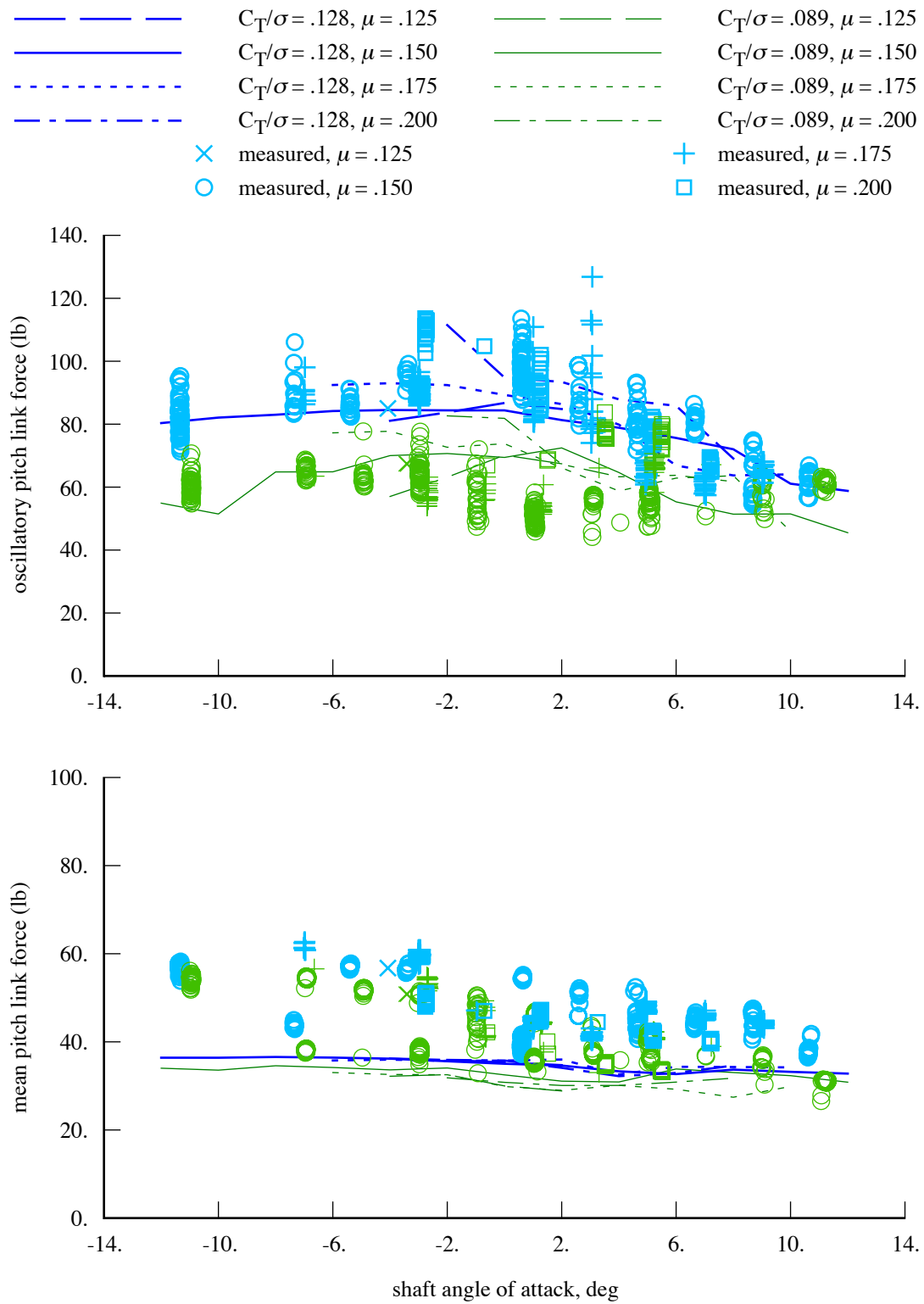


Figure 34. Measured and calculated TRAM helicopter mode blade loads; pitch link A force.

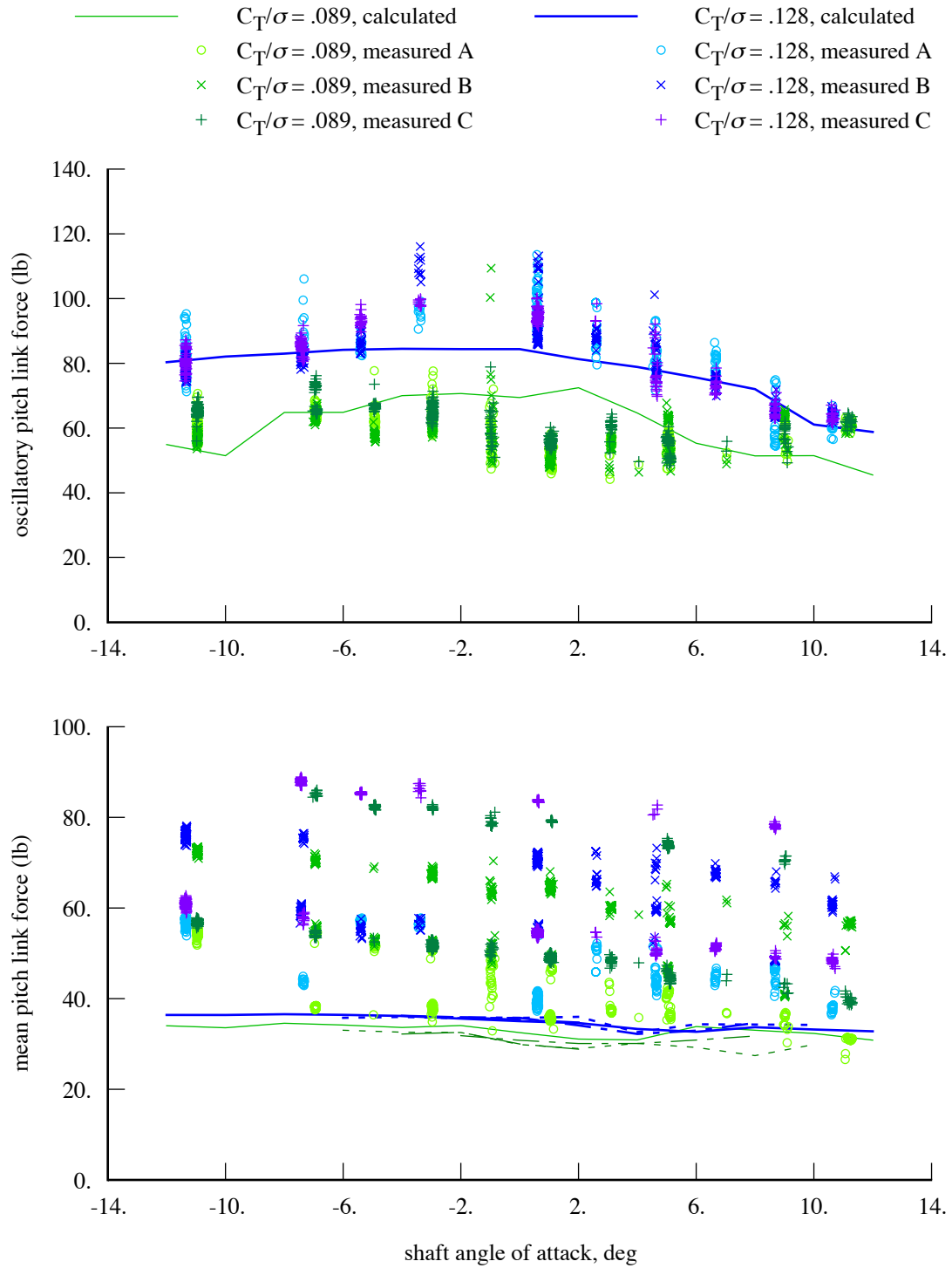


Figure 35. Measured and calculated TRAM helicopter mode blade loads ($\mu = 0.15$); pitch link A, B, C force.

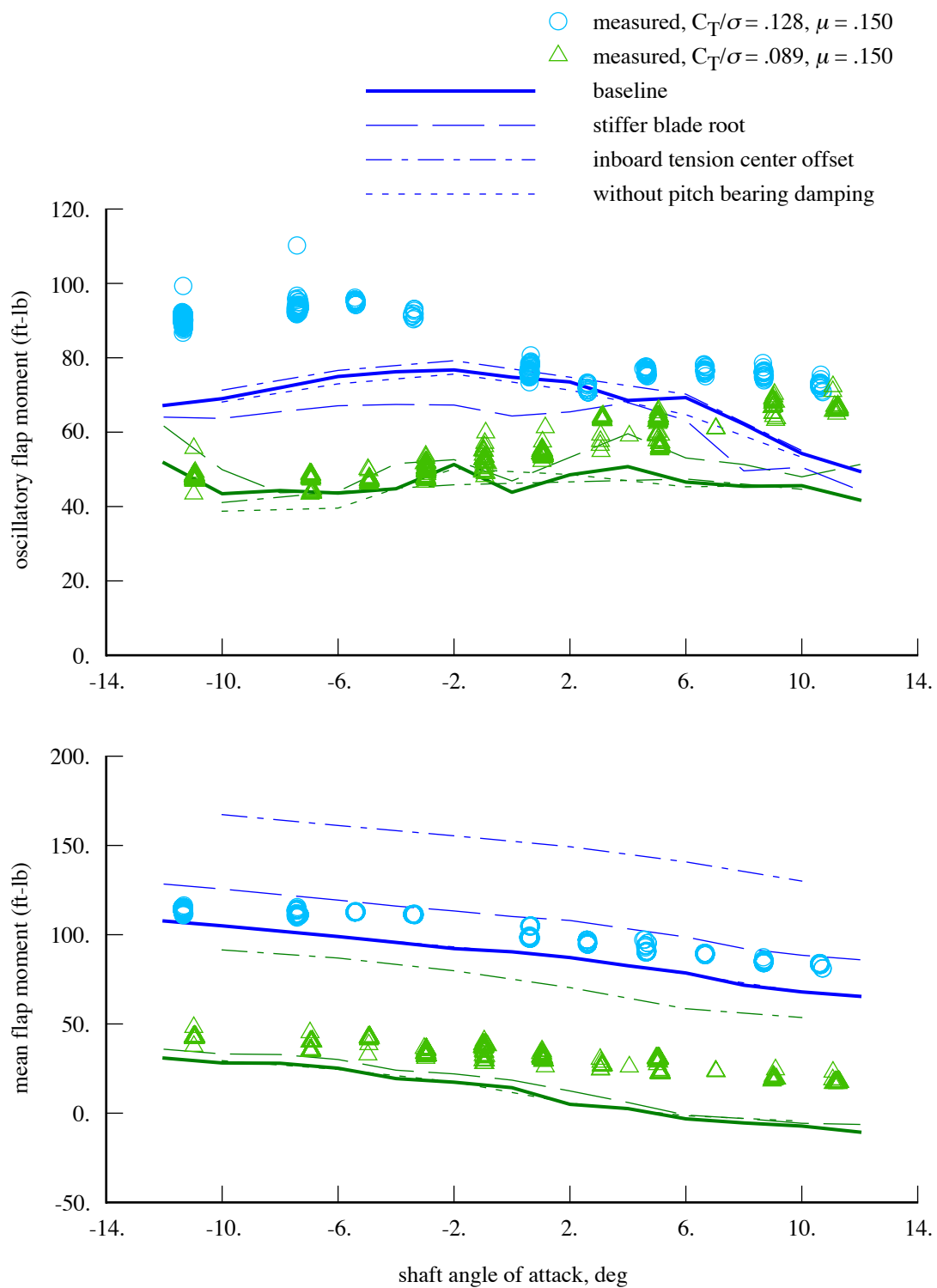


Figure 36. Influence of structural model on calculated TRAM helicopter mode blade loads ($\mu = 0.15$); flap bending moment at $r = 0.23R$.

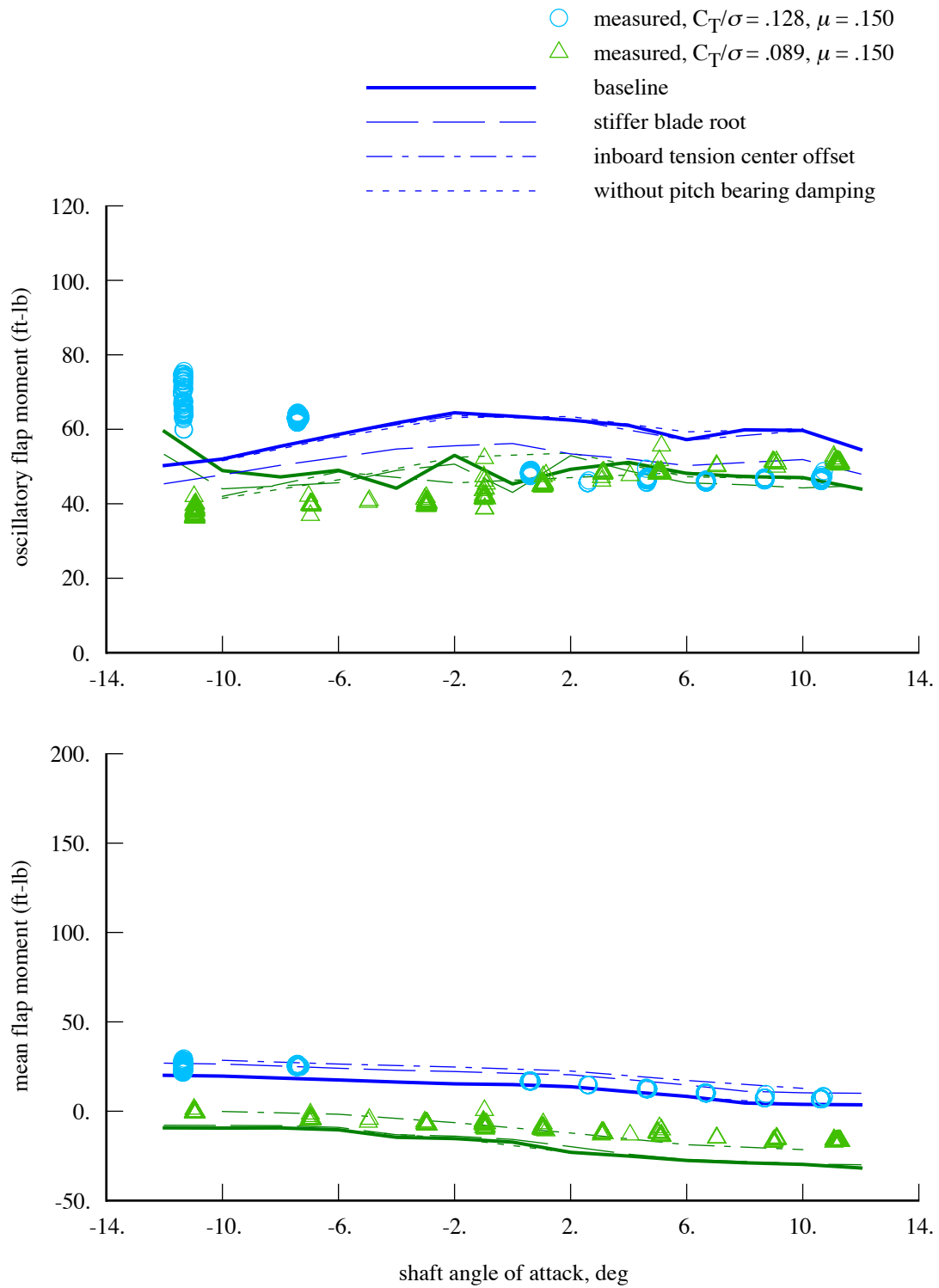


Figure 37. Influence of structural model on calculated TRAM helicopter mode blade loads ($\mu = 0.15$); flap bending moment at $r = 0.50R$.

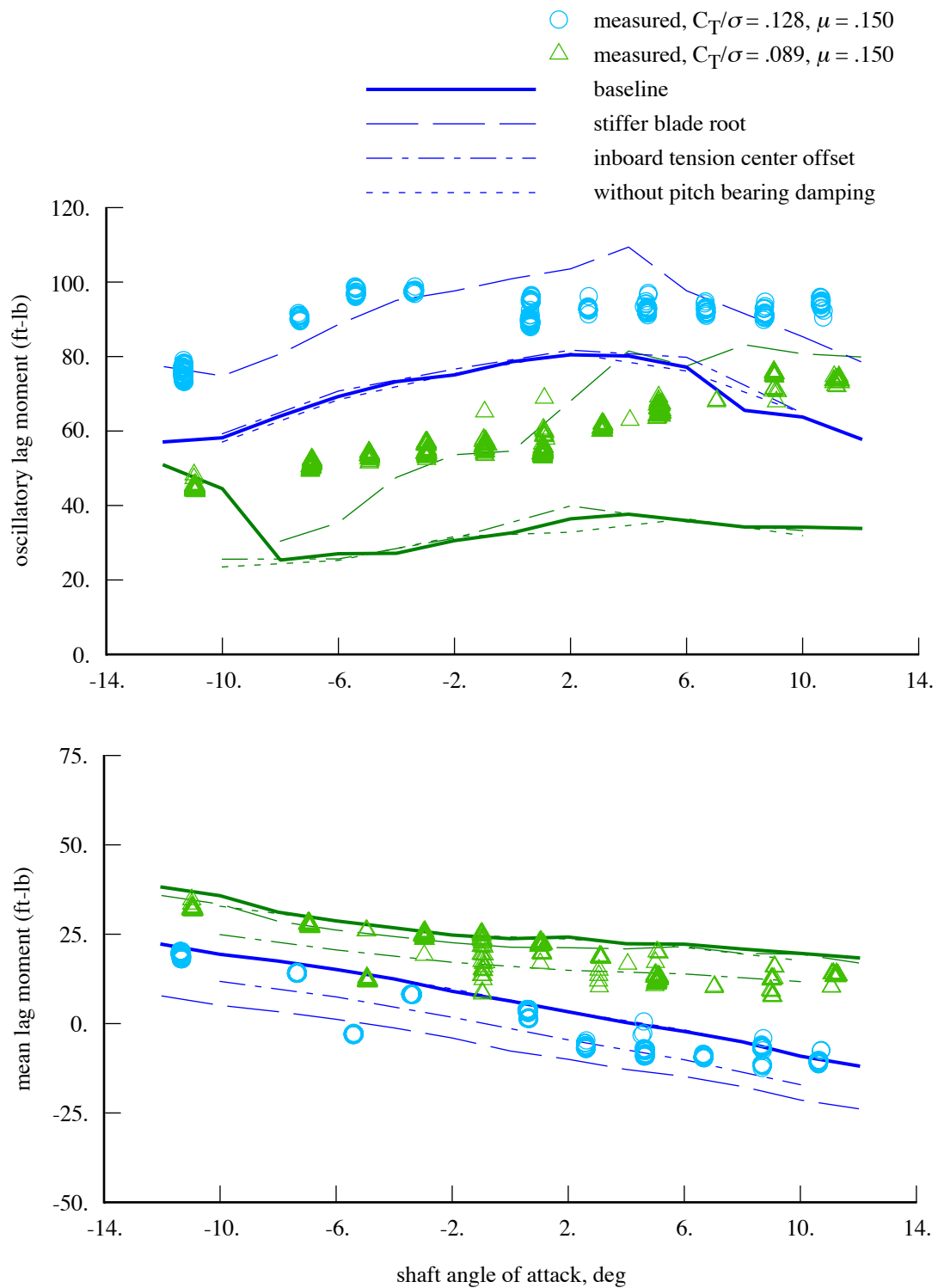


Figure 38. Influence of structural model on calculated TRAM helicopter mode blade loads ($\mu = 0.15$); lag bending moment at $r = 0.23R$.

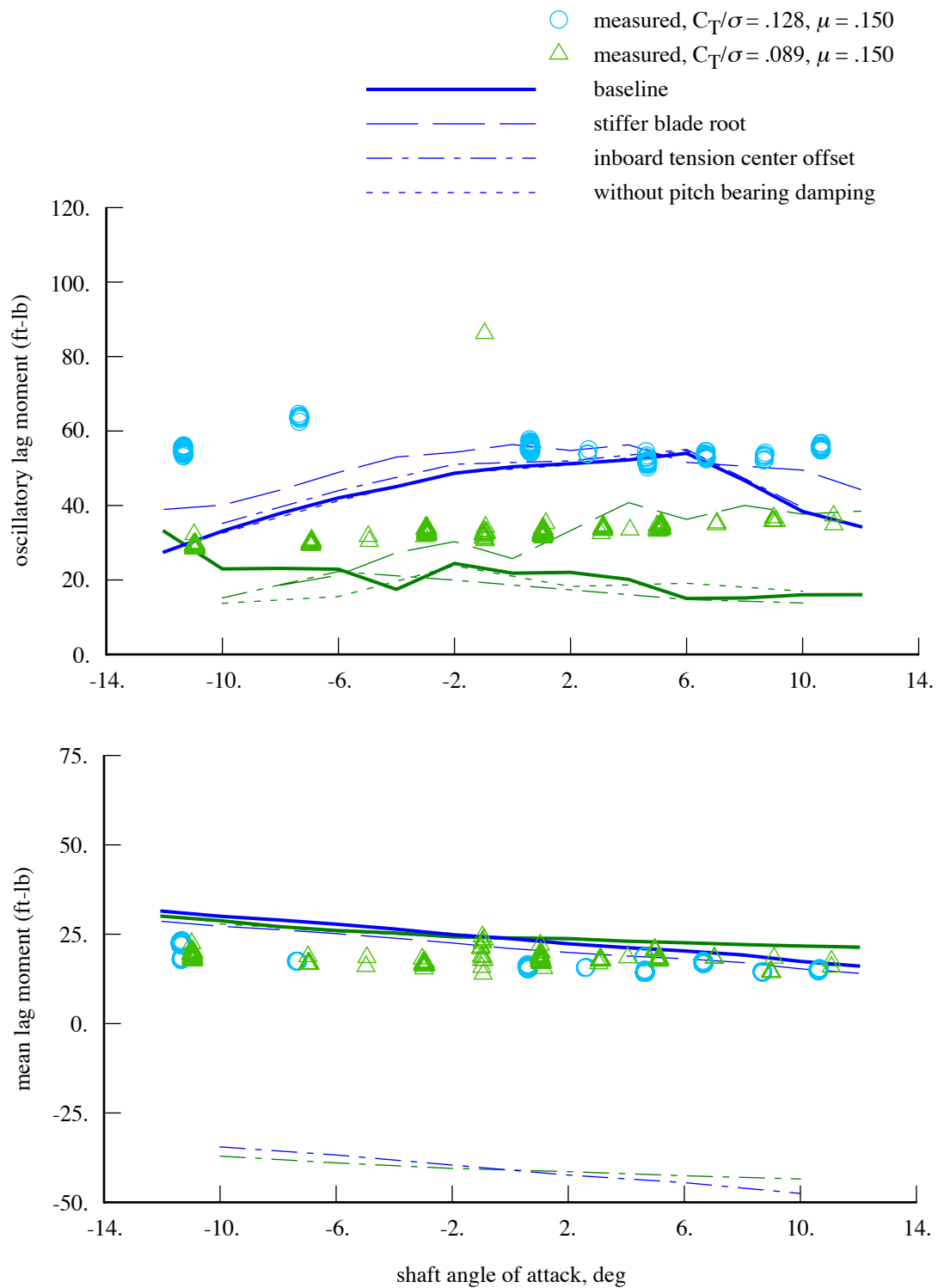


Figure 39. Influence of structural model on calculated TRAM helicopter mode blade loads ($\mu = 0.15$); lag bending moment at $r = 0.50R$.

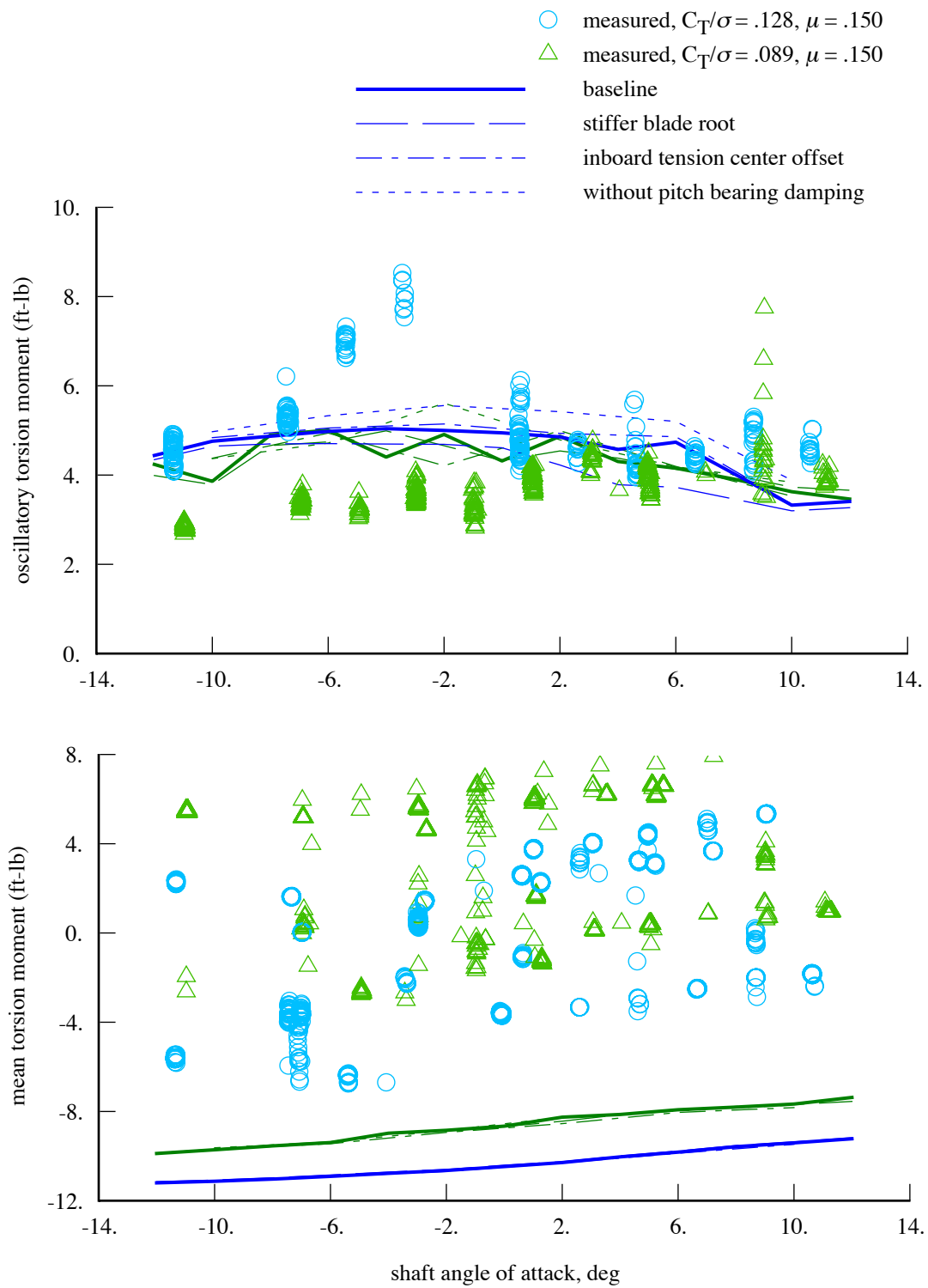


Figure 40. Influence of structural model on calculated TRAM helicopter mode blade loads ($\mu = 0.15$); torsion moment at $r = 0.432R$.

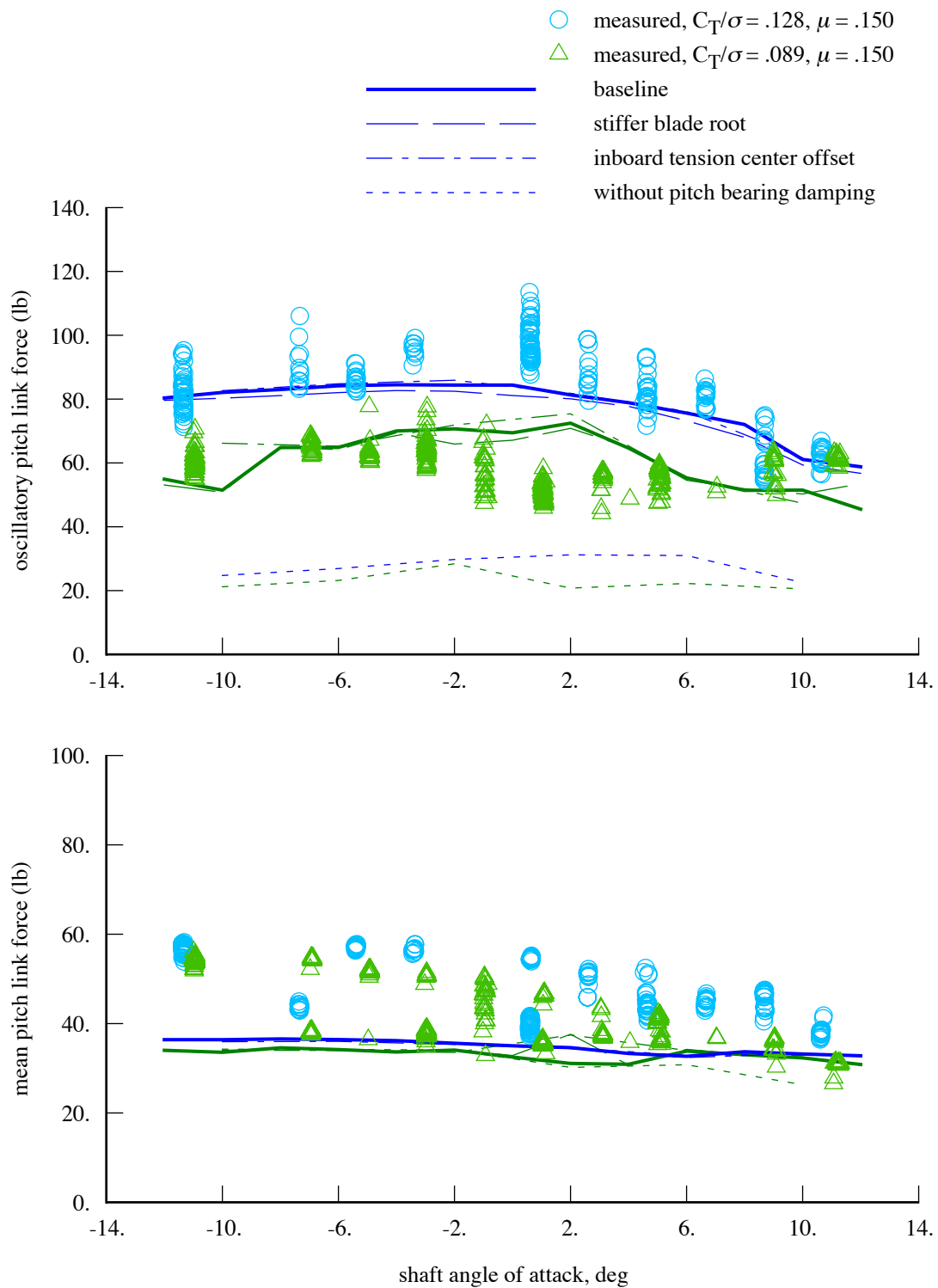


Figure 41. Influence of structural model on calculated TRAM helicopter mode blade loads ($\mu = 0.15$); pitch link A force.

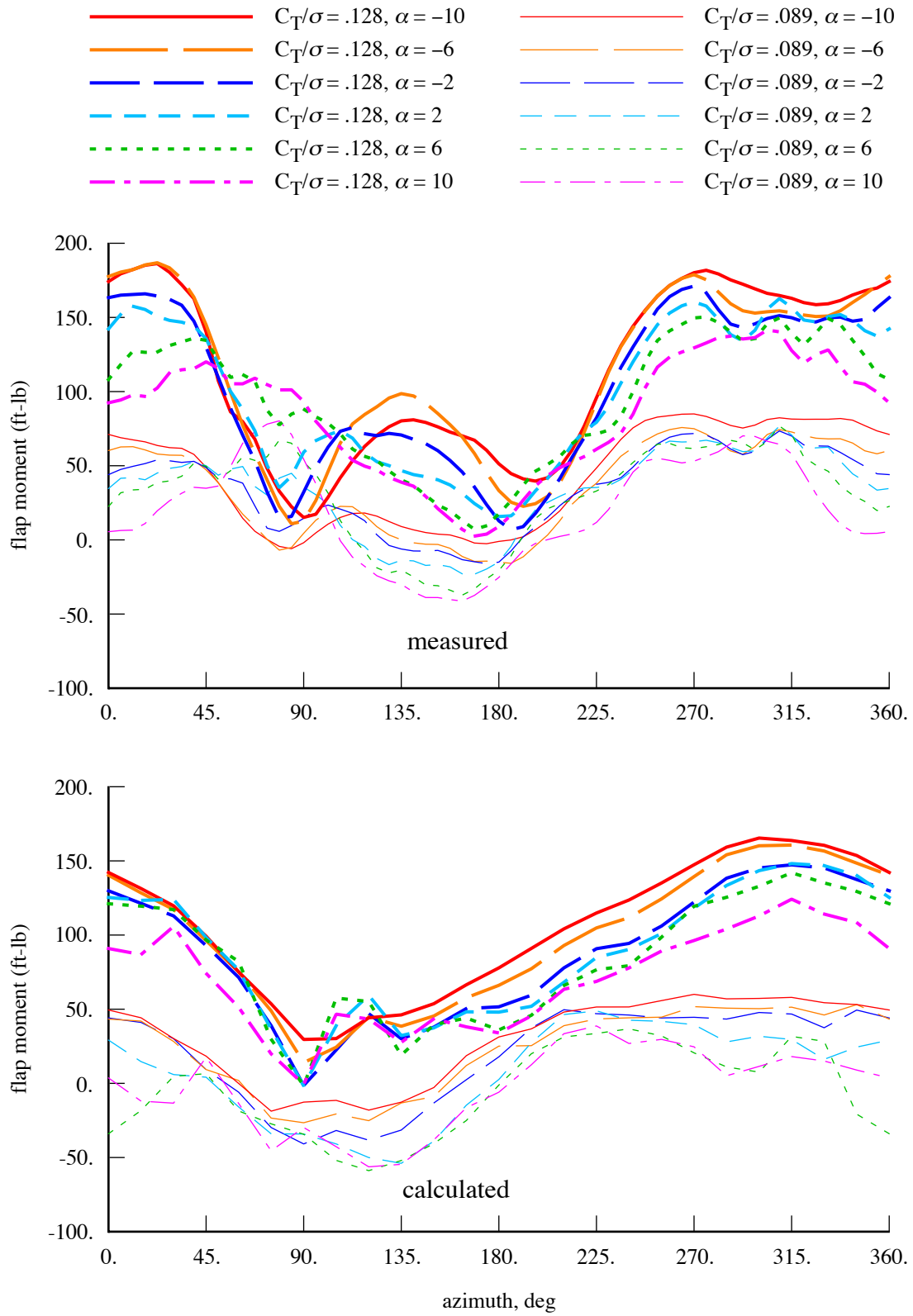


Figure 42. Measured and calculated TRAM helicopter mode blade loads ($\mu = 0.15$).
Flap bending moment at $r = 0.23R$.

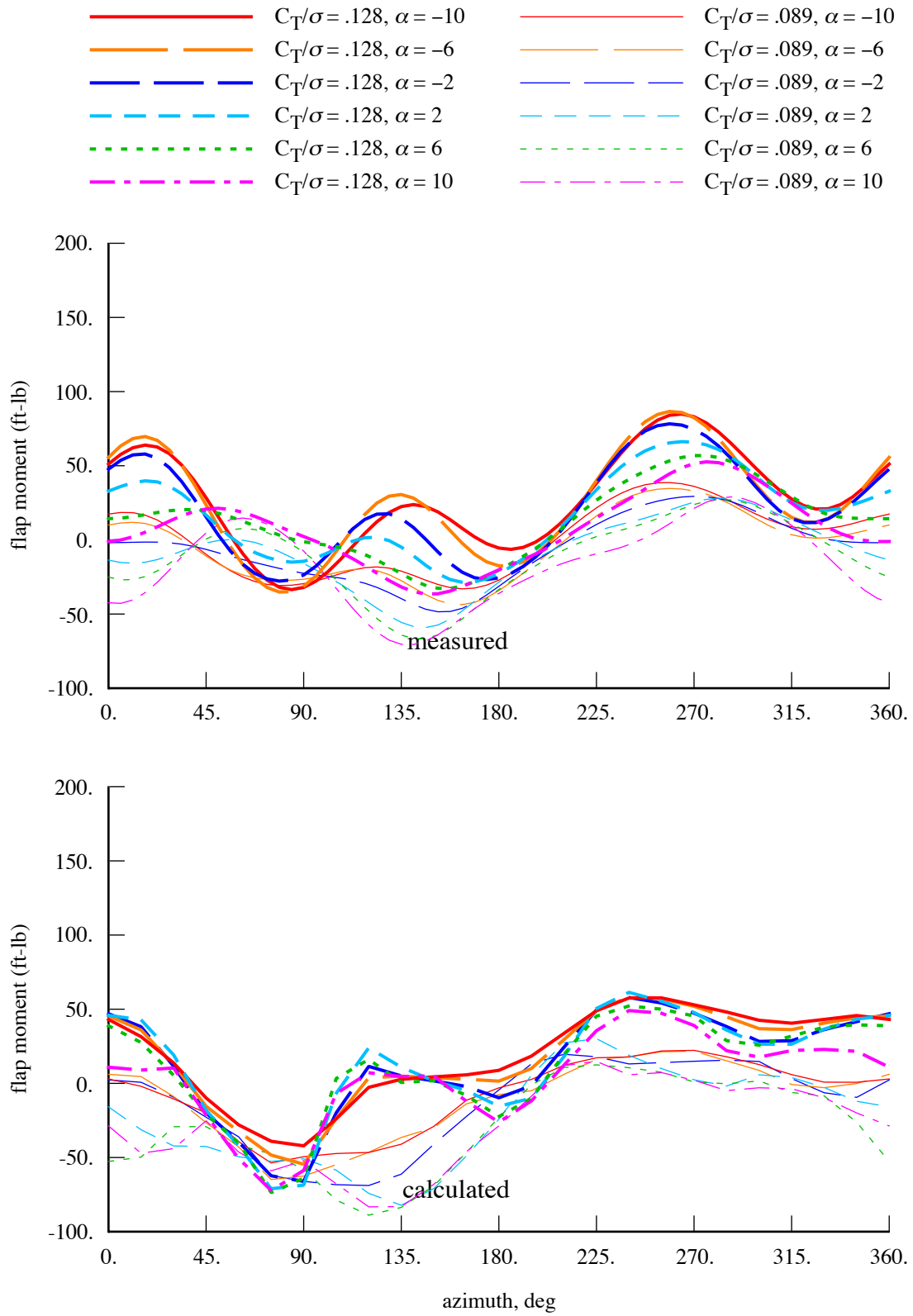


Figure 43. Measured and calculated TRAM helicopter mode blade loads ($\mu = 0.15$).
Flap bending moment at $r = 0.50R$.

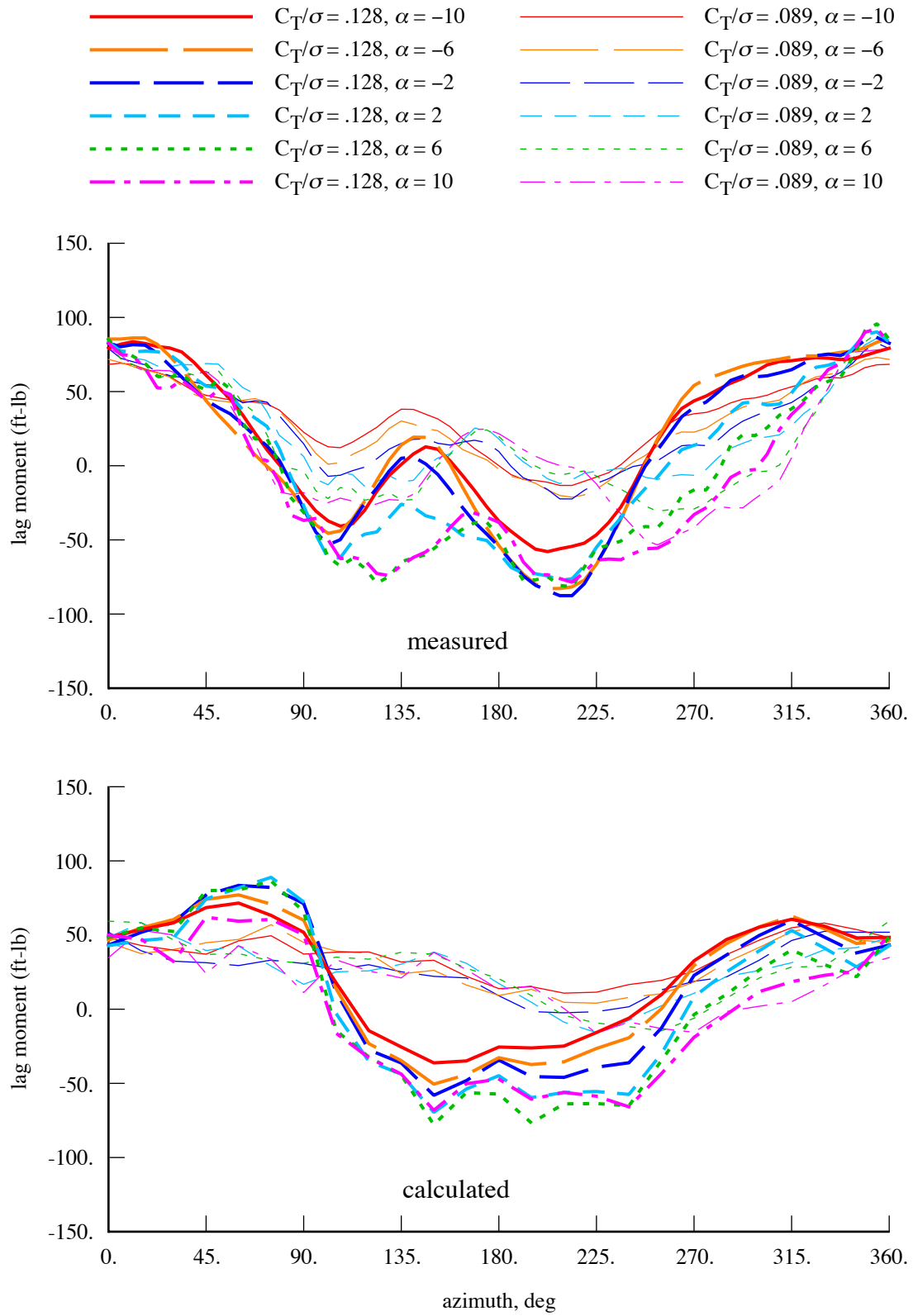


Figure 44. Measured and calculated TRAM helicopter mode blade loads ($\mu = 0.15$).
Lag bending moment at $r = 0.23R$.

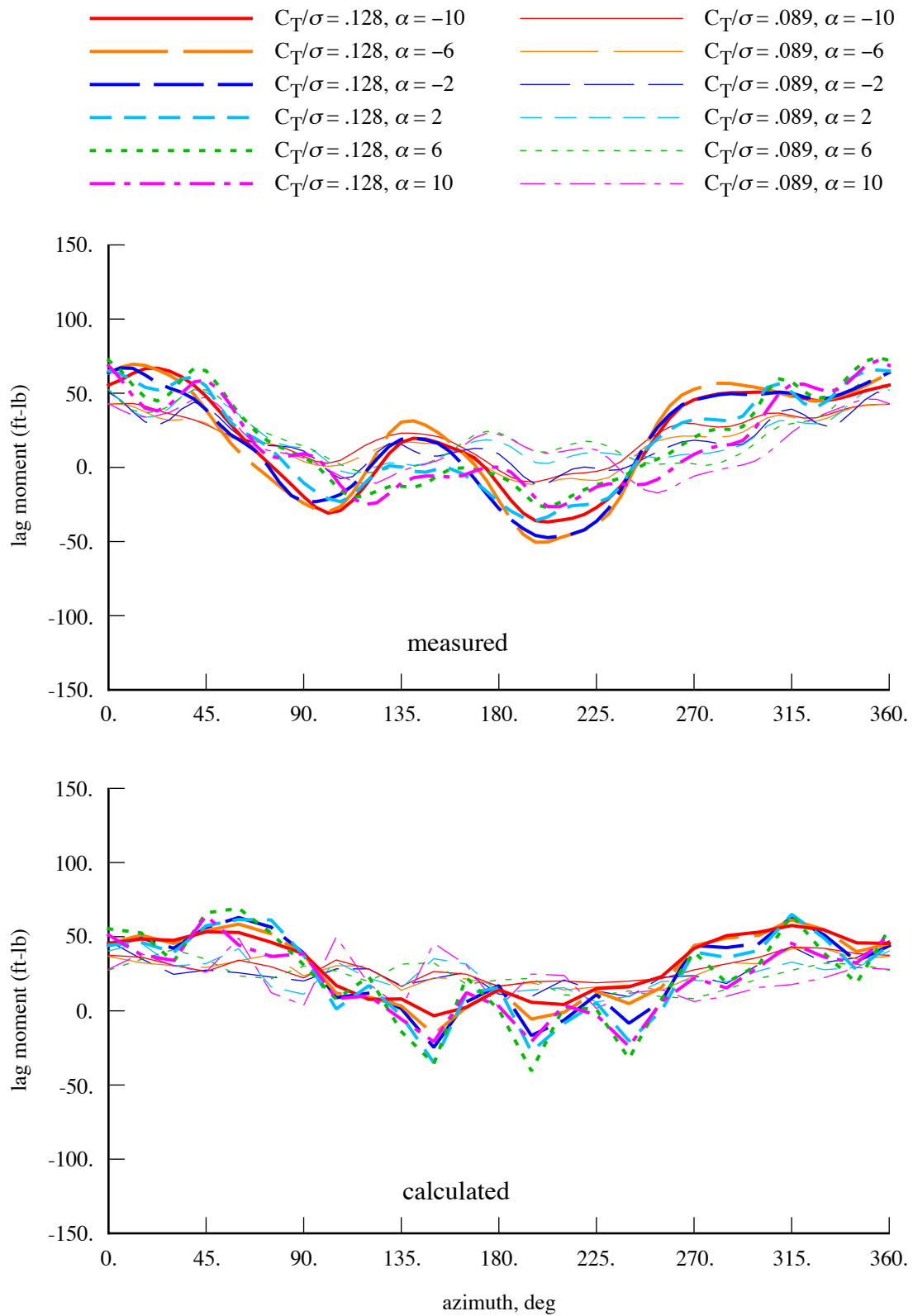


Figure 45. Measured and calculated TRAM helicopter mode blade loads ($\mu = 0.15$).
Lag bending moment at $r = 0.50R$.

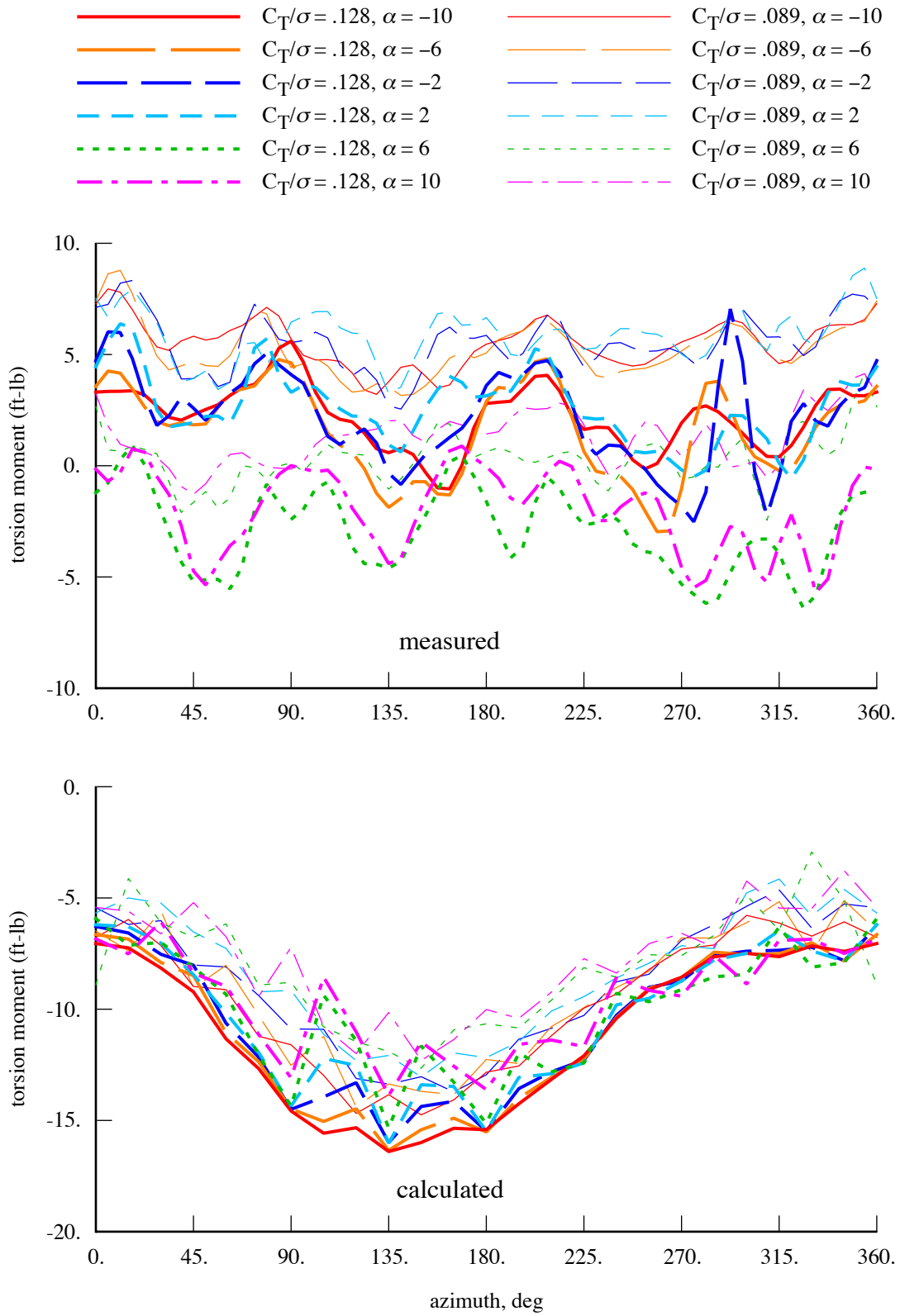


Figure 46. Measured and calculated TRAM helicopter mode blade loads ($\mu = 0.15$).
Torsion moment at $r = 0.432R$.

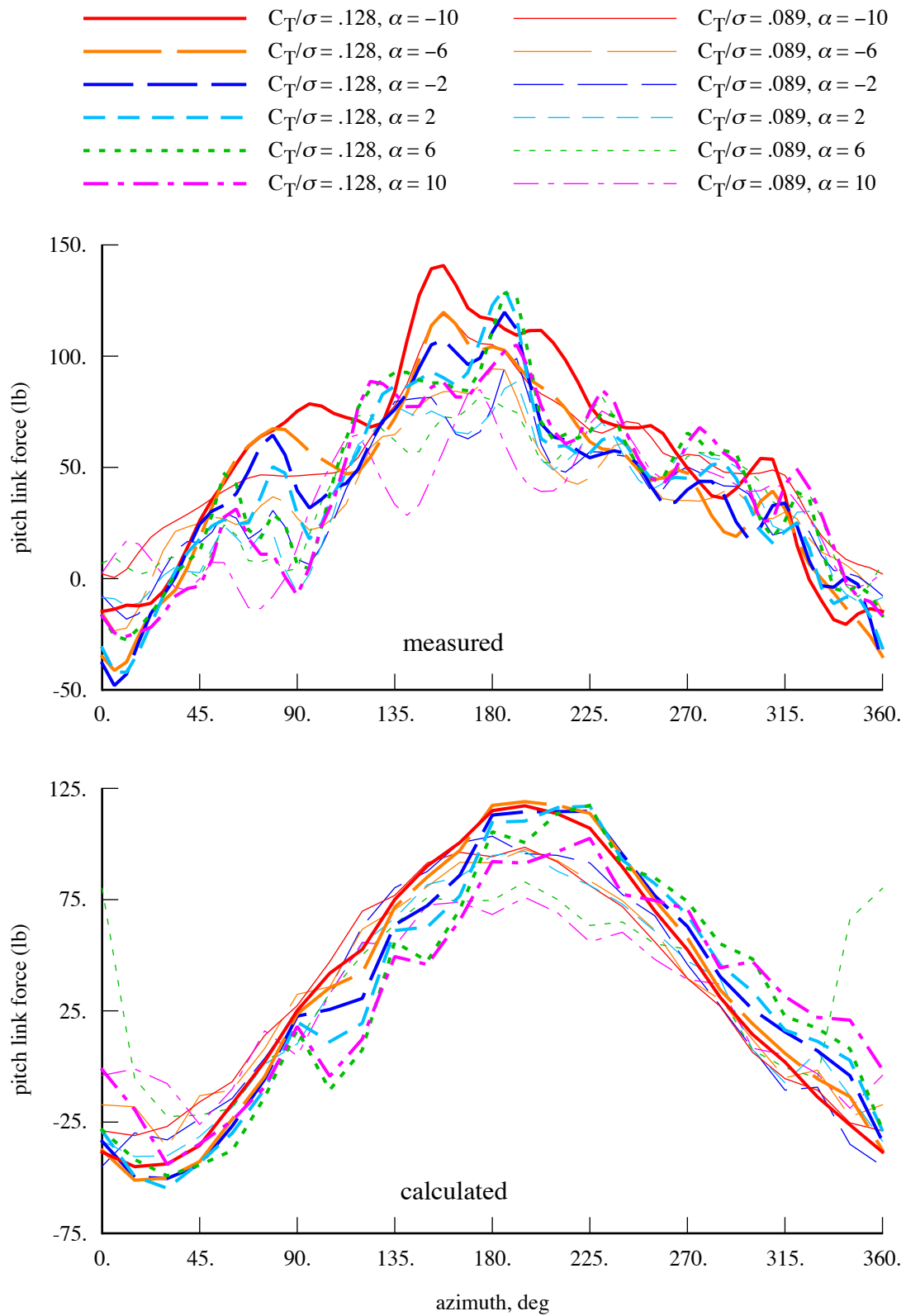


Figure 47. Measured and calculated TRAM helicopter mode blade loads ($\mu = 0.15$).
Pitch link A force.